NOTE TO USERS

Page(s) missing in number only; text follows. Page(s) were scanned as received.

15-16,51,68-69,82,101

This reproduction is the best copy available.

uOttawa

L'Université canadienne
Canada's university

FACULTÉ DES ÉTUDES SUPÉRIEURES ET POSTOCTORALES

uOttawa

L'Université canadienne
Canada's university

FACULTY OF GRADUATE AND POSDOCTORAL STUDIES

Eid Alatawi

AUTEUR DE LA THÈSE / AUTHOR OF THESIS

M.A.Sc. (Mechanical Engineering)

GRADE / DEGREE

Department of Mechanical Engineering

FACULTÉ, ÉCOLE, DÉPARTEMENT / FACULTY, SCHOOL, DEPARTMENT

Simulation of Axisymmetric Round Jet with and without Coflow Using Vortex-In-Cell Method

TITRE DE LA THÈSE / TITLE OF THESIS

Roger Milane

DIRECTEUR (DIRECTRICE) DE LA THÈSE / THESIS SUPERVISOR

CO-DIRECTEUR (CO-DIRECTRICE) DE LA THÈSE / THESIS CO-SUPERVISOR

EXAMINATEURS (EXAMINATRICES) DE LA THÈSE / THESIS EXAMINERS

Edgar Matida

Bertrand Jodoin

Gary W. Slater

Le Doyen de la Faculté des études supérieures et postdoctorales / Dean of the Faculty of Graduate and Postdoctoral Studies

Simulation of Axisymmetric Round Jet with and without Coflow Using Vortex-In-Cell Method

Eid Alatawi

A thesis submitted to the Faculty of Graduate and Postdoctoral Studies
in partial fulfilment of the requirements for the degree of

MASTER OF APPLIED SCIENCE

in Mechanical Engineering

Ottawa-Carleton Institute for Mechanical and Aerospace Engineering
University of Ottawa
Ottawa, Canada

April 2008

Your file Votre référence
ISBN: 978-0-494-48431-9
Our file Notre référence
ISBN: 978-0-494-48431-9

Abstract

The vortex-in-cell is developed to simulate an axisymmetric round jet with and without coflow. For an incompressible and viscous jet, the method consists in three fractional steps. The first fractional step describes the convection of interacting vortex elements. The second and third fractional steps simulate the diffusion of vorticity using the diffusion velocity method and the deterministic diffusion, respectively.

For the jet with no coflow, the methodology is tested by initializing the vorticity field with one vortex sheet, multiple vortex sheets and with the Stokes stream function using one and multiple vortex sheets. Two inflow profiles are tested, the top hat profile and the jet self similar profiles. The sensitivity of the results to the number of vortex elements and grid size are presented and compared. Also, the effect of perturbing the top hat inflow velocity profile is investigated. The jet with coflow is investigated using top hat inflow velocity profile with one and multiple vortex sheets. The mean centerline velocity, streamwise mean velocity profile, vorticity contour, instantaneous distribution of vortex elements, root-mean-square longitudinal and lateral velocity fluctuations, cross-stream correlation are presented. The results are compared with previous experimental measurements and numerical simulation using vortex method.

Acknowledgements

I would like to express my gratitude to my supervisor Dr. Roger Milane for his advice, guidance, constructive criticism and continuous help throughout this work and my study.

Thanks also go to my colleagues for their encouragement and help. Also, I want to thank the academic members of the department of mechanical engineering for their valuable assistance.

My deepest appreciation goes to my parents for their patience and support. Indeed working in this thesis has been very much interesting and much beneficial.

Table of Contents

Abstract i
Acknowledgements ii
Table of Contents iii
List of Figures vi
List of Tables xii
Nomenclature xiii

Chapter 1. Introduction

1.1 Turbulent Flow 1
1.2 Jet Flow 2
1.3 Vortex Methods 4
1.4 Objectives 5

Chapter 2. Literature Survey

2.1 Vortex Methods in Round Jets 8
2.2 Diffusion-Velocity Method and Deterministic Diffusion 11
2.3 Other Methods Applied in Jets 13

Chapter 3. Governing Equations and Numerical Approximation

3.1 Vorticity Equation 15
3.2 Axisymmetric Vorticity Equation without Swirl 17
3.3 Numerical Method and Approximation 19
3.3.1 Numerical Approximation for Poisson's Equation 20
3.3.2 Numerical Approximation of the First Diffusion Fractional Step 22
3.3.3 Numerical Approximation of the Second Diffusion Fractional Step 23

Chapter 4. Vortex-In-Cell

4.1 Vortex Particles 25
4.2 Interpolation Scheme 26
4.3 Convection and Diffusion Velocity 27
4.4 Jet with No Coflow 29
4.4.1 Boundary and Initial Conditions 29
4.4.2 Solution Procedure 33
4.5 Jet with Coflow 35
4.5.1 Boundary and Initial Conditions 35
4.5.2 Solution Procedure 37

Chapter 5. Results for Axisymmetric Jet with No Coflow

5.1 Numerical Parameters 40
5.2 Flow Field Results 41
5.2.1 Streamwise Centerline Velocity Variation 41
5.2.2 Mean flow 42
5.2.3 Velocity Fluctuations and Cross Correlation 43
5.2.4 Vorticity Contour and Vortex Distribution 45
5.2.5 Sensitivity to the Number of Vortex Elements 45
5.2.6 Sensitivity to the Grid Size 47
5.2.7 Effect of the Convective Outflow Velocity 48
5.2.8 Effect of Perturbation 49
5.3 Effect of Inflow Boundary Condition 50
5.4 Initialization of Vorticity Using Stokes Stream Function 51
5.5 Initialization of Vorticity-Multiple Vortex Sheets 53
5.5.1 Top Hat Profile – Several Sheets 53
5.5.1.1 Sensitivity to Number of Vortex Elements 56
5.5.1.2 Sensitivity to Convective Outflow Velocity 56
5.5.2 Stokes Stream Function 57

Chapter 6. Results for Axisymmetric Jet with Coflow

6.1 Numerical Parameters 59
6.2 Flow Field Results 60
6.2.1 Streamwise Centerline Velocity Variation 60
6.2.2 Mean Velocity 62
6.2.3 Velocity Fluctuations and Cross Correlation 62
6.2.4 Vorticity Contour and Vortex Distribution 64
6.3 Initialization of Vorticity– Multiple Vortex Sheets with Top Hat Inflow 65

Chapter 7. Conclusions and Recommendations

7.1 Conclusions 67
7.2 Recommendations for Future Studies 69

References 112
Appendix 117

List of Figures

Figure 1: (a) Two dimensional area-weighting scheme in the VIC method. (b) Two-dimensional area-weighting scheme to transfer the change of vorticity onto the vortex elements.

Figure 2: Computational domain for jet with no coflow, rectangular grid, initial position of the vortices and boundary conditions.

Figure 3: Computational domain for jet with coflow, rectangular grid, initial position of the vortices and boundary conditions.

Figure 4: Streamwise mean centerline decay, (a) comparison with 2D simulation of Sidahmed & Brown (2001), (b) comparison with 3D simulation of Boersma et al. (1998).

Figure 5: (a) Radial profiles of mean axial velocity showing the spreading of the jet flow at two downstream locations, (b) the streamwise mean velocity profiles of the jet at three axial positions.

Figure 6: Normalized streamwise mean velocity: (a) present simulation compared with the experiment of Wygnanski & Fiedler (1969), (b) present simulation compared with the 2D simulation of Chung & Troutt (1988).

Figure 7: Root mean square fluctuations normalized with the streamwise mean centerline velocity at three downstream locations: (a) rms longitudinal velocity fluctuations, (b) rms lateral velocity fluctuations. The mesh lines connecting the open symbols show the predicted profiles; the dark symbols correspond to the data from the experiment of Wygnanski & Fiedler (1969).

Figure 8: Normal Reynolds stresses normalized with the square of streamwise mean centerline velocity at two downstream locations: (a) longitudinal Reynolds stress, (b) lateral Reynolds stress. The mesh lines connecting the open symbols show the predicted profiles; the dark symbols correspond to the data from the experiment of Hussein et al. (1994).

Figure 9: Normalized cross-stream correlation at three downstream locations: (a) comparison with the experiment of W&F, (b) magnification of the simulated cross-stream correlation. The mesh lines connecting the open symbols show the predicted profiles; the dark symbols correspond to the data from the experiment of Wygnanski & Fiedler (1969).

Figure 10: (a) Instantaneous distribution of vortex elements, (b) vorticity contour, contour level increment is 2000.

Figure 11: Effect of the number of vortices on (a) streamwise mean centerline decay, (b) streamwise mean velocity, (c) rms longitudinal fluctuations, (d) rms lateral fluctuations.

Figure 12: Effect of the number of vortices on vortices distribution: (a) 750 vortices, (b) 2560 vortices, (c) 3300 vortices, (d) 19800 vortices.

Figure 13: Effect of grid size on: (a) the decay of the streamwise mean centerline velocity , (b) streamwise mean velocity at two downstream locations, (c) r.m.s. longitudinal velocity fluctuations at two downstream locations, and (d) r.m.s. lateral velocity fluctuations at two downstream locations.

Figure 14: Comparison of one sheet $U_{con}=U_J$ with one sheet $U_{con}=U_{AVG}$ at two downstream locations: (a) streamwise mean velocity, (b) rms longitudinal velocity fluctuations, (c) rms lateral velocity fluctuations, (d) cross-stream correlation.

Figure 15: Streamwise mean centerline decay using perturbation compared with streamwise mean centerline decay without perturbation.

Figure 16: Comparison of case without perturbation with case with perturbation at two downstream locations: (a) streamwise mean velocity, (b) rms longitudinal velocity fluctuations, (c) rms lateral velocity fluctuations, (d) cross-stream correlation.

Figure 17: Streamwise mean centerline velocity using self similar inflow boundary condition.

Figure 18: Effect of inflow boundary conditions on flow field, top hat inflow profile versus self similar profile at two downstream locations: (a) streamwise mean velocity, (b) rms longitudinal velocity fluctuation, (c) rms lateral

velocity fluctuation, (d) cross-stream correlation. Dark symbols, top hat; Open symbols, self similar profile.

Figure 19: Effect of self similar profile inflow boundary condition on : (a) instantaneous distribution of vortex elements, (b) vorticity contour, contour level increment is 2000.

Figure 20: Streamwise mean centerline velocity using Stokes stream function with one vortex sheet.

Figure 21: Comparison one sheet (base run) with one sheet using Stokes stream function at two downstream locations: (a) streamwise mean velocity, (b) rms longitudinal velocity fluctuations, (c) rms lateral velocity fluctuations, (d) cross-stream correlation.

Figure 22: Vorticity field distribution in the radial direction for cases: (a) one vortex sheet without Stokes, (b) one vortex sheet with Stokes.

Figure 23: Comparison of vorticity contours for one sheet: (a) base run, (b) using Stokes stream function, contour level increment is 2000.

Figure 24: Comparison one sheet and two sheets with Exp. of W & F at two downstream locations: (a) streamwise mean velocity, (b) rms longitudinal velocity fluctuations, (c) rms lateral velocity fluctuations, (d) cross-stream correlation. Dark diamond and circle symbols, Exp. of Wygnanski & Fiedler (1969); mesh lines connecting dark symbols, one sheet; mesh lines connecting open symbols, two sheets.

Figure 25: Comparison one sheet and five sheets with Exp. of W & F at two downstream locations: (a) streamwise mean velocity, (b) rms longitudinal velocity fluctuations, (c) rms lateral velocity fluctuations, (d) cross-stream correlation. Dark diamond and circle symbols, Exp. of Wygnanski & Fiedler (1969); mesh lines connecting dark symbols, one sheet; mesh lines connecting open symbols, five sheets.

Figure 26: Comparison one sheet and ten sheets with Exp. of W & F at two downstream locations: (a) streamwise mean velocity, (b) rms longitudinal velocity fluctuations, (c) rms lateral velocity fluctuations, (d) cross-stream correlation. Dark diamond and circle symbols, Exp. of Wygnanski &

Fiedler (1969); mesh lines connecting dark symbols, one sheet; mesh lines connecting open symbols, ten sheets.

Figure 27: Effect of initializing on the streamwise mean centerline decay using: (a) one sheet, (b) two sheets, (c) five sheets, and (d) ten sheets. Dark square symbols, present simulation; open square symbols, 2D simulation of Sidahmed & Brown (2001).

Figure 28: Comparison of vorticity contours for cases: (a) one sheet, (b) two sheets, (c) five sheets, (d) ten sheets, contour level increment is 2000.

Figure 29: Sensitivity of number of vortex elements N_v=9900 and 6400 vortices using five sheets to: (a) the streamwise mean centerline velocity, (b) the streamwise mean velocity at two downstream locations, (c) rms longitudinal fluctuations at two downstream locations, and (d) rms lateral fluctuations at two downstream locations.

Figure 30: Comparison of $U_{con}=U_J$ with $U_{con}=U_{AVG}$ using five sheets at two downstream locations: (a) streamwise mean velocity, (b) rms longitudinal velocity fluctuations, (c) rms lateral velocity fluctuations, (d) cross-stream correlation.

Figure 31: Comparison one sheet and five sheets using Stokes with Exp. of W&F at two downstream locations: (a) streamwise mean velocity, (b) rms longitudinal velocity fluctuations, (c) rms lateral velocity fluctuations, (d) cross-stream correlation. Dark diamond and circle symbols, Exp. of Wygnanski & Fiedler (1969); mesh lines connecting dark symbols, one sheet; mesh lines connecting open symbols, five sheets.

Figure 32: Comparison one sheet and ten sheets using Stokes with Exp. of W&F at two downstream locations: (a) streamwise mean velocity, (b) rms longitudinal velocity fluctuations,(c) rms lateral velocity fluctuations, (d) cross-stream correlation. Dark diamond and circle symbols, Exp. Of Wygnanski & Fiedler (1969); mesh lines connecting dark symbols, one sheet; mesh lines connecting open symbols, ten sheets.

Figure 33: Effect of initializing using Stokes on the streamwise mean centerline decay using: (a) five sheets, (b) ten sheets. Dark square symbols, present simulation; open square symbols, 2D simulation of Sidahmed & Brown (2001).

Figure 34: Streamwise mean centerline velocity: (a) comparison with experiment of Forstall & Shapiro (1950), (b) comparison with 3D simulation of Uchiyama (2003).

Figure 35: Radial profiles of the streamwise mean velocity at two downstream locations showing the spreading of, (a) coflow jet, and (b) no coflow jet.

Figure 36: Streamwise mean velocity normalized with the difference of streamwise mean centerline velocity and the coflowing velocity at three downstream locations: (a) present simulation compared with the experiment of Antonia & Bilger (1973), (b) present simulation compared with the 3D simulation of Uchiyama (2003).

Figure 37: Longitudinal root mean square fluctuations normalized with the difference of streamwise mean centerline velocity and the coflowing velocity at three downstream locations: (a) present simulation compared with the experiment of Antonia & Bilger (1973), (b) present simulation compared with the 3D simulation of Uchiyama (2003).

Figure 38: Lateral root mean square fluctuations normalized with the difference of streamwise mean centerline velocity and the coflowing velocity at three downstream locations.

Figure 39: Cross-stream correlation normalized with the square of the difference of streamwise mean centerline velocity and the coflowing velocity at three downstream locations: (a) comparison with the experiment of Antonia & Bilger (1973), (b) magnification of the simulated cross-stream correlation. The mesh lines connecting the open symbols show the present predicted profiles; the dark symbols correspond to the data from the experiment of Antonia & Bilger (1973).

Figure 40: (a) Instantaneous distribution of vortex elements, (b) Vorticity contour for coflow jet, contour level increment is 2000.

Figure 41: Streamwise mean centerline velocity decay using ten sheets of vortex elements compared with 3D simulation of Uchiyama (2003).

Figure 42: Comparison one sheet with ten sheets at two downstream locations: (a) streamwise mean velocity, (b) rms longitudinal velocity fluctuations, (c) rms lateral velocity fluctuations, (d) cross-stream correlation. Open symbols, ten sheets; dark symbols, one sheet.

List of Tables

Table I Sensitivity of root mean square velocity fluctuations to number of vortices.

Table II Figures for statistic results.

Nomenclature

A_{t_z}	Total area contributed by all particles
A_z	Area contribution of each particle
d	Distance between vortices
D	Nozzle diameter
h	Grid size in area weighting scheme
H	Length of the computational domain
N_v	Number of vortices
Re_D	Reynolds number based on the diameter of the nozzle
R	Nozzle radius
t	Time
u	Velocity vector
v, w, u	Velocity components
u_{diff}, v_{diff}	Diffusion velocities
U_i, V_i	Velocity components of the vortices
U_n, V_n	Components of velocity at nodes
U	Streamwise mean velocity
V	Lateral mean velocity
U_J	Jet exit velocity
U_a	Coflowing velocity
U_C	Streamwise mean centerline velocity

U_c	Arithmetic average of the jet exit and coflowing velocities
U_{con}	Convective outflow velocity
U_{AVG}	Average velocity at outflow
ΔU	Difference between jet exit and coflowing velocities
x_0	Virtual origin
r, x	Cylindrical coordinates along radial and axial directions
x_i, r_i	Coordinates of the vortices
Δt	Time step
$\Delta x, \Delta r$	Grid sizes in x- and r-direction

Greek Symbols

α	Azimuthal direction in cylindrical coordinates
Γ	Circulation
Γ_i	Circulation of a vortex
ξ	Similarity variable for velocity
ν	Kinematic viscosity
σ	Core radius
ψ	Stream function
ω	Vorticity vector
$\omega_r, \omega_\alpha, \omega_x$	Components of vorticity vector
χ	Trajectories of vortices

$\Delta\omega_\alpha$	Change in azimuthal vorticity
η_1, η_2	Functions in Stokes stream function
λ	Ratio of the difference to the sum of η_1 and η_2
ε	Vortex blob smoothing parameter
γ	Ratio of jet exit velocity to the coflowing velocity

Chapter 1

Introduction

1.1 Turbulent Flow

Turbulent flows have highly irregular motion in which the various quantities such as velocity, pressure and temperature demonstrate a random variation with time and space coordinates. Actually, the turbulence is a superposition of an irregular eddying motion on a mean stream, whose detailed configuration is neither reproducible from one experiment to the next nor predictable theoretically, but whose statistical properties are significant (Philips, 1969). The turbulence can be produced by friction forces at fixed walls such as flow through conduits and flow past bodies. Also, it might be generated by the flow of layers of fluids with different velocities over one another. Turbulence can be defined by common characteristics. The turbulent flow can be three dimensional and two dimensional as in the turbulent motion. The main feature of turbulence is the ability to transport and mix more efficiently than the laminar flow (Pope, 2000). Another essential feature of the turbulent flow is the presence of vortices, which result from the eddies in

turbulent flow. These eddies are of different sizes. The largest eddies, which are produced by the forces driving the flow, are unstable. The instability of these eddies leads to the brake up of these eddies into smaller eddy size. In turn, the small eddies become unstable and produce eddies of even smaller size. This mechanism continues until the eddies are suppressed by viscosity.

The viscosity has significant effect in real viscous fluids. The viscosity transforms the kinetic energy of the flow into heat and this will lead to the dissipation of the kinetic energy. Therefore, the motion of the turbulent flow will decay if there is no external source. Another effect of viscosity is to render the turbulence homogeneous and to become less dependant on direction. Flows that are not in contact with a solid boundary can be categorized into three basic flows: jets, plane wakes and mixing layers. In this study jet flow is simulated. More information about the jet flow mechanism is provided in the next section.

1.2 Jet Flow

Although the mechanics of jet flows have been studied for more than fifty years, they have recently received more attention. Turbulent jets are fluid flows generated due to a pressure drop through a nozzle or an orifice. The dynamics of the jet flow is completely controlled by the vorticity, which determines a local measure of fluid rotation (Grinstein et al, 1995). The generation of vorticity near the jet exit and its convection and diffusion into a portion of space defines the jet's appearance. The initial flow instability and the resulting fluctuating vorticity cause further generation of vorticity. For high

Reynolds numbers, the jet starts with unstable laminar shear layer and then rapidly develops into fully turbulent flow (Tennekes and Lumley, 1972). The process of mixing between a turbulent jet and its surroundings can be divided into two steps. The first step is the entrainment process. The second step is accomplished by the small scale velocity fluctuations which accelerate mixing at the molecular level. One important factor for the propagation of the interface between rotational and irrotational fluid is the entrainment rate. The entrainment rate of the jet is the rate at which fluid from the jet and from its surroundings become mixed as they join at the mixing layers. This rate is controlled by the speed of large scale vortices that move into the surrounding fluid (Tennekes and Lumley, 1972). Therefore, the control of the jet development is dependent on how the jet properties can be affected by the dynamics of large scale vortices i.e., the formation, interaction, merging and breakdown of vortices.

In combustion applications, the jet flow consists of fuel flows into an infinite reservoir of a quiescent fluid (oxidizer). The turbulence mixing, as described above, plays an important role in the initial flow pattern of jets in combustion devices, because the efficiency of these devices depends on the rate of mixing. It is known that most of the noise associated with jet propulsion originates in the turbulent mixing.

The governing equations of turbulent flows are those of conservation of mass, momentum and energy. Because of complexity of turbulent flows including jets, many experiments are carried out to investigate the jet flow behaviour. Recently, it has become possible to study turbulent jet flow by means of numerical simulation. Round jets have been studied using different methods such as direct numerical simulation (DNS) and Large Eddy Simulation (LES). One of the methods that have been used in the numerical

simulation of round jet is the vortex method. This method is described briefly in the following section.

1.3 Vortex Methods

Vortex methods are based on the discretization of the vorticity field into a finite number of vortex points or blobs which are traced at each time using a Lagrangian approach. The point vortex method was used by Rosenhead (1931) to trace the path line of fluid particles with concentrated vorticity (vortex points or blobs) and at each time-step the vorticity transport equation controls the change of vorticity distribution within a blob. Abernathy and Kronauer (1962) applied the point vortex method to simulate vortex streets. Chorin (1973) used vortex blobs method in order to solve the two-dimensional problem. Ashurst (1979) applied Chorin's method in a two-dimensional mixing layer and there was good agreement between simulation results of the downstream evolution of the large scale structures and experiment of Brown and Roshko (1974).

In order to reduce the computational time of the full Lagrangian method, Vortex-in-cell (VIC) method has been developed to solve the vorticity equation. In this method, Eulerian Scheme is used to calculate the velocity field by solving Poisson's equation and the Lagrangian scheme is used to track the vortices obtained from the Laplacian of the stream function. Baker (1979) and Aref and Siggia (1980) applied the VIC method for their research.

Leonard (1980) used three dimensional vortex methods to simulate the interaction of aircraft-trailing vortices and also applied the vortex method to simulate two

dimensional mixing layer. Inoue and Leonard (1987) used two dimensional vortex methods in their research to simulate a spatially growing turbulent mixing layer. Baig and Milane (2004) applied the Reynolds Averaged Navier-Stokes (RANS) with vortex methods. Lin and Pratt (1987), Milane and Nourazar (1995, 1997) and Mansfield et al. (1998) applied large eddy simulation (LES) using vortex methods for their research.

1.4 Objectives

The objectives of this thesis is concerned with the application of the vortex-in-cell method (VIC) for simulating the upper half of axisymmetric round jet using diffusion velocity method and deterministic diffusion to simulate diffusion. In this study, the relevant literature of jet flow using vortex method is reviewed. In addition, a new code for jet flow using VIC, diffusion velocity method and deterministic diffusion is developed.

In the first part of this study, a jet flow issuing into still environment is investigated. Two inflow velocity profiles are tested and compared. One of them is the top hat velocity profile and the other is self similar velocity profile. Several initializations are conducted in this study including one sheet of vortex elements for the top hat and self similar inflow velocity profiles, several sheets of vortex elements for the top hat profile and initializing using the analytical Stokes stream function expression. Flow field results including the centerline decay, the mean streamwise velocity, longitudinal and lateral root mean square fluctuations, cross-stream correlation and vortices distribution are

predicted. The results of the simulation are validated by comparing with the results of two and three dimensional simulation and with experimental measurements.

In the second part of this study, the jet flow issuing into the same fluid with coflowing velocity is considered. The diffusion part in the vorticity equation is modelled as in the first part, i.e., using diffusion velocity method and deterministic diffusion. The center line decay, mean velocity, longitudinal and lateral root mean square fluctuations are reported. The results of the simulation are validated by comparing with the results of 3D simulations and with experimental measurements.

Chapter 2

Literature Survey

In this chapter, the literature related to the topics that handled numerical simulation of jet flow will be reviewed. The studies that apply vortex methods to simulate the round jet flow are introduced in section (2.1). Also, the relevant literature of the techniques used for simulating the diffusion of vorticity is reviewed in section (2.2). Because the vorticity equation for axisymmetric flow in the present study includes two types of diffusion; the first one will be simulated using diffusion velocity method and the second one will be simulated using the deterministic diffusion. In addition, other studies that implement other methods such as Reynolds Averaged Navier Stokes (RANS), Direct Numerical Simulation (DNS) and Large Eddy Simulation (LES) are introduced in section (2.3) because they have some interesting results such as turbulent characteristics and vorticity contour.

2.1 Vortex Methods in Round Jets

Recently, vortex method has been usefully applied to a wide variety of flow field. Vortex method has been developed in context of discrete vortex numerical methods. Discrete vortex methods provide a numerical computation approach for solutions to general incompressible flows. The main purpose of these methods is to have vorticity on a set of Lagrangian computational points by solving the vorticity equation and to get the velocity field by solving the Biot-Savart law. The vorticity field based on the vorticity value should be represented by either singular or continuous representation in order to apply Biot-Savart law. Singular vortex method has concentrated vorticity representation of singular points as the point vortices. The continuous vortex methods have continuous vorticity represented by overlapping elements. Every element can have Gaussian or smooth variation of vorticity in its core. The vortex methods have been used for solution of two and three dimensional problems of both inviscid and viscous flows (Leonard, 1985; Cottet and Koumoutsakos, 2000).

Discrete vortex method was implemented early by Davies and Hardin (1973) in modeling the jet flow. Their results for the starting vortex, i.e., the position of the vortex elements, are qualitatively in agreement with the experiments. Acton (1976) and Acton (1980) modelled the 2D jet flow by vortex ring elements using a fully Lagrangian simulation. The vortex ring element is one form of the vortex elements which is characterized by a circulation Γ, a ring radius and a circular core that has finite radius (Marshall, 2001). The author simulated the jet shear layer and the nozzle surface using a sheet of vortex rings. He used an analytical expression called Stokes Stream Function obtained by Lamb (1932) in order to compute the velocities induced by vortex ring

elements. This expression involves complete elliptic integral of first and second kind, respectively, defined by Abramowitz and Stegun (1972). In his approach, the author accounted for the self induced velocity (Saffman, 1970) in addition to the induced one obtained from the analytical expression. The Stokes stream function has a singularity at the origin, which will cause infinite self induced velocity of the vortex rings. This result is due to the fact that the induced velocity is affected by the circular core of the vortex ring (Batchelor, 1970). The author remedied this problem by assigning finite core radius equal to one fifth the ring radius. Each vortex ring is convected using the total velocity of the self induced and the velocity induced by other vortex rings on each vortex ring. His results for the mean velocity profiles were nearly in agreement with the measurements of Crow and Champagne (1971). But the root mean square velocity fluctuations were in disagreement with the experiment. The author explained that the difference between the simulation results and the experiment is due to the complexity in the representation of the nozzle surface. Also, he reported that the axisymmetric model and the absence of viscosity led to some turbulence quantities such as velocity fluctuations not well represented.

Some theoretical models for simulating jet flow, as in Acton's approach (1980), are based on the self induced velocity of the vortex ring (Pullin, 1978, 1979; Saffman, 1978). However, Didden (1979, 1982) showed that these models could not simulate exactly the experimental observation of the flow shedding from the jet nozzle. This is due to the failure of the similarity theory to account for the self induced velocity of the vortex ring. Nitsche and Krasny (1994) modelled, using the fully Lagrangian 2D vortex method, the experiment of Didden (1979) in which a jet issuing from a nozzle was generated by

the motion of a piston in a circular tube. The authors simulated the jet shear layer and the nozzle surface by using continuous and bound vortex sheets, respectively, as in Acton (1980). However, they used the vortex blob technique (Chorin and Bernard, 1973) in which a parameter, corresponding to a finite thickness of the vortex ring core radius, was inserted into the Stokes stream function in order to remove the singularity in the stream function. They reported flow visualization, eddies formation and circulation shedding but the mean velocity and turbulence quantities were not reported. In another development, Langthiem and Nakano (2005) simulated a Lagrangian 2D axisymmetric jet impinged on a circular hole in a plate. They modelled the nozzle surface and the plate by bound vortex sheet whereas the shear layer by continuous vortex sheet. Their approach was a combination of the approach used by Acton (1980) and the one used by Nitsche and Krasny (1994). The authors discretized the vortex sheets as Acton's approach (1980) but they utilized the vortex blob technique as in Nitsche and Krasny (1994).

In the literature, there are few studies that use the vortex methods to simulate jet with coflow. Uchiyama (2003) applied 3D vortex method using a Lagrangian approach to simulate an incompressible round jet flow issuing into a coflowing stream. The author simulated the flow inside the nozzle by the panel method (Kiya et al, 1997). The jet nozzle had a circular panel at the bottom with 168 source points distributed on six concentric circles and the panel center to provide the fluid flow. The surface of the nozzle was represented by 32 square panels in the axial and circumferential directions. The flow leaving from the nozzle was simulated by vortex rings as in Acton (1980) and Nitsche and Krasny (1994). The vortex rings were convected with the velocity computed from the Biot-Savart law in which core distribution functions were used (Leonard, 1985;

Winckelmans and Leonard, 1993). His results, including the mean centerline decay and the streamwise mean velocity profiles, were in agreement with the experiment. Recently, Uchiyama and Fukase (2006) applied the 3D methodology following Uchiyama (2003) to simulate gas particle two phase jet flowing from round nozzle into coflowing air stream. Their results showed that the axial turbulent intensity and shear stress were well captured.

2.2 Diffusion-Velocity Method and Deterministic Diffusion

The diffusion-velocity method was introduced by Ogami and Akamatsu (1991) as an alternative technique to the random walk solution of the diffusion equation in order to extend the solution to Reynolds number values below the lower limit of applicability of the random walk. In diffusion-velocity method, the viscous diffusion is generated by the vortices' movement induced by the diffusion velocities which can be accounted as the summary of the contribution from each vortex and are added to the velocities at which the vortices are carried following the procedure of vortex method. Ogami and Akamatsu (1991) found that the diffusion velocity method can simulate problems such as separation and reattachment of the boundary layer without the boundary layer theory. The results for one-dimensional diffusion equation were in agreement with analytical solution. Clarke and Tutty (1994) used the discrete vortex method and applied both the diffusion velocity method and the random walk technique in order to simulate the viscous effect of the two-dimensional Navier-Stokes equations. In this method, the diffusion is limited to regions where the circulation of a single vortex is much larger than a region of low vorticity. The

results were validated in the flow translating circular cylinder and rotating translating circular cylinder. Ogami (1999) used a regridding technique in order to keep the number of vortices from becoming too many and also to position vortices in regions where they are sparse. Lacombe and Mas -Gallic (1999) showed the existence and uniqueness result from diffusion velocity method by solving the one-dimensional, two-dimensional and three-dimensional Navier-Stokes equations. Beaudoin et al. (2003), using the diffusion-velocity method as an alternative to the particle strength exchange (PSE) method, concluded that for anisotropic diffusion problems it is by far easier to derive than that of the PSE method.

The axisymmetric flows include another substep of diffusion called deterministic diffusion. The deterministic diffusion equation is equivalent to the radial movement of the vortex elements. Sod (1978) used the deterministic diffusion as a substep equation in a study for solving equations of gas dynamics for axisymmetric flows. He solved the deterministic diffusion equation analytically by finding the characteristic lines of the equation. In another work concerned with the flow field inside circular geometries, Giovannini (1995) developed the same approach of Sod (1978) in solving the deterministic diffusion equation. The present work simulates the round axisymmetric jet using vortex-in-cell (VIC) method in conjunction with diffusion velocity method that handles the first substep of diffusion in the vorticity equation. The second substep of diffusion is the deterministic diffusion. The Lagrangian-Eulerian vortex-in-cell (VIC) method is used because it combines the best features of Lagrangian and Eulerian methods, i.e., the numerical dissipation is reduced relative to the pure Eulerian method (Sarpkaya, 1994; Ghoneim and Givi, 1987; Leonard, 1980; Chorin and Marsden, 1979) and the

computational time is reduced relative to the Lagrangian method. In the VIC method, an Eulerian scheme is used to calculate the velocity field and a Lagrangian scheme is used to track the vortices. The vortices that represent fluid particles with concentrated vorticity (vortex points or blobs) are tagged and traced in time. As time proceeds, the change of vorticity distribution within a blob is governed by the vorticity transport equation. The justification for this method stems from the fact that, in turbulent flows, vorticity is often very large in thin thread like fluid, while the remaining fluid is virtual without vorticity. Therefore, the vorticity can be lumped into concentrated vortex blobs around which the fluid spins.

2.3 Other Methods Applied in Jets

The jet flow has been simulated extensively in methods different from the vortex methods. These methods involve large eddy simulation (LES), direct numerical simulation (DNS) and Reynolds Averaged Navier Stokes (RANS). Chen et al. (1993) used a LES in conjunction with the Smagorinsky Subgrid scale (SGS) to simulate the proximal region of a round jet flow. The authors reported that the mean velocity was nearly self similar, whereas turbulence statistics were still not fully developed. Verzicco and Orlandi (1994) conducted a DNS and a LES to model 3D round jet flow using both Smagorinsky and dynamic SGS models. They reported that the dynamic SGS model gave better results than the Smagorinsky SGS model. In another simulation, Olsson and Fuchs (1996) performed a LES to simulate the first twelve diameters from the nozzle of a round jet using dynamic SGS model. Their results for the mean flow, the mean centerline decay and vorticity contour were in reasonable agreement with the experiment.

DNS has been applied widely in jet flow simulation. Abid and Brachet (1993) reproduced the rotating streamwise eddies in jet flow. They showed that these eddies play an important role in the transition process of the flow into turbulence. Danaila et al. (1997) used DNS to simulate jet flow at low Reynolds number. Their study was concentrated on the transition from laminar to fully developed turbulent jet flow. They reported that the coherent structures of the flow field in the proximal region were different for low Reynolds numbers. Boersma et al. (1998) conducted full DNS simulation of developing jet flow. Their simulation covered the first forty diameters and was focused on the fully developed region. Their results for mean velocity profile using inflow top hat velocity profile showed good agreement with the experiment but the rms velocity and shear stress were slightly lower than the experiment of Hussein et al. (1994). Sidahmed and Brown (2001) simulated round jet flow using 2D and 3D RANS in FLUENT® code. The authors reported that the 3D scheme results for the mean velocity profiles and the centerline decay agreed well with the experiment. But the results of 2D round jet for the centerline decay overestimated the measured velocities. Gazzah et al. (2004) investigated the influence of a coflow on a turbulent binary gas mixing round jet numerically using first and second order turbulence models. The results of their simulation for the mean flow and the turbulent fluctuations showed that both models were in reasonable agreement with the experimental results.

3.2 Axisymmetric Vorticity Equation without Swirl

In axisymmetric vortex flows the problem is simplified because the velocity components along r and x only are considered. Therefore, the term $\frac{1}{r}\frac{\partial w}{\partial \alpha}$ in Eq.(3) is nil and the continuity equation becomes

$$\frac{\partial v}{\partial r}+\frac{v}{r}+\frac{\partial u}{\partial x}=0 \tag{7}$$

For axisymmetric vortex flows with no swirl ($w=0$), the vorticity vector is directed along the azimuthal direction only (Marshall, 2001). Therefore, the vorticity equations along r [Eq.(4)] and x [Eq.(6)] vanish and Eq.(5) is reduced to

$$\frac{\partial \omega_\alpha}{\partial t}+(\mathbf{u}\cdot\nabla)\omega_\alpha=\frac{v\omega_\alpha}{r}+\nu(\nabla^2\omega_\alpha-\frac{\omega_\alpha}{r^2}) \tag{8}$$

$$\nabla^2\omega_\alpha=\frac{1}{r}\frac{\partial}{\partial r}\left(r\frac{\partial \omega_\alpha}{\partial r}\right)+\frac{1}{r^2}\frac{\partial^2\omega_\alpha}{\partial \alpha^2}+\frac{\partial^2\omega_\alpha}{\partial x^2}$$

Expanding Eq.(8), the vorticity equation along α takes the following form

$$\frac{\partial \omega_\alpha}{\partial t}+u\frac{\partial \omega_\alpha}{\partial x}+v\frac{\partial \omega_\alpha}{\partial r}-v\frac{\omega_\alpha}{r}=\nu(\frac{\partial^2\omega_\alpha}{\partial x^2}+\frac{\partial^2\omega_\alpha}{\partial r^2}+\frac{1}{r}\frac{\partial \omega_\alpha}{\partial r}-\frac{\omega_\alpha}{r^2}) \tag{9}$$

Eq.(9) can be rearranged as

$$\frac{\partial \omega_\alpha}{\partial t}+\frac{\partial u\omega_\alpha}{\partial x}-\omega_\alpha\frac{\partial u}{\partial x}+\frac{\partial v\omega_\alpha}{\partial r}-\omega_\alpha\frac{\partial v}{\partial r}-\nu\frac{\omega_\alpha}{r}=\nu(\frac{\partial^2\omega_\alpha}{\partial x^2}+\frac{\partial^2\omega_\alpha}{\partial r^2}+\frac{\partial}{\partial r}(\frac{\omega_\alpha}{r}))\qquad(10)$$

and by using continuity equation [Eq.(7)] some terms will vanish and Eq.(10) is reduced to

$$\frac{\partial \omega_\alpha}{\partial t}+\frac{\partial u\omega_\alpha}{\partial x}+\frac{\partial v\omega_\alpha}{\partial r}=\nu(\frac{\partial^2\omega_\alpha}{\partial x^2}+\frac{\partial^2\omega_\alpha}{\partial r^2}+\frac{\partial}{\partial r}(\frac{\omega_\alpha}{r}))\qquad(11)$$

Rearranging Equation (11) by combining the second order derivatives on the R.H.S. with the convective terms on the L.H.S., the following form can be obtained

$$\frac{\partial \omega_\alpha}{\partial t}+\frac{\partial}{\partial x}[u-\frac{\nu}{\omega_\alpha}\frac{\partial \omega_\alpha}{\partial x}]\omega_\alpha+\frac{\partial}{\partial r}[v-\frac{\nu}{\omega_\alpha}\frac{\partial \omega_\alpha}{\partial r}]\omega_\alpha=\nu(\frac{\partial}{\partial r}(\frac{\omega_\alpha}{r}))\qquad(12)$$

The vorticity vector reduces to one component in the azimuthal α direction,

$$\omega_\alpha=\frac{\partial v}{\partial x}-\frac{\partial u}{\partial r}\qquad(13)$$

Also the velocity can be expressed along x and r in terms of the stream function ψ such that

$$u = \frac{1}{r}\frac{\partial \psi}{\partial r} \quad , \quad v = -\frac{1}{r}\frac{\partial \psi}{\partial x} \tag{14}$$

Substituting the velocity components given by Eq.(14) into Eq.(13), the Poisson's equation is obtained as

$$\frac{\partial^2 \psi}{\partial x^2} + \frac{\partial^2 \psi}{\partial r^2} - \frac{1}{r}\frac{\partial \psi}{\partial r} = -r\omega_\alpha \tag{15}$$

Equations (14) and (15) can be used to determine the velocity field, in which the vorticity distribution is given by the R.H.S. of Eq. (15).

3.3 Numerical Method and Approximation

In this work the method of fractional steps is used to solve the vorticity equation (Eq.(12)). This method is helpful for multidimensional problems and higher order partial differential equations, because it usually reduces the dimensions and order of the equations to a series of steps, each of which involves only one part of the equation. An extensive description of this method may be found in Yanenko (1971).

In vortex method, the solution of the vorticity equation Eq. [(12)] can be split into three fractional steps similar to the procedure followed by Sod (1978); the convection fractional step that describes the convection of the interacting vortices and two diffusion fractional steps.

The equation governing the convection fractional step is

$$\frac{\partial \omega_\alpha}{\partial t} + \frac{\partial u \omega_\alpha}{\partial x} + \frac{\partial v \omega_\alpha}{\partial r} = 0 \tag{16}$$

The equation governing the first diffusion step, which is based on the diffusion velocity method, is given by

$$\frac{\partial \omega_\alpha}{\partial t} + \frac{\partial}{\partial x}(-\frac{\nu}{\omega_\alpha}\frac{\partial \omega_\alpha}{\partial x})\omega_\alpha + \frac{\partial}{\partial r}(-\frac{\nu}{\omega_\alpha}\frac{\partial \omega_\alpha}{\partial r})\omega_\alpha = 0 \tag{17}$$

and the equation governing the second diffusion fractional step is given by the deterministic diffusion

$$\frac{\partial \omega_\alpha}{\partial t} = \nu \frac{\partial}{\partial r}(\frac{\omega_\alpha}{r}) \tag{18}$$

The numerical approximation for the three fractional steps is described in the following subsections.

3.3.1 Numerical Approximation for Poisson's Equation

The first fractional equation Eq.(16) corresponds to the motion of an incompressible, inviscid and axisymmetric fluid flow. It governs the evolution of vorticity that is transported solely by the convection of the fluid. In a vorticity-stream function formulation, the solution of Equation (16) is equivalent to the solution of the

Poisson equation Eq.(15). The Poisson equation is discretized by approximating the derivatives using the second order central finite difference scheme such that

$$\frac{\psi(i+1,j)-2\psi(i,j)+\psi(i-1,j)}{(\Delta x)^2}+\frac{\psi(i,j+1)-2\psi(i,j)+\psi(i,j-1)}{(\Delta r)^2}$$

$$-\frac{1}{(\Delta r)j}\frac{\psi(i,j+1)-\psi(i,j-1)}{2(\Delta r)}=-(\Delta r)j\omega_\alpha(i,j) \tag{19}$$

where Δx and Δr are the grid sizes in the axial and radial directions, respectively, i and j are subscripts along the axial and radial directions, respectively, and $j=1$ corresponds to the centerline axis $r=0$ as shown in Figure (2).

By rearranging Eq.(19) and solving for $\psi(i,j)$, it becomes

$$\psi(i,j)=\left[\begin{array}{l}(\Delta r)^2\psi(i+1,j)+(\Delta r)^2\psi(i-1,j)+\psi(i,j+1)\left(-\frac{(\Delta x)^2}{2j}+(\Delta x)^2\right)\\ +\psi(i,j-1)\left(\frac{(\Delta x)^2}{2j}+(\Delta x)^2\right)+j(\Delta r)^3(\Delta x)^2\omega_\alpha(i,j)\end{array}\Bigg/2(\Delta r)^2+2(\Delta x)^2\right] \tag{20}$$

Equation (20) is solved in order to get $\psi(i,j)$ at each node (i,j) of the computational domain. Then, using Equation (14), the velocity components at the nodes are approximated using central difference scheme for the first derivative as

$$u(i,j)=\frac{1}{j(\Delta r)}\frac{\psi(i,j+1)-\psi(i,j-1)}{2(\Delta r)},\quad v(i,j)=-\frac{1}{j(\Delta r)}\frac{\psi(i+1,j)-\psi(i-1,j)}{2(\Delta x)} \tag{21}$$

The velocity $u(i,j)$ and $v(i,j)$ are used to convect the vortices, vortex-in-cell (VIC) method is used in this work. Details of the numerical scheme using the VIC method are discussed in chapter 4.

3.3.2 Numerical Approximation of the First Diffusion Fractional Step

The second fractional step [Eq.(17)] governs the effect of diffusion on the transport of vorticity but has no effect on the circulation of vortices. Equation (17) can be simulated using either the random–walk method (Chorin, 1973), diffusion velocity method (Ogami and Akamatsu, 1991), the core spreading technique or the particle strength exchange (PSE). The diffusion velocity technique is used in this work. The diffusion velocities are calculated at the nodes as

$$u_{diff} = -\frac{\nu}{\omega_\alpha}\frac{\partial \omega_\alpha}{\partial x} \quad , \quad v_{diff} = -\frac{\nu}{\omega_\alpha}\frac{\partial \omega_\alpha}{\partial r} \tag{22}$$

Then, Eq. (22) is discretized using central difference scheme for the first derivative as,

$$u_{diff}(i,j) = -\frac{\nu}{\omega_\alpha(i,j)}\frac{\omega_\alpha(i+1,j)-\omega_\alpha(i-1,j)}{2(\Delta x)}$$
$$v_{diff}(i,j) = -\frac{\nu}{\omega_\alpha(i,j)}\frac{\omega_\alpha(i,j+1)-\omega_\alpha(i,j-1)}{2(\Delta r)} \tag{23}$$

The diffusion velocities are then transferred to the vortex elements using the interpolation techniques. Further details about this method will be presented in section (4.3).

3.3.3 Numerical Approximation of the Second Diffusion Fractional Step

The third step, Eq.(18), handles the deterministic diffusion (Sod, 1978). Giovannini et al (1995) solved the deterministic diffusion by using an analytical expression. However, in this study the deterministic diffusion Eq. (18) is solved to obtain the change of vorticity $\Delta\omega_\alpha(i,j)$ at the nodes (Liu and Doorly, 1999). The deterministic diffusion, Eq.(18), is approximated using central difference scheme for the first derivative such that

$$\frac{\Delta\omega_\alpha(i,j)}{\Delta t} = \nu\left[\frac{\left(\frac{\omega_\alpha(i,j+1)}{r(i,j+1)} - \frac{\omega_\alpha(i,j-1)}{r(i,j-1)}\right)}{2(\Delta r)}\right] \tag{24}$$

and by rearranging, the change in vorticity $\Delta\omega_\alpha(i,j)$ is given as

$$\Delta\omega_\alpha(i,j) = \nu\frac{\Delta t}{2(\Delta r)}\left[\left(\frac{\omega_\alpha(i,j+1)}{r(i,j+1)} - \frac{\omega_\alpha(i,j-1)}{r(i,j-1)}\right)\right] \tag{25}$$

Chapter 4

Vortex-In-Cell

The vorticity field is discretized into a set of vortex rings which are then lumped into vortex particles. The motion of the vortex particles is governed by the vorticity transport equation [Eq.(12)]. The discretization of the field into vortex particles will be discussed in section (4.1). In the vortex-in-cell method, the vorticity is transferred from the vortex particles to the nodes of a grid, using an interpolation technique which will be discussed in section (4.2). The motion of the vortex particles is traced by splitting the vorticity transport equation into several substeps. In the first substep, the convection of the interacting vortex particles is obtained by first calculating the components of the velocity $\boldsymbol{u}=(U,V)$ at the nodes by solving the Poisson's equation Eq.(15). Then the components of the diffusion velocities are calculated at the nodes as $\left(-\frac{\nu}{\omega_\alpha}\frac{\partial\omega_\alpha}{\partial x}, -\frac{\nu}{\omega_\alpha}\frac{\partial\omega_\alpha}{\partial r}\right)$. The velocity components $\boldsymbol{u}=(U,V)$ and the diffusion velocities at the nodes are transferred to the location of each vortex particle, using an

interpolation technique. Then the vortex particles are convected using the equation of motion of a material point. This step will be discussed in section (4.3). For the deterministic diffusion, a change in the circulation of the vortex particle, due to the change in vorticity, is added to the old circulation of the particle. Therefore, the vortex particle is convected with the sum of the change and old circulation. This step will be discussed at the end of section (4.3).

4.1 Vortex Particles

In vortex methods, the vorticity field is discretized into N_p vortex elements with circulation Γ_i for each, the vorticity field is given as

$$\omega(\mathbf{x}) = \sum_{i=1}^{N_P} \Gamma_i \delta(\mathbf{x} - \mathbf{x}_i) \tag{26}$$

where $\delta(\mathbf{x})$ is the Dirac delta function, $\mathbf{x}$ represents the coordinates at which the vorticity is calculated and $\mathbf{x}_i$ is the coordinates position of the vortex elements. The vortex elements are vortex blobs rather than vortex points because the Biot-Savart law, i.e., the Green's function, has a singularity at the origin. It creates large velocities in its neighbourhood, which causes numerical as well as theoretical instabilities. To remove this difficulty, finite core size vortices or blob vortices may be used (Chorin, 1973). Thus, inside the core, velocity is smooth and finite at the centre of the core. Although this trick creates some errors, it is very effective in removing the singularities from the flow field. With this technique, the velocity field induced by each vortex is quantitatively correct, only away from the centre of the vortices. In the vortex blob approach, the particles have

a core radius σ (in VIC σ is equal the grid size), a volume $\delta\upsilon_i$ and a vorticity vector of magnitude ω_i smoothened within the volume δv_i. For a given vortex particle, the circulation Γ_i is identical to the product of the vorticity and the volume of the vortex particle, $\omega_i\ \delta v_i$, which also represents the contribution of the vortex particle to the vorticity field. Therefore, each vortex particle is completely characterized by (x , Γ_i) and the vorticity field is given as

$$\omega(\mathrm{x}) = \sum_{i=1}^{N_P} \Gamma_i \zeta_\sigma(\mathrm{x} - \mathrm{x}_i) \tag{27}$$

where the smoothing function $\zeta_\sigma(\mathrm{x} - \mathrm{x}_i)$ is expressed as

$$\zeta_\sigma(\mathrm{x} - \mathrm{x}_i) = \frac{1}{\sigma^2}\,\zeta\left(\frac{\mathrm{x} - \mathrm{x}_i}{\sigma}\right) \tag{28}$$

with $\int\zeta(x)\,dx = 1$. For the present formulation, the vorticity field is given as

$$\omega(x) = \frac{1}{\sigma^2}\sum_{i=1}^{N_P} \Gamma_i \zeta\left(\frac{x - x_i}{\sigma}\right)\zeta\left(\frac{r - r_i}{\sigma}\right) \tag{29}$$

where $[(x - x_i)/\sigma\,,\ (r - r_i)/\sigma\ ]$ are the coordinates distance in units of core size.

4.2 Interpolation Scheme

The smoothing function used is the area-weighing scheme (Baker, 1979),

$$\zeta(\eta) = (1 - |\eta|) \qquad |\eta| < 1 \tag{30}$$

The interpolation scheme [Eqs.(29) and (30)] is used to transfer the vorticity from the vortex blobs to the nodes of the grid. A vortex blob contributes to the nearest 4 nodes as

shown in Figure (1a) in the area-weighing scheme. The total vorticity at each node is obtained by summing the vorticity contributions of all the vortex particles which are within one grid from that node for the area-weighing scheme. Also since there is at least one vortex blob per grid, therefore the vortex blobs will always overlap. The position vector of the vortex blob center is determined by (x_i, r_i) and is discussed in the next section.

4.3 Convection and Diffusion Velocity

The Poisson's equation Eq.(15) is solved in order to obtain the velocity components at each node by using the central difference approximation for the derivatives. The method is also called the extrapolated Liebmann's method (Abdolhosseini and Milane, 2000). Once the components of the velocity at the nodes $\boldsymbol{u_n}$ $=(U_n, V_n)$ are calculated, the components of the velocity $\boldsymbol{u_i} =(U_i, V_i)$ acting on the center of a vortex blob can be calculated with the interpolation technique as

$$U_i = \sum_n U_n \zeta\left(\frac{x_i - x_n}{\sigma}\right)\zeta\left(\frac{r_i - r_n}{\sigma}\right) \tag{31a}$$

$$V_i = \sum_n V_n \zeta\left(\frac{x_i - x_n}{\sigma}\right)\zeta\left(\frac{r_i - r_n}{\sigma}\right) \tag{31b}$$

where n is the representation of the nearest 4 nodes surrounding the vortex blob in the area-weighing scheme. The position vector of the vortex blob centre $\chi=(x_i, r_i)$ is calculated by integrating the equation of motion of a material point

$$d\chi/dt = \mathbf{u}\,(\chi(r,\alpha,x,t)) \tag{32}$$

using the improved Euler's method where the predictor is

$$\chi(t+\Delta t)= \chi(t)+ \mathbf{u}\,\Delta t \tag{33}$$

Δt is the time-step and the velocity $\mathbf{u} = \boldsymbol{u_i}$. To implement Eq.(33), the calculations are carried out in one step within each time step. In this step, the algorithm is executed using the predictor Eq.(33).

After completing the above operation, the components of the diffusion velocities are calculated at the nodes, $\left(U_{diff} = -\frac{\nu}{\omega_\alpha}\frac{\partial \omega_\alpha}{\partial x}, V_{diff} = -\frac{\nu}{\omega_\alpha}\frac{\partial \omega_\alpha}{\partial r}\right)$, and transferred to the centre of the vortex blob using Eqs.(31a) and (31b). The position vector of the vortex blob is calculated using Eq.(33) in which $\mathbf{u} = \boldsymbol{u_{di}}$. The diffusion velocity could be unreasonably high in regions of small vorticity and non-zero vorticity gradient because it is inversely proportional to the vorticity. This problem is remedied by setting the components of the diffusion velocity to zero whenever the vorticity at the nodes is less than 0.1% of the vorticity associated with vortex particles. Here it is noted that the solution of the Poisson's equation together with the Lagrangian movement of the vortex particles is equivalent to the solution of the convective term $\boldsymbol{u} = (U_n, V_n)$ in Eq.(12).

After calculating the components of the diffusion velocities at the nodes, the change in vorticity at the nodes $\Delta\omega_\alpha(i, j)$ is obtained from Eq. (18). The change in vorticity at the nodes is projected back onto the particle to change its vorticity and subsequently its circulation. The area weighting scheme is used to transfer the change of

vorticity $\Delta\omega_\alpha$ onto the particles within a grid. By using this technique the new circulation of the particle will be

$$\Gamma_i(t+\Delta t) = \Gamma_i(t) + \sum_{z=1}^{4} \Delta\omega_\alpha \frac{A_z}{A_{t_z}} h^2 \tag{34}$$

where h is the grid size and A_{t_z} is the total shaded area or the summation of the shaded area contributed by all particles related with the node (i, j) as shown in Figure (1b) and A_z is the shaded area contributed by each particle related with the node (i, j) (See Figure (1b)). Then the vorticity from the vortex particles is transferred to the nodes using the interpolating scheme [Eqs.(29) and (30)] as mentioned in section (4.2).

4.4 Jet with No Coflow

4.4.1 Boundary and Initial Conditions

The problem to be simulated in the first part of the present work is described as the jet flow issuing into still environment. The jet flow geometry has an axial symmetry. Therefore, the upper half of the jet is taken for the numerical simulation. The computational domain consists of a rectangular grid system with uniform grid size in axial and radial direction $\Delta x \neq \Delta r$, respectively. The grid system is shifted one unit in axial and radial direction such that the centerline $r = 0$, with respect to the jet flow, is located along subscript $j = 1$ as shown in Figure (2). The Neumann condition is applied to

the inflow boundary. At the inflow, the velocity is uniform which is known as the top hat velocity profile such that

$$\begin{aligned} (\partial\psi/\partial r)_{1,j} = rU \qquad & U = U_J \qquad r \le R \\ & U = U_a = 0 \qquad r > R \end{aligned} \tag{35}$$

where subscript j corresponds to the node in the radial direction, R is the radius of the nozzle, U_J and U_a are the velocities of the jet exit flow and the coflowing, respectively. The outflow boundary condition corresponds to the convective outflow boundary as

$$(\partial\psi/\partial t)_{M,j} + U_{con}(\partial\psi/\partial x) = 0 \tag{36}$$

where the subscript M corresponds to the last node in the axial direction at the outflow. In convective outflow boundary condition $U_{con} = U_J$ in this work. Because of symmetry about $r = 0$, the axisymmetric boundary conditions can be applied at $r = 0$ as

$$\begin{aligned} (\partial U/\partial r)_{i,1} &= 0 \\ V_{i,1} &= 0 \\ (\partial\psi/\partial x)_{i,1} &= 0 \end{aligned} \tag{37}$$

Therefore, since $V_{i,1} = 0$ this will lead to $(\partial\psi/\partial x)_{i,1} = 0$ because the lateral velocity V is related to the $(\partial\psi/\partial x)$ through Eq. (14). The top boundary condition can be obtained by integrating Eq. (35) such that

$$\psi_{1,N} = \frac{U_a}{2} r_{1,N}^2 + \left(\frac{U_J - U_a}{2}\right) R^2 \tag{38}$$

where N corresponds to the last node in the radial direction. The jet shear layer issued from the nozzle is simulated using a continuous vortex sheet discretized into vortex rings. Then, the vortex rings are lumped into a row of vortex particles or blobs located at the level of the upper half of the nozzle. Initially, the vortex particles are equidistant, and are separated by a distance $d = H/N_v$, where N_v is the number of vortices and $H = \Delta x M$ is the length of the computational domain. At time $t = 0$, the vortex closest to the edge of the nozzle is moved vertically a small distance $0.5d$ to initialize the Kelvin-Helmholtz instability. The circulation is distributed equally among the vortices N_v as $\Gamma_i = d\Delta U$ where $\Delta U = U_J - U_a$. If at the end of each time step Δt, defined as the characteristic time $\Delta t = d/U_c$ where $U_c = (U_J + U_a)/2$, a vortex element with circulation Γ_i is generated at the edge of the nozzle at $x = 1$ and $r = R$, the vorticity generation rate is $\Gamma_i/\Delta t = \Delta U U_c$ and therefore the Kutta condition is satisfied. When the vortex element is generated at the edge of the nozzle, the vortex element with the largest residence time is discarded. The vortex elements can move freely in and out through the outflow boundary to avoid the collection of vortices at the end of the computational domain. The motion of the vortices outside the computational domain is assumed to be governed by the velocity at the outflow boundary.

Another inflow boundary condition will be tested in the present simulation. This boundary condition is of Neumann type which is applied at the inflow of the computational domain beyond the potential core such that

$$(\partial\psi/\partial r)_{1,j} = rU_{1,j} \qquad U_{1,j} \text{ for } 0 \le r \le r_N \tag{39}$$

where r_N is the radial distance up to the last node in the radial direction, and $U_{1,j}$ is given by the self similar profile as

$$U_{1,j} = \frac{U}{(1+a\eta^2)^2}$$

where $a = \left(\sqrt{2}-1\right)/S^2$, $S = 0.094$ is the spreading rate from the experiment of Hussein et al (1994), $\eta = r/(x-x_0)$ is the similarity variable where, $x_0 = 4D$ is the virtual origin (Hussein et al, 1994); the velocity U in the numerator of self similar profile is obtained from the following equation

$$U = \frac{B_u U_J}{\left(\frac{x}{D} - \frac{x_0}{D}\right)}$$

where $B_u = 5.8$ is an experimental constant. The top boundary condition is represented by

$$(\partial\psi/\partial r)_{1,N} = rU_{1,N} \qquad U_{1,N} \text{ for } r = r_N \tag{40}$$

where $U_{1,N}$ is the velocity at the last node in the radial direction obtained from the self similar profile. The outflow and bottom boundary conditions are as Equations (36) and (37), respectively.

In this work, the initialization of the vorticity field using the Stokes stream function $\psi(x,r)$ is tested. The Stokes stream function is given as

$$\psi(x,r)=\frac{\Gamma}{2\pi}(\eta_1+\eta_2)(K(\lambda)-E(\lambda)) \tag{41}$$

where $\lambda=(\eta_2-\eta_1)/(\eta_2+\eta_1)$,

$$\eta_1=\left[(x-x_i)^2+(r-r_i)^2+\varepsilon^2\right]^{1/2},$$

and $\eta_2=\left[(x-x_i)^2+(r+r_i)^2+\varepsilon^2\right]^{1/2}$

ε is the vortex blob smoothing parameter corresponds to finite thickness equal to 0.01, $K(\lambda)$ and $E(\lambda)$ are the complete elliptic integrals of the first and second kind, respectively, given as $K(\lambda)=\int_0^{\pi/2}\left(1-\lambda^2\sin^2\theta\right)^{-1/2}d\theta$, $E(\lambda)=\int_0^{\pi/2}\left(1-\lambda^2\sin^2\theta\right)^{1/2}d\theta$.

4.4.2 Solution Procedure

The solution procedure to solve the velocity and vorticity fields consists in the following steps:

(a) Initializing by placing the equidistant vortices at the level of the nozzle edge and by assuming arbitrary values for ψ at the internal nodes together with the boundary conditions [Eqs.(35)-(38)].

(b) Distributing the vorticity from the vortex particles to the nodes using the interpolation scheme [Eqs.(29) and (30)].

(c) Solving the Poisson's equation [Eq.(15)], using a Gauss-Seidel iteration with a left-to-right sweep of the nodes and bottom-up sweep of the lines. Iteration convergence is obtained when the percent difference between consecutive ψ is less than 0.001%.

(d) Computing the velocities U and V at the nodes using Eq.(14).

(e) Calculating the velocities at the location of each vortex (U_n , V_n) using the interpolation scheme [Eqs.(31a) and (31b)].

(f) Updating the co-ordinates of the vortices using Eq.(33).

(g) Computing the component of diffusion velocity $\left(-\frac{\nu}{\omega_\alpha}\frac{\partial \omega_\alpha}{\partial x} , -\frac{\nu}{\omega_\alpha}\frac{\partial \omega_\alpha}{\partial r} \right)$ at the nodes.

(h) Computing the change of vorticity $\Delta\omega_\alpha(i,j)$ at the nodes using Eq.(18) and then projecting the change $\Delta\omega_\alpha$ to the particle using Eq.(34).

(i) Calculating the diffusion velocity at the location of each vortex using the interpolation scheme [Eqs.(31a) and (31b)] where (U_n, V_n) is replaced by the component of diffusion velocity .

(j) Updating the coordinates of the vortices using Eq.(33).

(k) Introducing a new vortex at the edge of the nozzle and discarding the oldest one.

(l) Marching in time by repeating the calculations from step (b) through (k).

4.5 Jet with Coflow

4.5.1 Boundary and Initial Conditions

The problem to be simulated in the second part of the present work is described as the jet flow issuing into the same fluid. The computational domain consists of a rectangular grid system with uniform grid size in axial and radial directions $\Delta x \neq \Delta r$, respectively. The grid system is shifted one unit in axial and radial directions such that the centerline $r = 0$, with respect to the jet flow, is located along subscript $j = 1$ as shown in Figure (3). The Neumann condition is applied to the inflow boundary. At the inflow, i.e., the nozzle exit, the velocity is top hat (uniform velocity) profile and the coflow velocity is uniform such that

$$\left(\partial\psi/\partial r\right)_{1,j} = rU \qquad \begin{array}{ll} U = U_J & r \le R \\ U = U_a & r > R \end{array} \tag{42}$$

where subscript j corresponds to the grids in the radial direction, U_J and U_a are the velocities of the jet exit flow and the coflowing, respectively. The outflow boundary condition corresponds to the convective outflow boundary as

$$(\partial\psi/\partial t)_{M,j} + U_{con}(\partial\psi/\partial x) = 0 \tag{43}$$

where the subscript M corresponds to the last node in the axial direction at the outflow, j corresponds to the node in the radial direction. Also, $U_{con} = U_J$ is used in the convective outflow boundary condition. Due to the symmetry about $r = 0$, the axisymmetric boundary conditions can be applied at $r = 0$ as

$$\begin{aligned} (\partial U/\partial r)_{i,1} &= 0 \\ V_{i,1} &= 0 \\ (\partial\psi/\partial x)_{i,1} &= 0 \end{aligned} \tag{44}$$

Therefore, since $V_{i,1} = 0$ this will lead to $(\partial\psi/\partial x)_{i,1} = 0$ because the lateral velocity V is related to the $(\partial\psi/\partial x)$ through Eq. (14). By integrating Eq.(42), the top boundary condition can be obtained as

$$\psi_{1,N} = \frac{U_a}{2} r_{1,N}^2 + \left(\frac{U_J - U_a}{2}\right) R^2 \tag{45}$$

The same approach used in discretizing the vortex elements for jet with no coflow is also applied to jet with coflow.

4.5.2 Solution Procedure

The solution procedure to solve the velocity and vorticity fields consists in the following steps:

(a) Initializing by placing the equidistant vortices at the level of the nozzle edge and by assuming arbitrary values for ψ at the internal nodes together with the boundary conditions [Eqs.(42)-(45)].

(b) Distributing the vorticity from the vortex particles to the nodes using the interpolation scheme [Eqs.(29) and (30)].

(c) Solving the Poisson's equation [Eq.(15)], using a Gauss-Seidel iteration with a left-to-right sweep of the nodes and bottom-to-top sweep of the lines. Iteration convergence is obtained when the percent difference between consecutive ψ is less than 0.001%.

(d) Computing the velocities U and V at the nodes using Eq.(14).

(e) Calculating the velocities at the location of each vortex (U_n , V_n) using the interpolation scheme [Eqs.(31a) and (31b)].

(f) Updating the co-ordinates of the vortices using Eq (33).

(g) Computing the component of diffusion velocity $\left(-\frac{\nu}{\omega_\alpha}\frac{\partial \omega_\alpha}{\partial x}, -\frac{\nu}{\omega_\alpha}\frac{\partial \omega_\alpha}{\partial r}\right)$ at the nodes.

(h) Computing the change of vorticity $\Delta\omega_\alpha(i,j)$ at the nodes using Eq.(18) and then projecting the change $\Delta\omega_\alpha$ to the particle using Eq.(34).

(i) Calculating the diffusion velocity at the location of each vortex using the interpolation scheme [Eqs.(31a) and (31b)] where (U_n, V_n) is replaced by the component of diffusion velocity .

(j) Updating the coordinates of the vortices using Eq. (33).

(k) Introducing a new vortex at the edge of the nozzle and discarding the oldest one.

(l) Marching in time by repeating the calculations from step (b) through (k).

Chapter 5

Results for Axisymmetric Jet with No Coflow

Jet flows were investigated in many studies by experimental measurements and by numerical simulations. The diffusion velocity method and deterministic diffusion simulating molecular diffusion, in conjunction with the vortex-in-cell method for simulating axisymmetric round jet has not yet been presented in previous literature. Therefore, the method will be validated by comparing with the experimental round jet data of Wygnanski & Fiedler (1969) and Hussein et al. (1994), and also by comparing with two dimensional simulation of Sidahmed & Brown (2001) and Chung and Troutt (1988) and three dimensional numerical simulation of Boersma et al. (1998). Results obtained using inflow top hat velocity profile are compared with results using inflow self similar profile. Several initializing methods have been conducted using one sheet and several sheets of vortex elements. In addition, initializing using the Stokes stream function (Lamb, 1932) is conducted. Several flow characteristics are reported and compared: the decay of the streamwise mean centerline velocity, streamwise mean

velocity, root-mean-square (r.m.s.) longitudinal and lateral velocity fluctuations, cross-stream correlation, instantaneous distribution of vortex elements and vorticity contours.

5.1 Numerical Parameters

The jet exit velocity is $U_J = 5620$ cm/s and the diameter of the nozzle is $D = 2.6$ cm, similar to the parameters used in the experiment of Wygnanski & Fiedler (1969). The reported results are for a viscous flow condition with $\nu = 14.5\times10^{-2}$ cm^2/s (the kinematic viscosity of air at 18°C). This leads to Reynolds number $\mathrm{Re}_D = U_J D/\nu = 1.01\mathrm{x}10^5$. The jet flow geometry has an axial symmetry. Therefore, the upper half of the jet is taken for the numerical simulation. The computational domain for the base run consists in a 128×128 grid with uniform grid size equals to $\Delta x = 0.4$ cm in the x-direction and uniform grid equals to $\Delta r = 0.1$ cm in r-direction as shown in Figure (2). At the level of the upper half of the nozzle, the jet shear layer is discretized into a number of N_v =9900 equidistant vortex elements, i.e., one vortex sheet is used. Therefore, the number of vortices per grid is 77, the circulation of each vortex element is $\Gamma_i = 2.91 \times10^{-3}$ m^2/s, and the time step is $\Delta t = d/U_c = 1.84 \times10^{-6}$ s. The top hat inflow profile with one vortex sheet is used for the base run. Sensitivity of the results to the number of vortices and grid size was tested as will be discussed in subsections (5.2.5) and (5.2.6), respectively.

The flow is allowed to develop for 5120 Δt before the statistical calculations are started. Then the mean flow is obtained using time-averaging over the next 15360 Δt, and the rms velocity fluctuations and the cross-stream correlation are calculated using time-averaging over the next 25600 Δt.

5.2 Flow Field Results

5.2.1 Streamwise Centerline Velocity Variation

The streamwise mean centerline velocity U_C along the centerline axis $r = 0$ is normalized by the jet exit velocity U_J, i.e., U_C/U_J and it is plotted in Figures (4a-4b) versus x/D where x is the axial location. Figures (4a-4b) show a comparison with the 2D simulation of Sidahmed & Brown (2001) and 3D simulation of Boersma et al. (1998), respectively. The streamwise mean centerline velocity decay in Figure (4a) is qualitatively similar to the two dimensional simulation of Sidahmed & Brown (2001), although there is a slight difference. Figures (4a-4b) show that U_C/U_J starts to decrease earlier than the 2D and 3D simulations as the distance from the nozzle exit increases. Then, the decay rate of U_C/U_J in the present simulation is slower than that of the 2D and 3D simulations for large value of x/D. In the present simulation $U_C/U_J \approx 0.86$ at $x/D = 15$ but in the 2D and 3D simulations $U_C/U_J \approx 0.69$ and $U_C/U_J \approx 0.6$, respectively, at $x/D = 15$. The difference in the results of the present simulation from those of the 2D and 3D simulations is probably due to the fact that initializing using one sheet of vortex elements is not enough.

The radial profiles of the streamwise mean velocity normalized with the nozzle exit velocity U/U_J is plotted as function of r/D in Figure (5a) for two downstream

stations; where r is the radial distance from the centerline axis and U is the mean streamwise velocity. This Figure shows that at $x/D = 1.8$, U/U_J reaches the free stream at about $r/D = 0.75$; whereas at downstream position $x/D = 13.8$, U/U_J reaches the free stream at $r/D = 1$. Therefore, the prediction indicates that the jet flow spreads as the downstream position increases. The streamwise mean velocity vectors are plotted for three downstream locations in Figure (5b). It can be noted that the streamwise mean velocity spreads laterally outward as the jet flows downstream. The Figure shows that the streamwise mean velocity is qualitatively representing the shape of the streamwise mean velocity of the jet flow.

5.2.2 Mean flow

The streamwise mean velocity U/U_C normalized with the streamwise mean centerline velocity is plotted in Figure (6a) against the similarity variable $\xi = r/r_{1/2}$ at three downstream locations; $r_{1/2}$ is defined as the width at which the mean velocity is equal to half of its value on the centerline. The results are presented in the self preserving region which corresponds to $3 \le x/D \le 19.2$. Figure (6a) shows that the simulation results agree with the experiment of Wygnanski & Fiedler (1969) in the region $0 \le \xi \le 1$ and that the experimental profiles spread more than the simulated profiles beyond $\xi = 1$. The difference between the simulation results and the experiment can be probably due to the variations in inflow conditions between experiment and simulation. In addition, initializing using one sheet of vortex elements might be inadequate.

Figure (6b) shows the streamwise mean velocity normalized with the jet exit velocity as U/U_j versus r/D compared with the 2D simulation of Chung and Troutt (1988) using vortex method at two downstream locations. It is noted that there is agreement between the present simulation and the 2D simulation of Chung and Troutt (1988).

5.2.3 Velocity Fluctuations and Cross Correlation

The rms longitudinal (u'_{rms}) and lateral (v'_{rms}) velocity fluctuations normalized with the mean centerline velocity U_C as function of the similarity variable are shown in Figures (7a) and (7b), respectively. The experimental results of Wygnanski & Fiedler (1969) are shown as a reference, keeping in mind that the 2D simulation is not expected to predict these results as the experiment. The simulated profiles are presented in the self-preserving region at three downstream locations, which is in the region $3 \le x/D \le 19.2$. The u'_{rms} profiles in Figure (7a) show that the simulation profiles have a similar trend as the experiment. Moreover, the simulation profiles are not fully similar close to centerline where $\xi \le 1.5$. The simulated profiles of u'_{rms} have higher values than the experiment at the centerline. This is consistent with the 2D simulation of Acton (1980) who reported similar results for u'_{rms}. Figure (7b) shows that the v'_{rms} profiles are close to the experiment in the region of $2.5 \le \xi \le 1$. The v'_{rms} profiles start by decreasing at $\xi = 1$ and their values are zero at $\xi = 0$ which is different from the experiment. This is due to the axisymmetric nature of the simulation in which the boundary condition at the centerline

($r = 0$) is $V = 0$, i.e., the cross flow is nil. Also, this is consistent with the simulation of Acton (1980) in which the v'_{rms} vanishes at $r = 0$ and therefore the axisymmetric jet is less representative of a real jet. Figures (7a) and (7b) exhibit similar behaviour as the 2D VIC simulation of Knani et al. (2006) who simulated the upper half of plane jet.

The normal axial and lateral stresses normalized by the square of streamwise mean centerline velocity, i.e., $(u'_{rms})^2/(U_C)^2$ and $(v'_{rms})^2/(U_C)^2$, are plotted versus ξ in Figures (8a) and (8b) for two downstream locations, respectively. The simulation results are compared with the experiment of Hussein et al. (1994). The simulation results have a similar trend as the experiment except for $(v'_{rms})^2/(U_C)^2$ close to the centerline. The discrepancy in the results between the present simulation and the experiment is probably due to the imposed boundary condition $V = 0$.

The cross-stream correlation normalized with the square of streamwise mean centerline velocity $u'v'/(U_C)^2$ plotted versus the similarity variable ξ is shown in Figure (9a) and the same plot is magnified in Figure (9b). The normalized cross-stream correlation is small compared to the experimental results of Wygnanski & Fiedler (1969). The reason for this discrepancy is probably due to the nature of axisymmetric simulation. The streamwise and radial vorticity components, which play an important role in the kinetic energy transfer to the fluctuating velocity field, are absent when axisymmetric flow condition is used. As a result the nonlinear effect of turbulence fluctuations produces small cross-stream correlation compared to the experiment. The cross-stream correlation results in the present simulation are similar to those reported in the 2D VIC simulation of Knani et al. (2006) for a plane jet. The authors attributed this result to the nonlinear effect of rms velocity fluctuations.

5.2.4 Vorticity Contour and Vortex Distribution

Figure (10a) shows instantaneous distribution of vortex elements. The Figure indicates that as the flow develops in the downstream position the initially smaller vortices grow and amalgamate with neighbouring vortices to form large structure. The instantaneous distribution of vortex elements is indicative of the initial mushroom-type vortex normally produced by jet. These results are consistent with the simulation of Acton (1980) and Chung and Troutt (1988). Figure (10b) shows the downstream evolution of azimuthal vorticity ω_α contour for levels 0-20000. As the flow develops from the nozzle the vorticity contour spreads. It can be seen from the Figure that the vorticity contour initially exhibits roll up at $x/D = 0.8$ due to Kelvin-Helmholtz instability. The rollup is followed by pairing and then breaking up as the flow changes into turbulence. This is consistent with the flow visualization. The behaviour of the vorticity contour in the azimuthal direction is similar to the vorticity contour of Olsson and Fuchs (1996) in their investigation of round jet using 3D LES.

5.2.5 Sensitivity to the Number of Vortex Elements

The effect of the number of vortex elements N_v on the centerline decay, the mean flow, the rms longitudinal and lateral velocity fluctuations and instantaneous distribution of vortex elements, is investigated using 5 values, N_v= 750, 2560, 3300, 9900 and 19800.

The centerline decay, U_C/U_J, for different numbers of vortex elements N_v is shown in Figure (11a). The sensitivity of the centerline decay to the number of vortex elements is small as shown in Figure (11a) whereas the mean velocity profiles, U/U_C, in Figure (11b) remain insensitive as the number of vortex elements is increased. The rms longitudinal velocity fluctuations, u'_{rms}/U_C, are plotted in Figure (11c) for several values of N_v as a function of the similarity variable ξ. It is noted that u'_{rms}/U_C value at centerline increases from 0.18 for N_v =750 to 0.335 for N_v =19800 vortices. As the number of vortices is increased, the u'_{rms}/U_C value at centerline is approaching the value of 0.335 for N_v =19800 vortices which is close to value of 0.33 for N_v =9900 (base run). The rms lateral velocity fluctuations, v'_{rms}/U_C, are shown in Figure (11d). The sensitivity of rms lateral velocity fluctuations v'_{rms}/U_C to the number of vortices is similar to rms longitudinal velocity fluctuations u'_{rms}/U_C. It can be noted that the peak of v'_{rms}/U_C increases from 0.12 for N_v =750 to 0.25 for N_v =19800 vortices. As the number of vortices is increased, the peak of v'_{rms}/U_C is approaching the value of 0.25 for N_v =19800 which is close to value of 0.245 for N_v =9900 (base run). Table I shows the u'_{rms}/U_C values at centerline and the peak values of v'_{rms}/U_C are increasing with number of vortices and then become insensitive as N_v =9900 (base run) is doubled to N_v =19800 vortices. Therefore the results are insensitive to the number of vortices.

Table I –Sensitivity of root mean square velocity fluctuations to number of vortices

N_v	(u'_{rms}/U_C)	(v'_{rms}/U_C)
750	0.18	0.12
2560	0.26	0.195
3300	0.275	0.21
9900	0.33	0.245
19800	0.335	0.25

Figures (12a-12d) show the instantaneous distribution of vortex elements for N_v=750, 2560, 3300 and 19800 vortices, respectively. The Figures show that as the flow develops the initial vortex forms, and then smaller vortices or eddies grow to form large eddies as the flow develops in the downstream position similar to Figure (10a) for the base run with N_v=9900.

5.2.6 Sensitivity to the Grid Size

The sensitivity of the results to the grid size is tested by comparing results obtained using 128x128 grid system with grid sizes $\Delta x = 0.4$ cm and $\Delta r = 0.1$ cm and N_v=2560 vortices with results obtained using 256x256 grid system with grid sizes $\Delta x = 0.2$ and $\Delta r = 0.05$ cm and N_v=5120 vortices. In the VIC method, the grid sensitivity cannot be tested by just reducing the grid size and keeping other parameters constant, such as number of vortices. This is because reducing the grid size and keeping the number of vortices constant reduces the density of the vortices per grid. Therefore, the

sensitivity of the results to the grid size is obtained by halving the size of the grids and doubling the number of vortices, i.e., N_v=5120. The N_v=2560 vortices is used in the grid size sensitivity test in order to reduce the computational time. The results are compared for the two grid systems in Figures (13a-13d). The centerline decay, U_C/U_J, is plotted in Figure (13a). The centerline decay shows similar behaviour for both cases. The normalized mean streamwise, U/U_C, is plotted in Figure (13b). It can be noted that the profiles of U/U_C for the two cases indicate no significant difference. The normalized rms longitudinal velocity fluctuations, u'_{rms}/U_C, are plotted in Figure (13c). The profiles of u'_{rms}/U_C are close for the two cases. The values of u'_{rms}/U_C at centerline for $x/D = 7.9$ and $x/D = 13.3$ are 0.26 and 0.23, respectively, for the 128x128 grid system. For the 256x256 grid system, the values of u'_{rms}/U_C at centerline for $x/D = 7.9$ and $x/D = 13.3$ are 0.3 and 0.29, respectively. The normalized rms lateral velocity fluctuations, v'_{rms}/U_C, are plotted in Figure (13d). The profiles of v'_{rms}/U_C exhibit a similar trend in both cases. The peak values of v'_{rms}/U_C for $x/D = 7.9$ and $x/D = 13.3$ are 0.2 and 0.17, respectively, for the 128x128 grid system. For the 256x256 grid system, the peak values of v'_{rms}/U_C for $x/D = 7.9$ and $x/D = 13.3$ are 0.22 and 0.21, respectively. Therefore the rms velocity fluctuations have close values in the two grid systems.

5.2.7 Effect of the Convective Outflow Velocity

The convective outflow boundary condition is tested by setting U_{con} in the convective outflow boundary condition [Eq. (36)] equal to $U_{AVG} = 733.8$ cm/s. The velocity U_{AVG} is obtained by integrating the self similar velocity profile $U/(1+a\eta^2)^2$ over the outflow boundary. The results are presented and compared to the case with $U_{con} = U_J$ in Figures (14a-14d). The profiles of U/U_C, u'_{rms}/U_C, v'_{rms}/U_C and $u'v'/U_C^2$ are insensitive to the value of U_{con}. Therefore, $U_{con} = U_{AVG}$ is used in the convective outflow boundary condition in all the runs of this study.

5.2.8 Effect of Perturbation

The flow field is investigated by adding some perturbation to the inflow profile. The perturbation is applied to the top hat velocity profile at the inlet by adding a perturbation to the streamwise velocity. The perturbation is produced by generating Gaussian random numbers multiplied by an experimental fraction of the inlet streamwise velocity. Several fractions in range N_r=0.01-0.2 have been used but their effect on the flow field is not significant, therefore they are not shown. Moreover, a higher value N_r =0.25 has been tested where the results are presented in Figure (15) and Figures (16a-16d). Figure (15) shows a comparison of U_C/U_J for the present simulation between the case with and without perturbation. It can be noted that there is no difference in the decay rate between the two cases.

Figures (16a-16d) show U/U_C, u'_{rms}/U_C, v'_{rms}/U_C and $u'v'/U_C^2$, respectively, for the case without perturbation (dark symbols) and for the case with perturbation (open

symbols). The mean velocity profiles U/U_C are insensitive to the perturbation and coincide in the two cases. For all other profiles in Figures (16b-16d) the effect of perturbation is quite small.

5.3 Effect of Inflow Boundary Condition

Inflow boundary condition is tested by applying the self similar profile $U/(1+a\eta^2)^2$ at the inflow boundary condition and comparing the results with the top hat inflow profile. When the self similar profile is applied to the inflow, a vortex sheet consisting of vortex elements is placed at a level where the velocity gradient $\partial U/\partial r$ is the highest. The vortex elements have equal circulation Γ, which is calculated as $\omega_\alpha \Delta x \Delta r$. The vorticity ω_α is calculated using Eq. (13) where the velocity U is given by self similar velocity profile at the inflow boundary and V is nil. The streamwise mean centerline velocity U_C/U_J is plotted in Figure (17). The results for U/U_C, u'_{rms}/U_C, v'_{rms}/U_C and $u'v'/U_C^2$ are presented in Figures (18a-18d), respectively. The vorticity contour and the instantaneous distribution of vortex elements are plotted in Figures (19a-19b), respectively. Figure (17) shows that U_C/U_J jumps to value higher than unity in an unrealistic behaviour. The centerline velocity, which represents the spreading of the jet, is sensitive to the self preservation conditions but the mean streamwise velocity profiles are self similar (Wygnanski & Fiedler, 1969). Therefore when the self similar profile is applied as inflow boundary condition, it may cause an unrealistic jump to the centerline velocity while the mean velocity profiles remain self

inflow is top hat velocity profile similar to the base run. The streamwise mean centerline velocity U_C/U_J is shown in Figure (20). It can be noted that U_C/U_J is increasing to value higher than unity. The reason is because initializing using the Stokes stream function with one sheet of vortex elements is inadequate. This behaviour of U_C/U_J is remedied by using multiple vortex sheets which lead to a better centerline velocity decay as will be discussed in subsection (5.5.2). Figures (21a-21d) show the profiles of U/U_C, u'_{rms}/U_C, v'_{rms}/U_C and $u'v'/U_C^2$, respectively, for the Stokes stream function (open symbols) compared with the base run (dark symbols). Figure (21a) shows that the profile of U/U_C for the base run is close to the run using the Stokes stream function. The profiles of u'_{rms}/U_C, v'_{rms}/U_C and $u'v'/U_C^2$ obtained using Stokes stream function in Figures (21b-21d) are slightly lower than the profiles of the base run. The difference in results is due to the difference in the initial circulation between the two cases. In the Stokes stream function case the circulation of the vortex elements is higher than the base run. It is twice the circulation in the base run, i.e., 2 times Γ. Therefore, this affects the vorticity field and thus the velocity fluctuations become sensitive to this effect which results in lower values of axial and radial fluctuations. Figures (22a-22b) show the initial vorticity field distribution along the radial direction for the case of one vortex sheet without Stokes (base run) and for the case of one vortex sheet with Stokes, respectively. It can be noted that the vorticity that results from Stokes in Figure (22b) is twice the vorticity that results from one vortex sheet without Stokes (base run) in Figure (22a). Therefore, this leads to two different vorticity field distributions which cause the difference in the results.

Figures (23a-23b) show comparison of vorticity contour for the base run and initializing using the Stokes stream function. There is no significant difference between the two cases. However, the vorticity structures in the case using Stokes in Figure (23b) appear more than the base run in Figure (23a). This is due to the large vorticity that results when Stokes stream function is used. For the two cases, the vorticity contour exhibits initial development near the edge of the nozzle and then breakup as the flow develops in the downstream position due to the effect of the turbulence.

5.5 Initialization of Vorticity-Multiple Vortex Sheets

Initializing the computational domain with several sheets of vortex elements rather than one sheet is accomplished for the top hat profile which is similar to the base run. In addition, the computational domain is initialized with several sheets of vortex elements using Stokes stream function in order to test the flow characteristics. The results for those cases are discussed in details in the next subsections.

5.5.1 Top Hat Profile – Several Sheets

The top hat profile as inflow boundary condition with several vortex sheets of vortex elements are used to initialize the computational domain. The vortex sheets consist of vortex elements which possess the same circulation $\Gamma = \Delta UH / N_v$. As an approximation the circulation of each vortex element is assumed to be the same. Three cases with two, five and ten vortex sheets are used. The sheets are parallel and are

separated equally by vertical distance which varies in each case. One sheet is placed at the level of the upper edge of the nozzle and the next sheet is placed below by a distance equal to the vertical distance. For the two sheets the vertical distance is 0.65. For the five and ten sheets the vertical distance is 0.26 and 0.13, respectively. The results are presented in Figures (24-26). Table II presents a summary of statistic results Figures of different rows of vortex elements.

Table II – Figures for statistic results

Number of Sheets	Figure	N_v
2 sheets	Figures (24a-24d)	6400
5 sheets	Figures (25a-25d)	6400
10 sheets	Figures (26a-26d)	6400

Figures (24a-24c), Figures (25a-25c) and Figures (26a-26c) compare the base run consisting of one sheet and top hat inflow profile with two, five and ten sheets together with the experiment of Wygnanski & Fiedler (1969) (dark diamond and circle symbols). Figures (24d), (25d) and (26d) compare the one sheet (base run) with two, five and ten sheets, respectively. The experiment is not shown in Figures (24d), (25d) and (26d) because the range of the cross-stream correlation in the experiment is outside the bound used in the Figures. It can be noted from Figures (24a), (25a) and (26a) that the streamwise mean velocity profiles are insensitive to the initialization of vorticity for the case of two sheets, but there is a slight difference for cases of five and ten sheets; they spread further in the free stream close to the experiment of Wygnanski & Fiedler (1969). However, the profiles of u'_{rms}/U_C and v'_{rms}/U_C are decreasing as the number of vortex

sheets is increasing as shown in Figures (24b-24c), (25b-25c) and (26b-26c), respectively. The profiles of $u'v'/U_C^2$ in Figures (24d), (25d) and (26d) are reaching zero value as the number of sheets is increasing. The difference in results is due to different initializations. The present 2D simulation is unexpected to predict the rms velocity fluctuations as the 3D simulation and experiment because the streamwise and radial vorticity components are absent and also at the centerline ($r = 0$) $V = 0$, i.e., the cross flow is nil.

The effect of initialization of vorticity on the decay of U_C is investigated for two, five and ten sheets using top hat profile as inflow boundary condition. Figures (27a –27d) show a comparison of the present simulation with the 2D simulation of Sidahmed & Brown (2001). Figures (27b –27d) show that the decay of U_C/U_J for the present simulation is close to the 2D simulation of Sidahmed & Brown (2001). It is noted that U_C/U_J in Figures (27b –27d) is initially constant and then starts to decay at a faster rate than the decay of U_C/U_J in the base run shown in Figure (27a). The reason is because initializing with several sheets of vortex elements, several layers of nodes have initially non zero vorticity value, unlike the case with one sheet where only one layer of nodes has initially non zero value. The case with ten vortex sheets in Figure (27d) shows a faster decay rate of U_C/U_J because more nodes are influenced by vorticity in the case of ten sheets than in other cases.

Figures (28a-28d) show the vorticity contour for cases of one, two, five and ten vortex sheets, respectively. It can be noted that as the number of sheets is increased, the flow structure starts to appear in region close to centerline. But for all cases the flow starts to develop approximately at $r/D \approx 0.5$. After the flow develops, the vorticity

contour spreads and then breaks up in the downstream position due to the turbulence effect.

5.5.1.1 Sensitivity to Number of Vortex Elements

The sensitivity of the centerline decay, mean flow, the root mean square (rms) longitudinal and lateral velocity fluctuations to the number of vortex elements using five sheets is investigated. Two values of N_v=9900 and N_v=6400 vortices are used. The results are plotted and compared in Figures (29a-29d). The centerline decay, U_C/U_J, shows similar decay rate in both cases as shown in Figure (29a).The normalized mean velocity profiles U/U_C are insensitive to the number of the vortex elements used for the two cases as shown in Figure (29b). The normalized rms longitudinal velocity fluctuations, u'_{rms}/U_C, exhibit the same trend in both cases as shown in Figure (29c). The u'_{rms}/U_C values at centerline are 0.06 at $x/D = 7.9$ and 0.09 at $x/D = 13.3$ for N_v=9900 and 0.055 at $x/D = 7.9$ and 0.085 at $x/D = 13.3$ for N_v=6400. Similarly, the normalized rms lateral velocity fluctuations, v'_{rms}/U_C, show similar behaviour for both cases as shown in Figure (29d). The peak values of v'_{rms}/U_C are 0.06 at $x/D = 7.9$ and 13.3 for N_v=9900 and 0.0575 at $x/D = 7.9$ and 0.053 at $x/D = 13.3$ for N_v=6400 vortices. Therefore, the rms velocity fluctuations' values are close in both cases.

5.5.1.2 Sensitivity to Convective Outflow Velocity

The sensitivity to the convective outflow velocity is tested using five sheets of vortex elements. The convective velocity U_{con} in the convective outflow boundary condition [Eq. (36)] is set equal to $U_{AVG} = 733.8$ cm/s similar to subsection (5.2.7). The results are presented and compared to the case with $U_{con} = U_J$ in Figures (30a-30d). The profiles of U/U_C are insensitive to the value of U_{con}. The profiles of u'_{rms}/U_C, v'_{rms}/U_C and $u'v'/U_C^2$ are close to each other, although they exhibit a slight difference between the two cases.

5.5.2 Stokes Stream Function

In this test, the Stokes stream function (Lamb, 1932) is used to initialize the computational domain with vorticity similar to section (5.4) but the circulation of the vortex elements in Eq. (41) is $\Gamma = \Delta UH / N_v$. This test is applied for five and ten sheets of vortex elements where the inflow is top hat velocity profile similar to the base run. The results for five and ten sheets of vortex elements (open symbols) are compared with the run using the Stokes stream function with one sheet of vortex elements (dark symbols) together with the experiment of Wygnanski & Fiedler (1969) (dark diamond and circle symbols) as shown in Figures (31a-31c) and (32a-32c), respectively. Figures (31d) and (32d) show the cross-stream correlation for five and ten sheets of vortex elements (open symbols) compared with the run using the Stokes stream function with one sheet of vortex elements (dark symbols). Figures (31a) and (32a) show that U/U_C for one sheet has similar behaviour when compared with five and ten sheets. The profiles of

U/U_C reach the free stream earlier than the experiment. The profiles of u'_{rms}/U_C and v'_{rms}/U_C in Figures (31b-31c) and (32b-32c), respectively, are decreasing as the number of sheets is increasing. The profiles of $u'v'/U_C^2$ in Figures (31d) and (32d) are reaching zero value as the number of sheets is increasing. The difference in results is due to the fact that in Stokes stream function case with several sheets the circulation of the vortex elements is higher than the circulation in the case for one sheet. As a result, the velocity fluctuations are sensitive to this effect which causes lower values as number of sheets is increased.

Figures (33a-33b) show comparison of the present simulation using five and ten sheets of vortex elements, respectively, with the 2D simulation of Sidahmed & Brown (2001). Figure (33b) shows that the present simulation decay U_C/U_J for case with ten sheets is closer to the 2D simulation of Sidahmed & Brown (2001) than the decay for the case with five sheets in Figure (33a). It is noted that U_C/U_J in Figure (33b) is initially constant and then starts to decay at a faster rate.

Chapter 6

Results for Axisymmetric Jet with Coflow

6.1 Numerical Parameters

The jet issuing with jet exit velocity $U_J = 5620$ cm/s from a round nozzle of diameter $D = 2.6$ cm into the same fluid coflowing with velocity $U_a = 1518$ cm/s is investigated. The velocity ratio is $\gamma = U_a/U_J = 0.27$ whereas the Reynolds number is $\mathrm{Re}_D = U_J D/\nu = 1.01\text{x}10^5$. The study is done on the same 128x128 grid system of the jet with no coflow with uniform grid size equals to $\Delta x = 0.4$ cm in the x-direction and uniform grid size equals to $\Delta r = 0.1$ cm in r-direction as shown in Figure (3). The upper half of the jet is considered such that at the level of the upper half of the nozzle edge the jet shear layer is discretized into a number of vortex elements N_v=9900 vortices each with $\Gamma_i = 2.12\times10^{-3}$ m^2/s, and the size of the time step $\Delta t = d/U_c = 1.45\times10^{-6}$ s. The run with one sheet of vortex elements using top hat inflow velocity profile is chosen as the base

run. Initializing the computational domain with ten sheets of vortex elements is tested and compared with the base run. Several flow characteristics such as the streamwise mean centerline velocity, streamwise mean velocity profiles, root mean square (rms) longitudinal and lateral velocity fluctuations, cross-stream correlation, vorticity contour and the instantaneous distribution of the vortex elements are reported. The results are validated by comparing with the experimental data of Forstall and Shapiro (1950) and Antonia and Bilger (1973), and also by comparing with the three dimensional numerical simulation of Uchiyama (2003) using vortex method.

The flow is allowed to develop for 5120 Δt then the statistical calculations are started. The mean flow is obtained using time-averaging over the next 15360 Δt, and the rms velocity fluctuations and the cross-stream correlation are calculated using time-averaging over the next 25600 Δt.

6.2 Flow Field Results

6.2.1 Streamwise Centerline Velocity Variation

The streamwise mean centerline velocity normalized with the difference between the jet velocity and the coflowing velocity $(U_C - U_a)/(U_J - U_a)$ versus the axial location x/D is plotted in Figure (34a) and compared with the experiment of Forstall and Shapiro (1950). Also, $(U_C - U_a)/(U_J - U_a)$ versus x/D is shown in Figure (34b) with the 3D simulation of Uchiyama (2003). The present simulation shows that U_C is approximately constant until $x/D = 2$ and then decreases faster than the experiment and the 3D

simulation. The streamwise mean centerline velocity U_C in the present simulation is below the experiment in Figure (34a) at $2 \le x/D \le 6.5$ and then continues to decrease gradually at $x/D \ge 6.5$ but at a slower rate, i.e., it is higher than the experiment at $x/D \ge 6.5$. In Figure (34b), U_C in the present simulation is below the 3D simulation at $2 \le x/D \le 8.5$ and then continues to decrease slowly at $x/D \ge 8.5$. The difference between the present simulation and the experimental results are due to the difference in inflow conditions. The difference between the present simulation and the 3D simulation is probably due to the initialization of vorticity in the computational domain which is not adequate with one sheet of vortex elements. Moreover, in the 3D simulation of Uchiyama (2003) the panel method and source points were used to model the nozzle whereas in the present simulation the uniform top hat inflow velocity profile and symmetric boundary conditions applied at the centerline axis are used. This can make the difference between the 3D simulation and the present 2D simulation results.

Figure (35a) shows the radial profiles of the streamwise mean velocity normalized with the difference between the jet velocity and the coflowing velocity versus r/D at two downstream locations. The Figure shows that at $x/D = 1.8$ and 13.8, respectively, the velocity reaches the free stream at about $r/D = 0.6$ and 0.95. Whereas for the no coflow case, shown in Figure (35b), and at the same downstream positions $x/D = 1.8$ and 13.8, respectively, the velocity reaches the free stream at $r/D = 0.75$ and 1.05, respectively. Therefore, it can be noted that the spreading of the coflow jet is reduced when compared to the jet with no coflow as found by the simulation of Gazzah et al. (2004).

6.2.2 Mean Velocity

The streamwise mean velocity normalized as $(U-U_a)/(U_C-U_a)$ is shown in Figures (36a-36b) as a function of similarity variable ξ at three downstream positions, where U is the streamwise mean velocity. The present simulation results are compared with the experimental results of Antonia and Bilger (1973) and the 3D simulation of Uchiyama (2003) as shown in Figures (36a-36b), respectively. The results are presented in the self similar region, which is at $13.3 \le x/D \le 19.2$. In the Figures, the present simulation results are close to the experimental results of Antonia and Bilger (1973) and the 3D simulation of Uchiyama (2003) in the region $0 \le \xi \le 1$ close to the centerline. The simulated mean velocity profiles for $\xi > 1$ slowdown and reach the free stream earlier than the experiment and the 3D simulation. The difference between the experimental results and the present simulation results can be due to the difference in inflow conditions between the experiment and the present simulation. The difference between the 3D simulation of Uchiyama (2003) and the present simulation is probably because the nozzle exit in the 3D simulation is simulated by panel method whereas in the present simulation the simulation of the nozzle exit is not accounted.

6.2.3 Velocity Fluctuations and Cross Correlation

The rms longitudinal (u'_{rms}) velocity fluctuation normalized as $u'_{rms}/(U_C-U_a)$ versus ξ is shown in Figures (37a-37b). The present simulation results are compared with the experimental results of Antonia and Bilger (1973) and the 3D simulation of Uchiyama (2003) as shown in Figures (37a-37b), respectively. The $u'_{rms}/(U_C-U_a)$

profiles are shown in the self similar region, which corresponds to $13.3 \le x/D \le 19.2$. The present simulation results of $u'_{rms}/(U_C - U_a)$ exhibit slightly higher values at centerline than the experiment and the 3D simulation as shown in Figures (37a-37b). The present simulation results exhibit a trend similar to the experiment of Antonia and Bilger (1973) as shown in Figure (37a). In the present simulation the value of $u'_{rms}/(U_C - U_a)$ for $x/D = 13.3$ and $x/D = 15.6$ at the centerline is 0.33 which approximately coincides with $u'_{rms}/(U_C - U_a)$ value for $x/D = 76$ in the experiment of Antonia and Bilger (1973). The present simulation results are relatively self similar for $0.85 \le \xi \le 3$ but for $\xi \le 0.85$ the profiles are not fully self similar and this is consistent with the simulation of Uchiyama (2003) in Figure (37b). Also, it is noted that the peak values of $u'_{rms}/(U_C - U_a)$ increase with increasing x similar to the 3D simulation of Uchiyama (2003). The rms lateral velocity fluctuation normalized as $v'_{rms}/(U_C - U_a)$ versus ξ is plotted in Figure (38). The $v'_{rms}/(U_C - U_a)$ profiles are shown in the self similar region, which corresponds to $13.3 \le x/D \le 19.2$. The present simulation results are relatively self similar but for $0.6 \le \xi \le 1.5$ the profiles are not fully self similar. The v'$_{rms}$ profiles start by decreasing at $\xi = 1$ and their values are zero at $\xi = 0$ similar to the no coflow case. This is due to the axisymmetric nature of the simulation in which the imposed boundary condition at the centerline ($r = 0$) is $V = 0$, i.e., the cross flow is nil. Therefore, the present 2D simulation results are not expected to predict these results as the experiment and 3D simulation.

Figure (39a) shows the cross-stream correlation normalized as $u'v'/(U_C - U_a)^2$ versus the similarity variable ξ. The data of $u'v'/(U_C - U_a)^2$ are presented in the region

of $13.3 \leq x/D \leq 19.2$ together with the data from the experiment of Antonia and Bilger (1973). The simulation results in Figure (39a) are magnified in Figure (39b). The present result at $x/D = 13.3$ has a trend similar to the experimental one. In addition, the simulated profiles are nil at $\xi \geq 1.85$ in similar behaviour as the experiment. The reason for the difference between the present simulation and the experiment can be attributed to the nature of axisymmetric simulation. The streamwise and radial vorticity components, which have an important role in the kinetic energy transfer to the fluctuating velocity field, are absent when the axisymmetric flow condition is used. Therefore, as a result the nonlinear effect of turbulence fluctuations produces small cross-stream correlation compared to the experiment.

6.2.4 Vorticity Contour and Vortex Distribution

Figure (40a) shows the instantaneous distribution of the vortex elements. It is noted that smaller vortices form at $1.5 \leq x/D \leq 4$ as the flow develops in the downstream position. These smaller vortices grow and amalgamate with neighbouring vortices to form large structure vortices in the downstream. This is due to the effect of turbulence which acts as the flow develops from the nozzle. The downstream evolution of the azimuthal vorticity contour is shown in Figure (40b). As the flow develops in the downstream position, the vorticity contour spreads downstream. It can be noted that the vorticity contour exhibits initial roll up at $1 \leq x/D \leq 5$ due to Kelvin Helmholtz instability. Then the vorticity structure breaks down into small structures downstream at $x/D \geq 5$ as the flow changes into turbulence.

6.3 Initialization of Vorticity– Multiple Vortex Sheets with Top Hat Inflow

The top hat inflow velocity profile with ten sheets of vortex elements is used to initialize the computational domain. Figure (41) shows the streamwise mean centerline velocity normalized as $(U_C - U_a)/(U_J - U_a)$ compared with the 3D simulation of Uchiyama (2003). The decay of $(U_C - U_a)/(U_J - U_a)$ using ten sheets of vortex elements is closer to the 3D simulation of Uchiyama (2003) than the decay using one sheet in Figure (34). This is because when the computational domain is initialized with several sheets of vortex elements, several layers of nodes have initially non zero vorticity value, unlike the cases of less number of sheets where only few layers of nodes have initially non zero value.

Figures (42a-42d) compare the base run consisting of one sheet with ten sheets of vortex elements. It can be noted from Figure (42a) that the streamwise mean velocity profile $(U - U_a)/(U_C - U_a)$ is relatively sensitive to the initialization of vorticity for the case with ten sheets. The profiles of $u'_{rms}/(U_C - U_a)$ and $v'_{rms}/(U_C - U_a)$ are decreasing in the case with ten vortex sheets as shown in Figures (42b-42c). The profiles of $u'v'/(U_C - U_a)^2$ are almost nil when ten sheets are used. The discrepancy in the results is due to different initializations of vorticity. Moreover, the behaviour of the results is similar to the behaviour in the case with ten sheets in subsection (5.5.1) for jet with no coflow. The present 2D simulation is unexpected to predict the rms velocity fluctuations

as the 3D simulation and experiment because the streamwise and radial vorticity components are absent and also at the centerline ($r = 0$) $V = 0$, i.e., the cross flow is nil.

Chapter 7

Conclusions and Recommendations

7.1 Conclusions

The vortex-in-cell method in conjunction with diffusion velocity method and deterministic diffusion has been developed to simulate an axisymmetric round jet. For one sheet of vortex elements with top hat inflow profile, the mean centerline velocity decay is qualitatively similar to the two dimensional simulation. The streamwise mean velocity is close to the experimental measurements and is also in agreement with axisymmetric 2D simulation. However, the present simulation over predicts the rms longitudinal and lateral fluctuations and leads to lower values of cross-stream correlation u'v' compared to the experiment. The instantaneous distribution of vortex elements shows that the initial development of the jet is in agreement with previous numerical simulation. Moreover, the effect of the inflow boundary conditions is demonstrated by comparing the top hat profile with the jet self similar profile. Although the streamwise mean centerline velocity jumps to values greater than one, the streamwise mean velocity

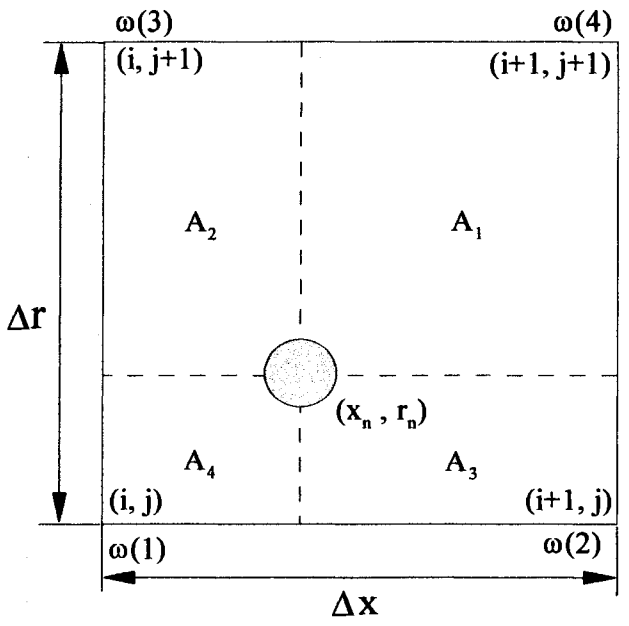

(a)

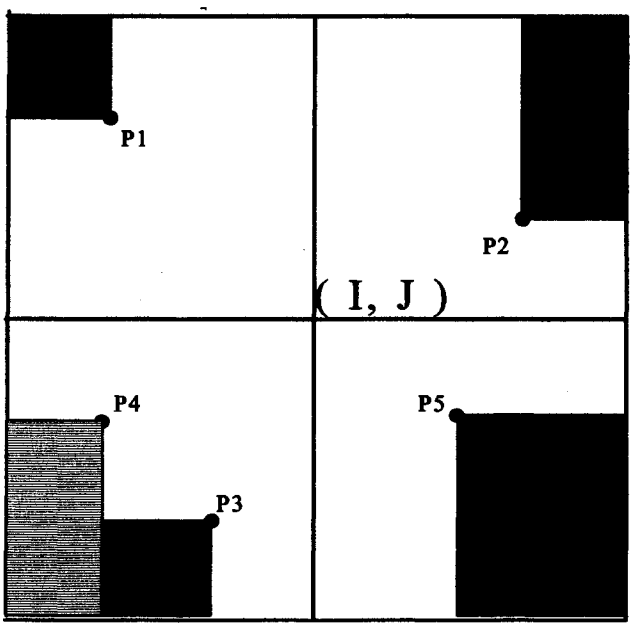

(b)

Figure 1. (a) Two dimensional area-weighting scheme in the VIC method.
(b) Two-dimensional area-weighting scheme to transfer the change of vorticity.

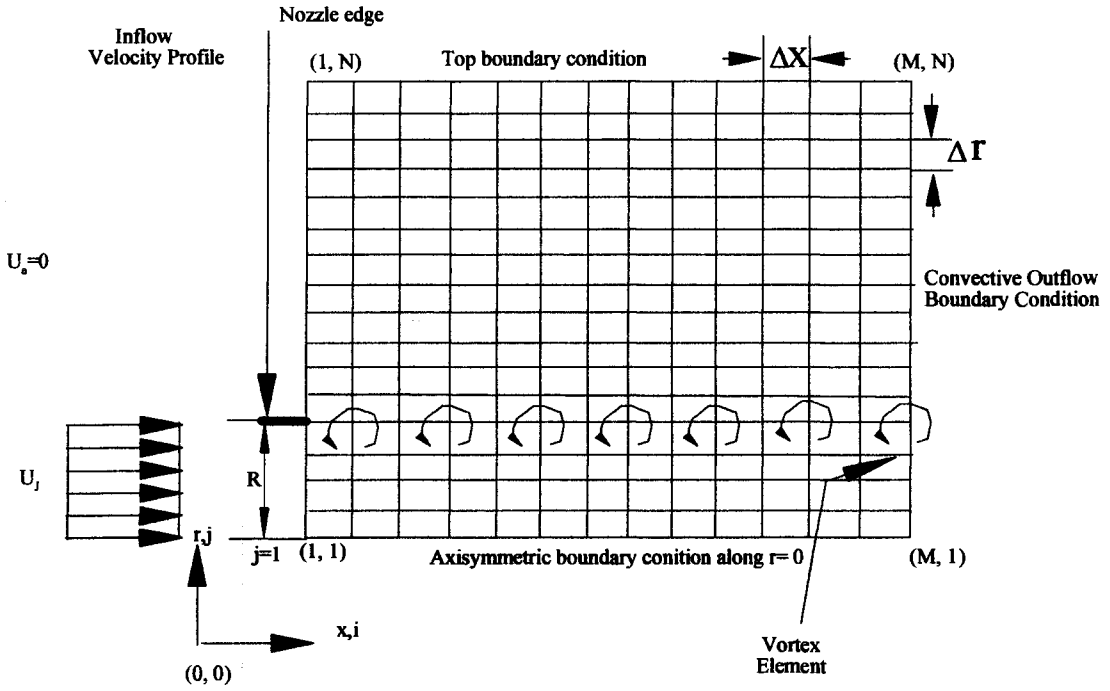

Figure 2. Computational domain for jet with no coflow, rectangular grid, initial position of the vortices and boundary conditions.

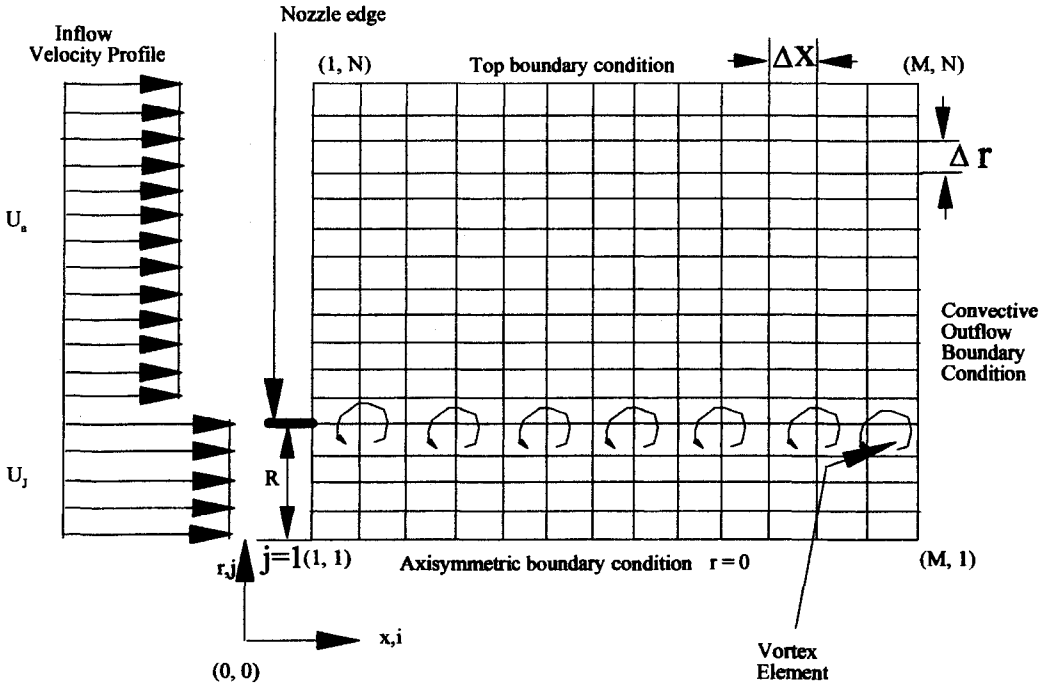

Figure 3. Computational domain for jet with coflow, rectangular grid, initial position of the vortices and boundary conditions.

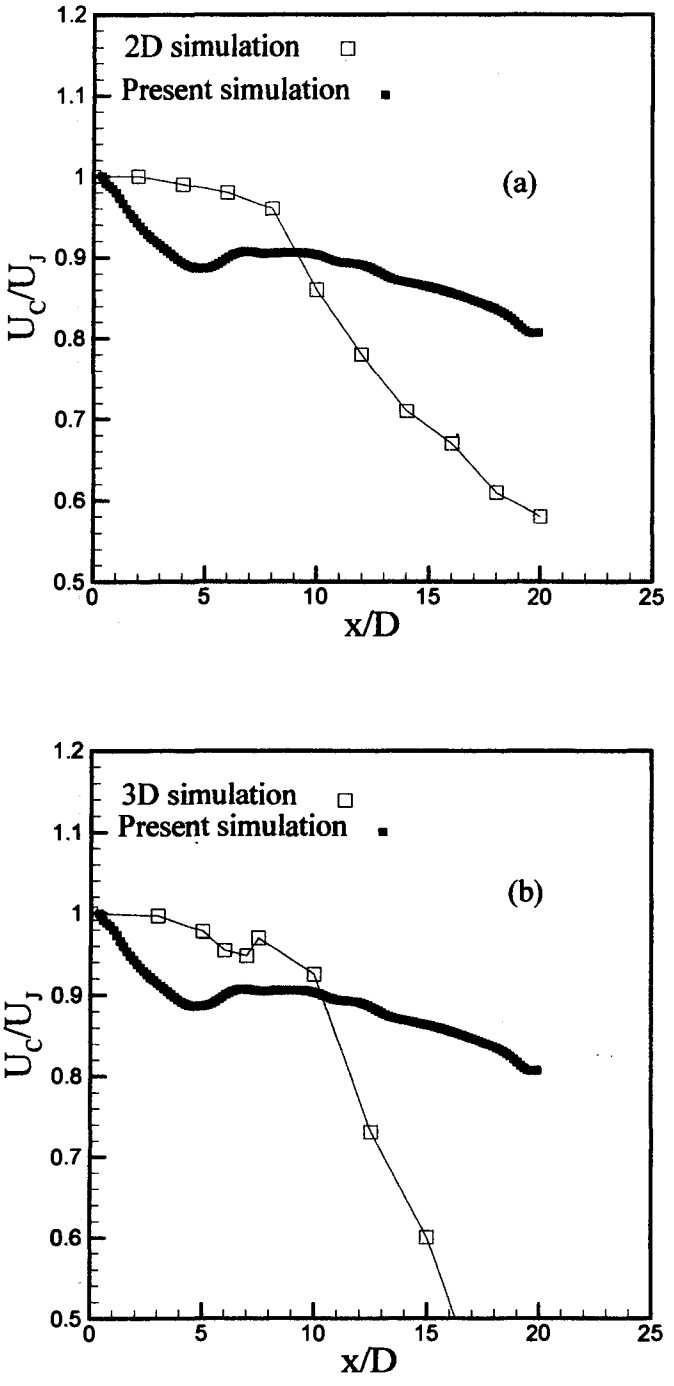

Figure 4. Streamwise mean centerline decay, (a) comparison with 2D simulation of Sidahmed & Brown (2001), (b) comparison with 3D simulation of Boersma et al. (1998).

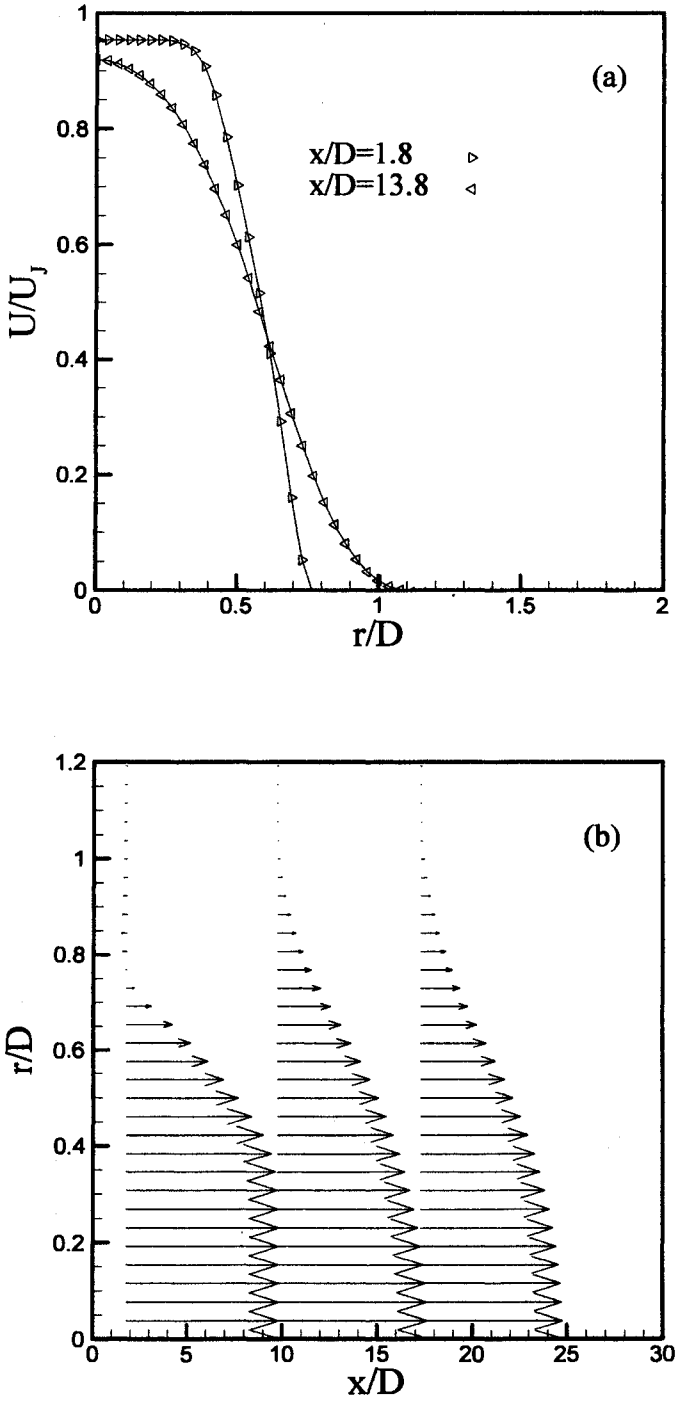

Figure 5. (a) Radial profiles of mean axial velocity showing the spreading of the jet flow at two downstream locations, (b) the streamwise mean velocity profiles of the jet at three axial positions.

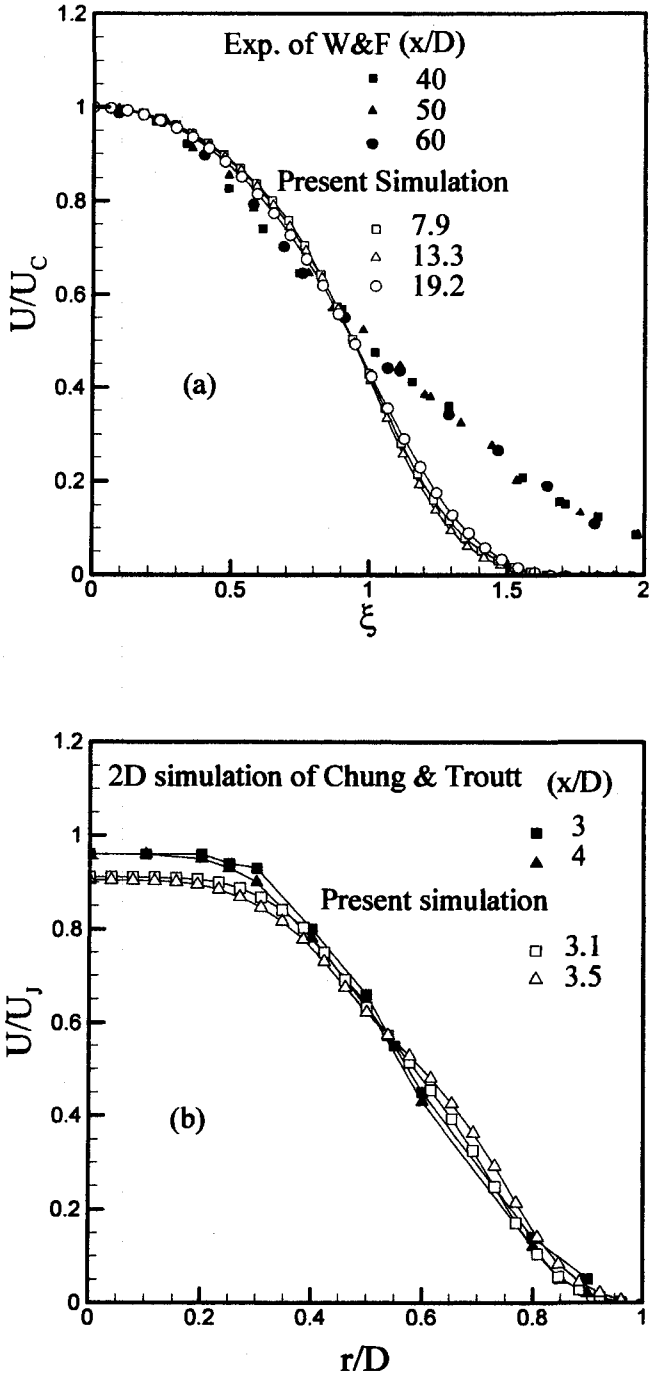

Figure 6. Normalized streamwise mean velocity: (a) present simulation compared with the experiment of Wygnanski & Fiedler (1969), (b) present simulation compared with the 2D simulation of Chung & Troutt (1988).

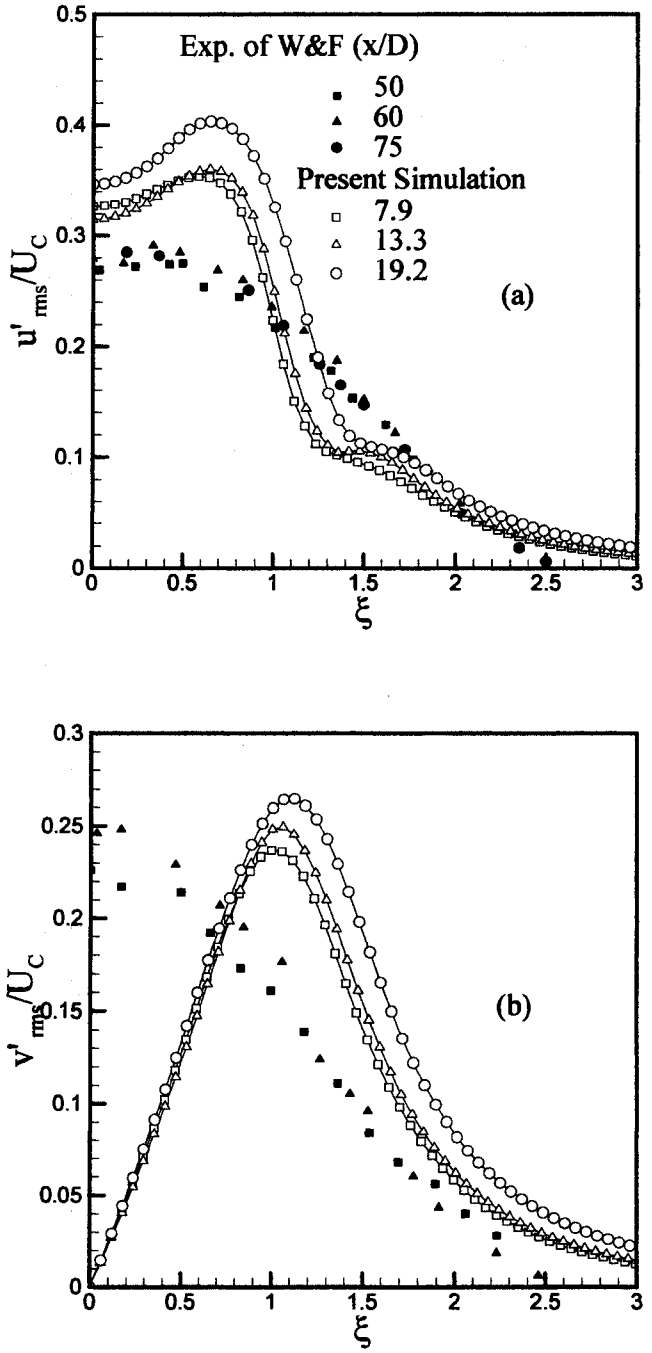

Figure 7. Root mean square fluctuations normalized with the streamwise mean centerline velocity at three downstream locations: (a) rms longitudinal velocity fluctuations, (b) rms lateral velocity fluctuations. The mesh lines connecting the open symbols show the predicted profiles; the dark symbols correspond to the data from the experiment of Wygnanski & Fiedler (1969).

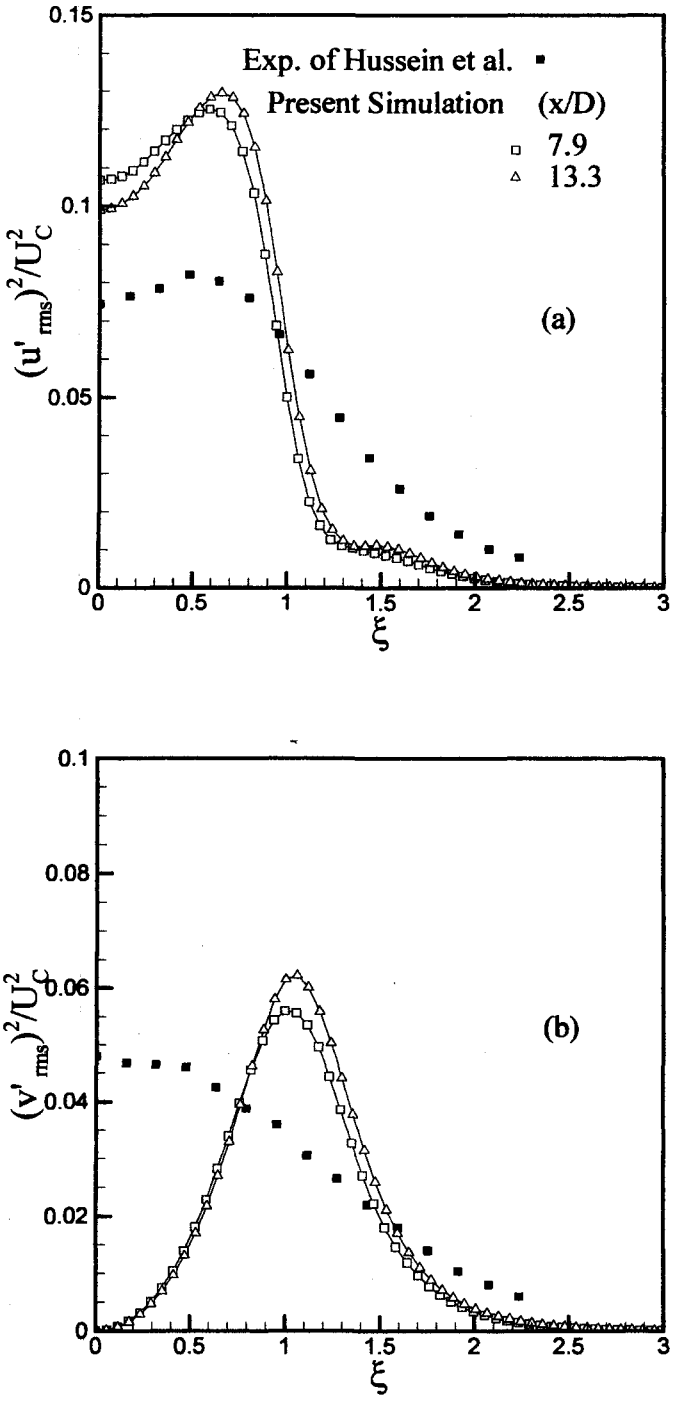

Figure 8. Normal Reynolds stresses normalized with the square of streamwise mean centerline velocity at two downstream locations: (a) longitudinal Reynolds stress, (b) lateral Reynolds stress. The mesh lines connecting the open symbols show the predicted profiles; the dark symbols correspond to the data from the experiment of Hussein et al. (1994).

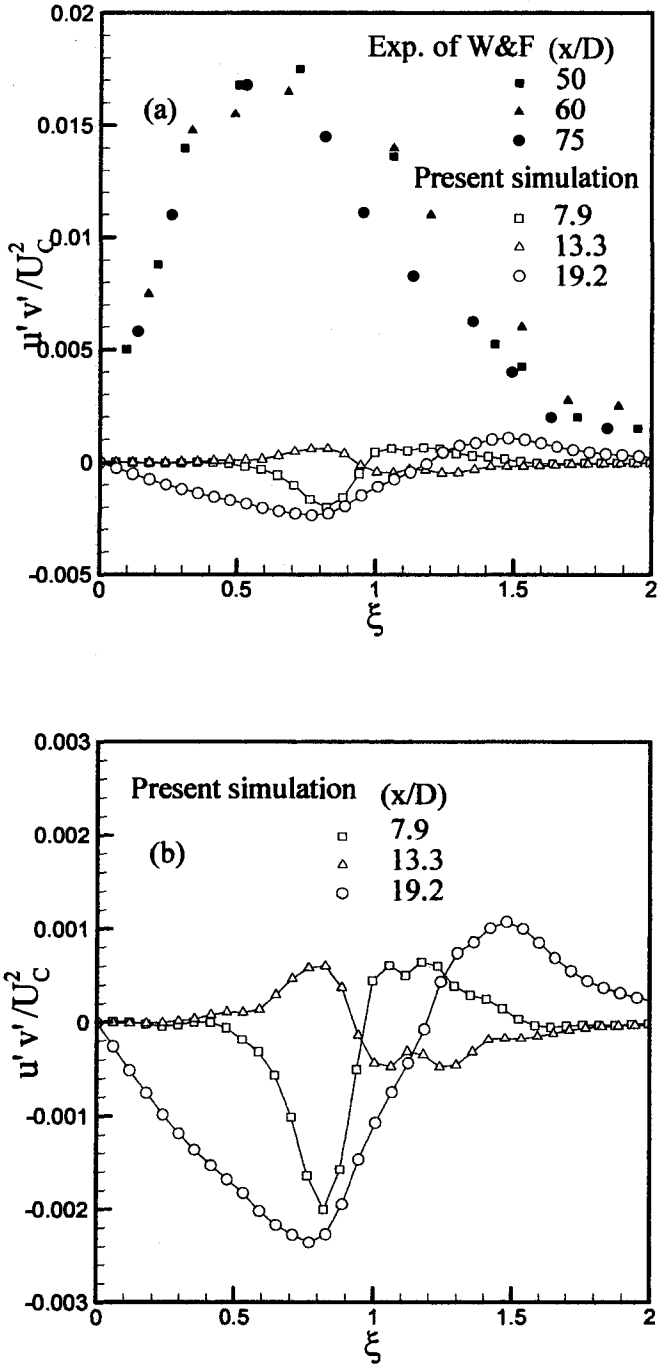

Figure 9. Normalized cross-stream correlation at three downstream locations: (a) comparison with the experiment of W&F, (b) magnifcation of the simulated cross-stream correlation. The mesh lines connecting the open symbols show the predicted profiles; the dark symbols correspond to the data from the experiment of Wygnanski & Fiedler (1969).

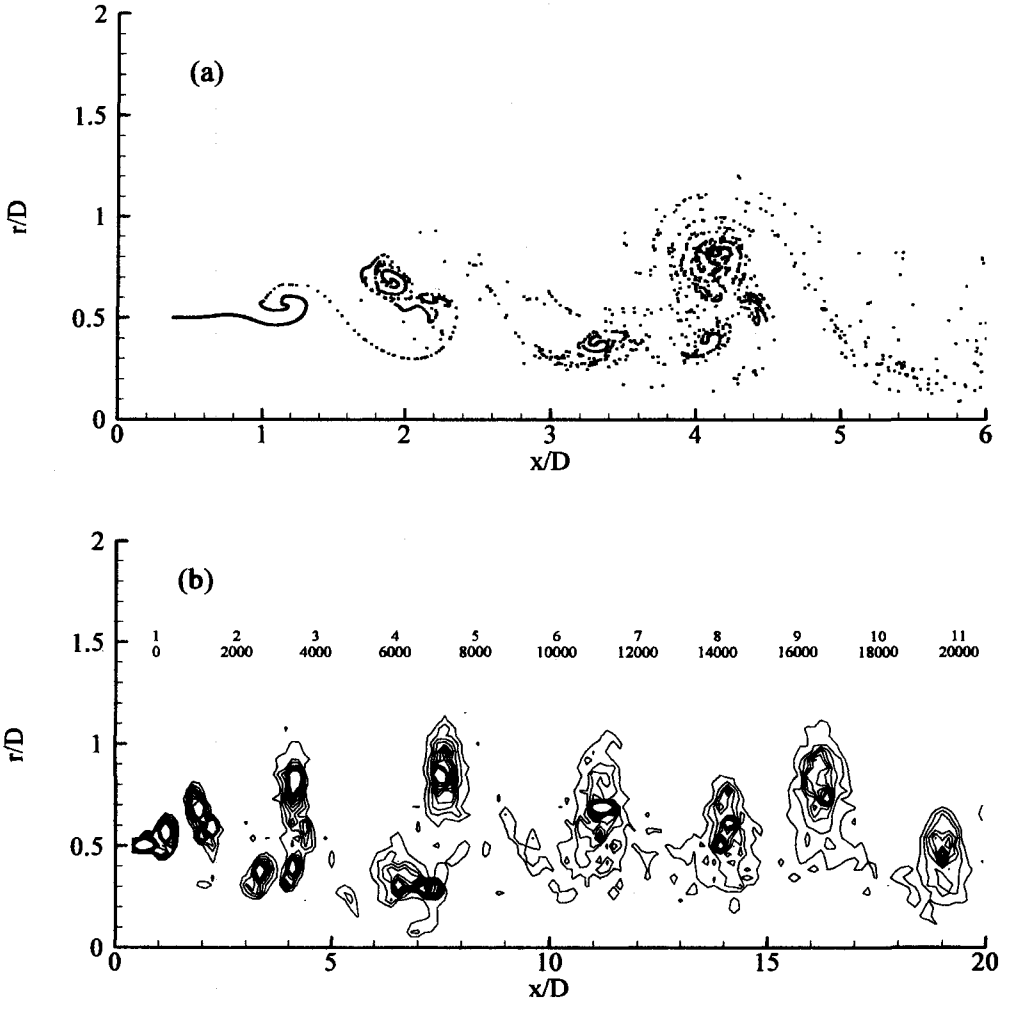

Figure 10. (a) Instantaneous distribution of vortex elements, (b) vorticity contour, contour level increment is 2000.

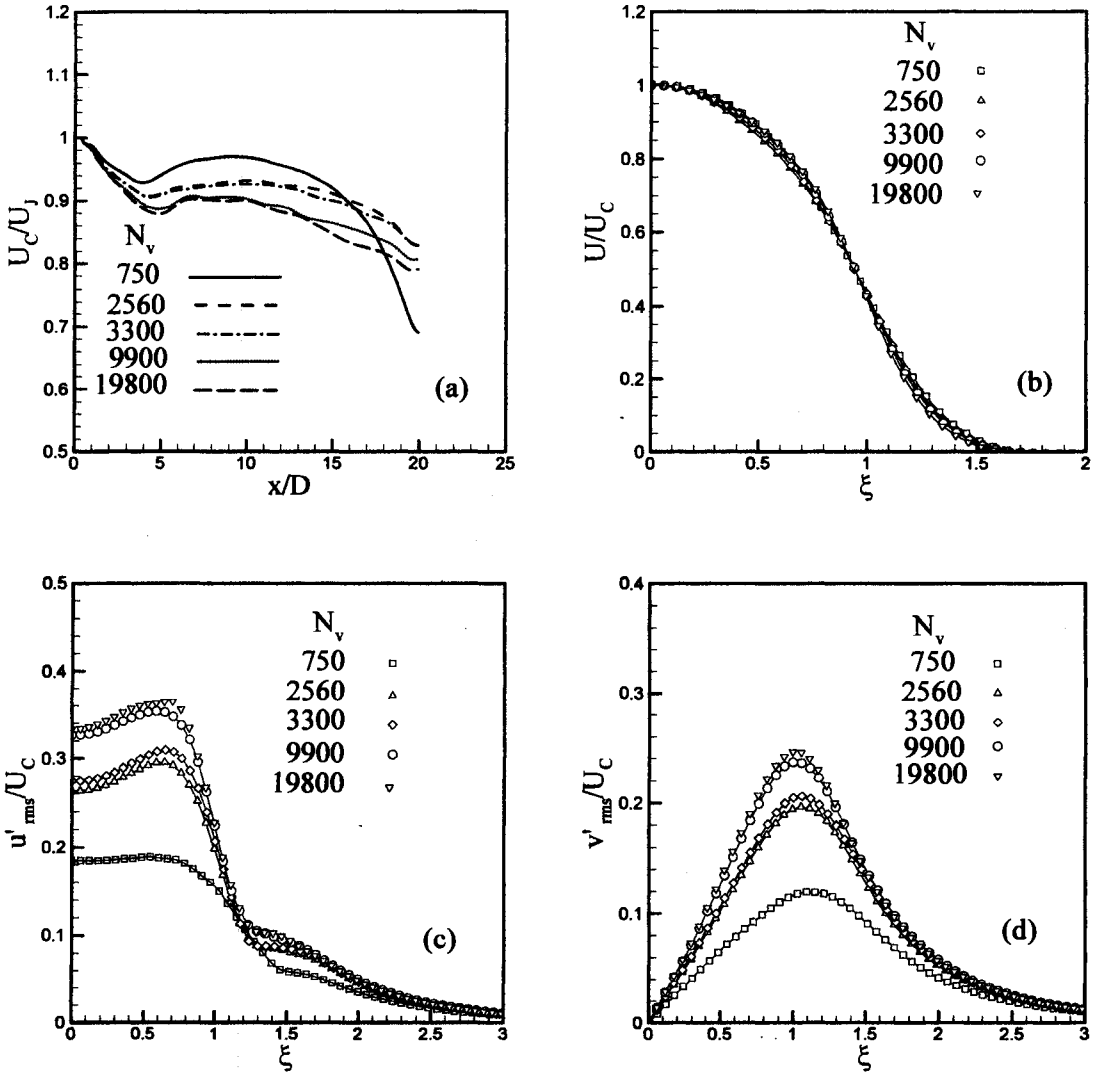

Figure 11. Effect of the number of vortices on (a) streamwise mean centerline decay, (b) streamwise mean velocity , (c) rms longitudinal fluctuations, (d) rms lateral fluctuations.

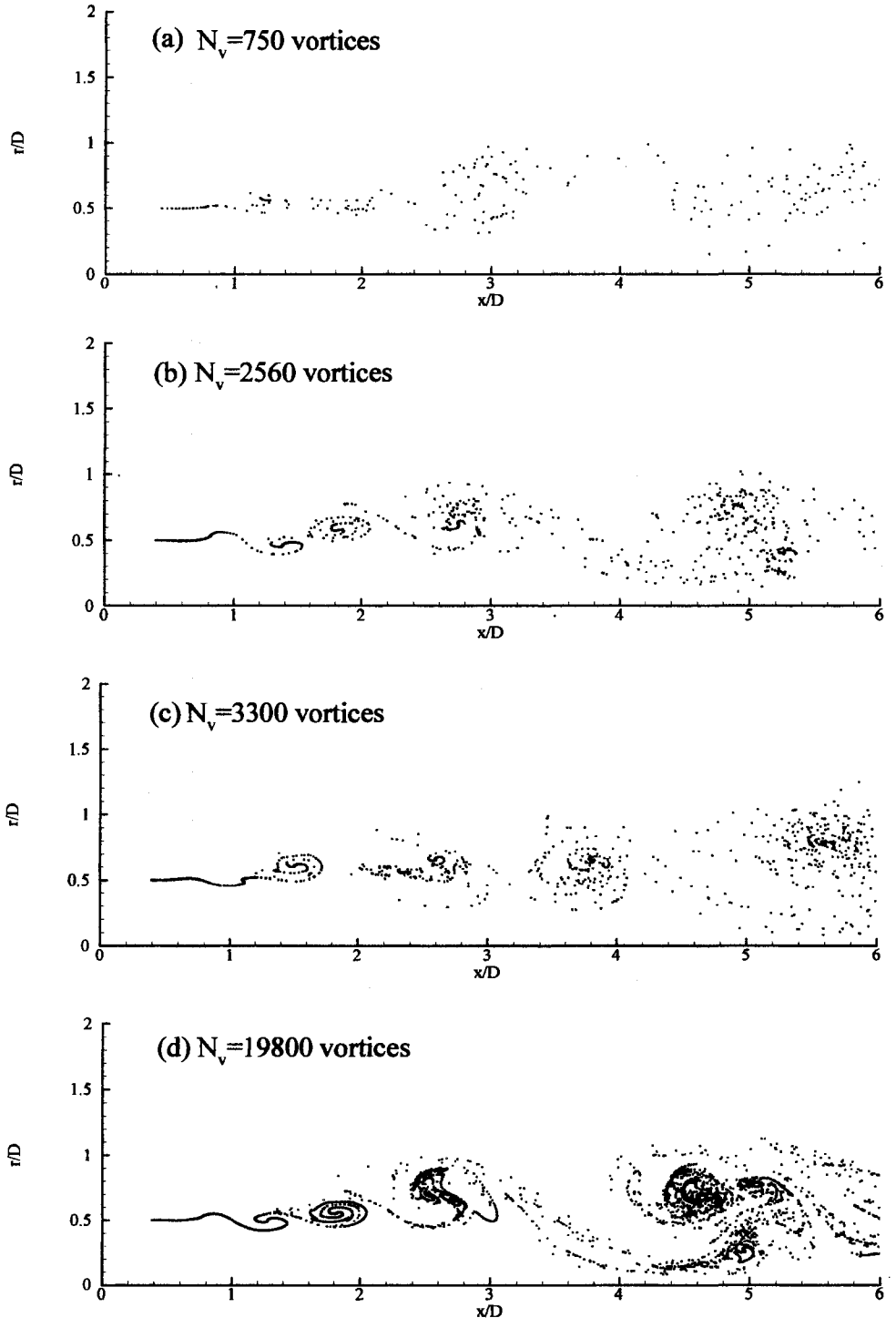

Figure 12. Effect of the number of vortices on vortices distribution: (a) 750 vortices, (b) 2560 vortices, (c) 3300 vortices, (d) 19800 vortices.

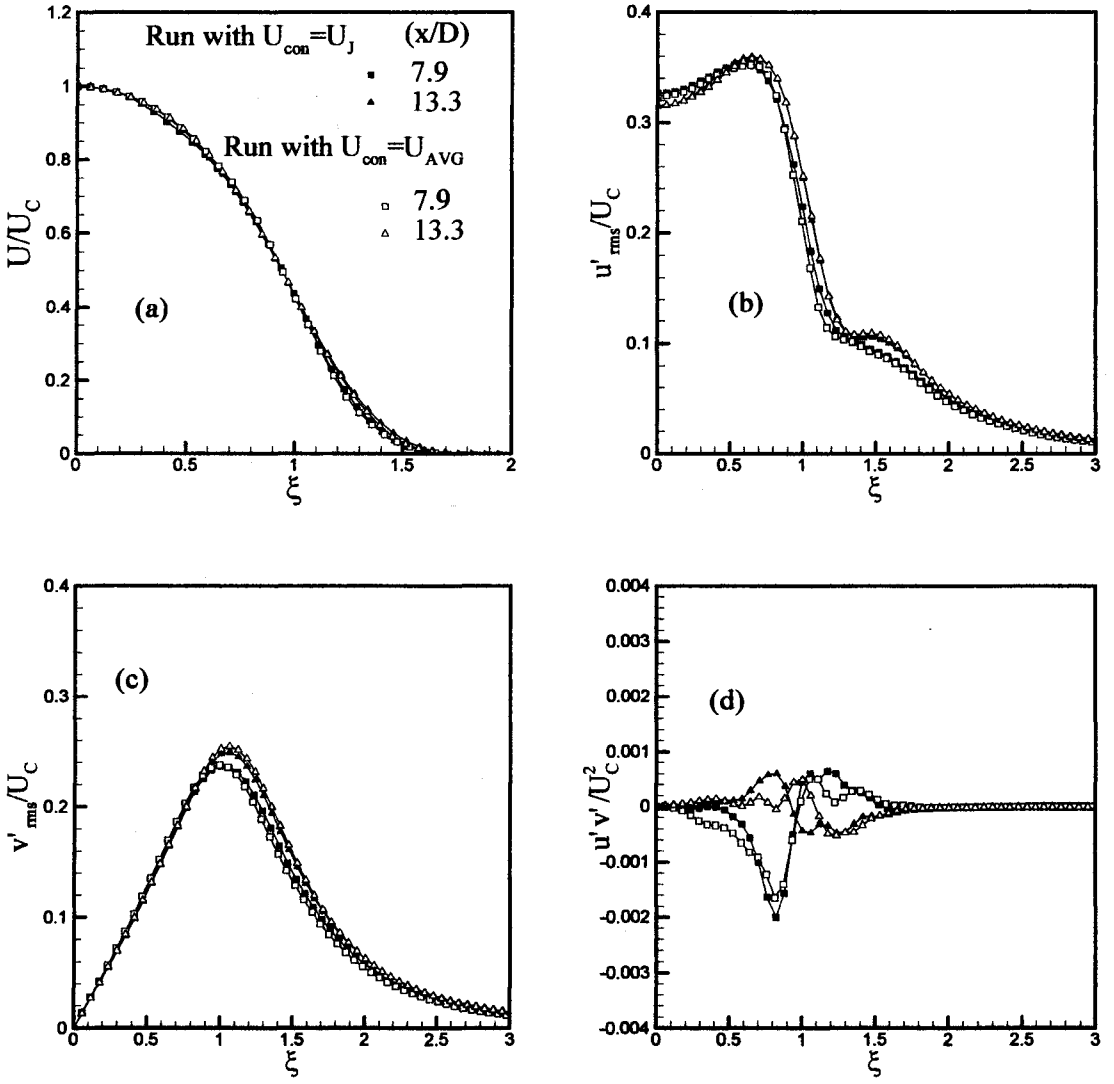

Figure 14. Comparison of one sheet $U_{con}=U_J$ with one sheet $U_{con}=U_{AVG}$ at two downstream locations: (a) streamwise mean velocity, (b) rms longitudinal velocity fluctuations, (c) rms lateral velocity fluctuations, (d) cross-stream correlation.

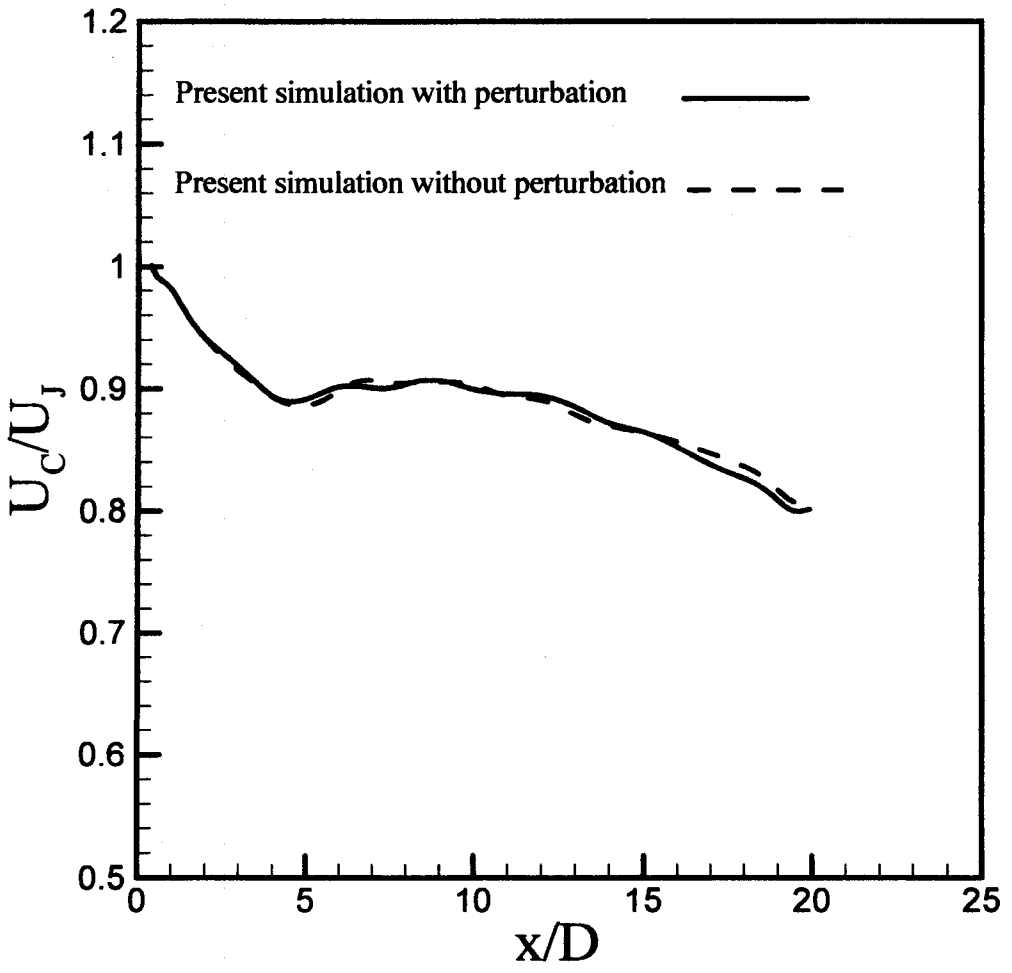

Figure 15. Streamwise mean centerline decay using perturbation with Nr=0.25 compared with streamwise mean centerline decay without perturbation.

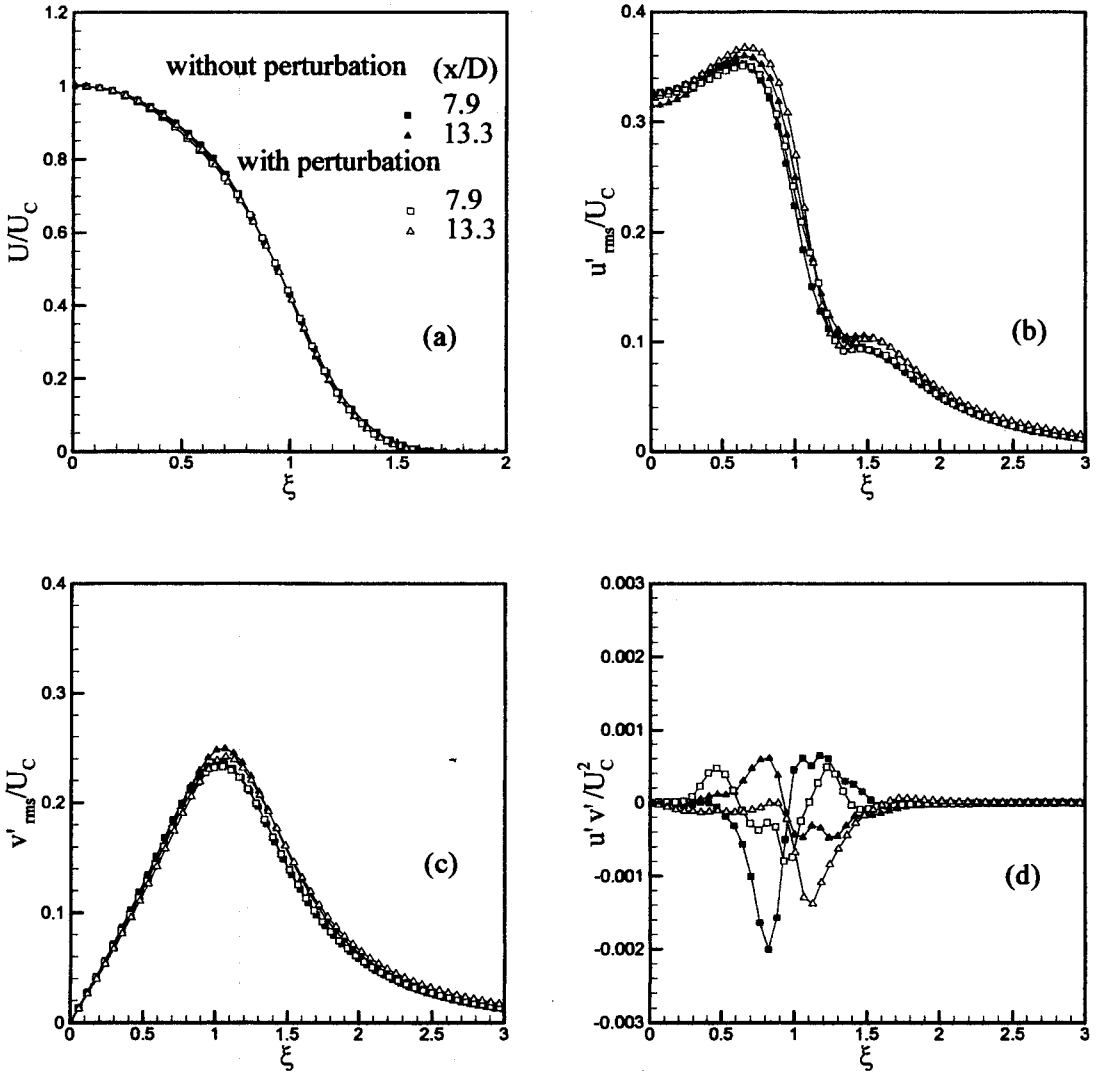

Figure 16. Comparison of case without perturbation with case using perturbation with Nr=0.25 at two downstream locations: (a) streamwise mean velocity, (b) rms longitudinal velocity fluctuations, (c) rms lateral velocity fluctuations, (d) cross-stream correlation.

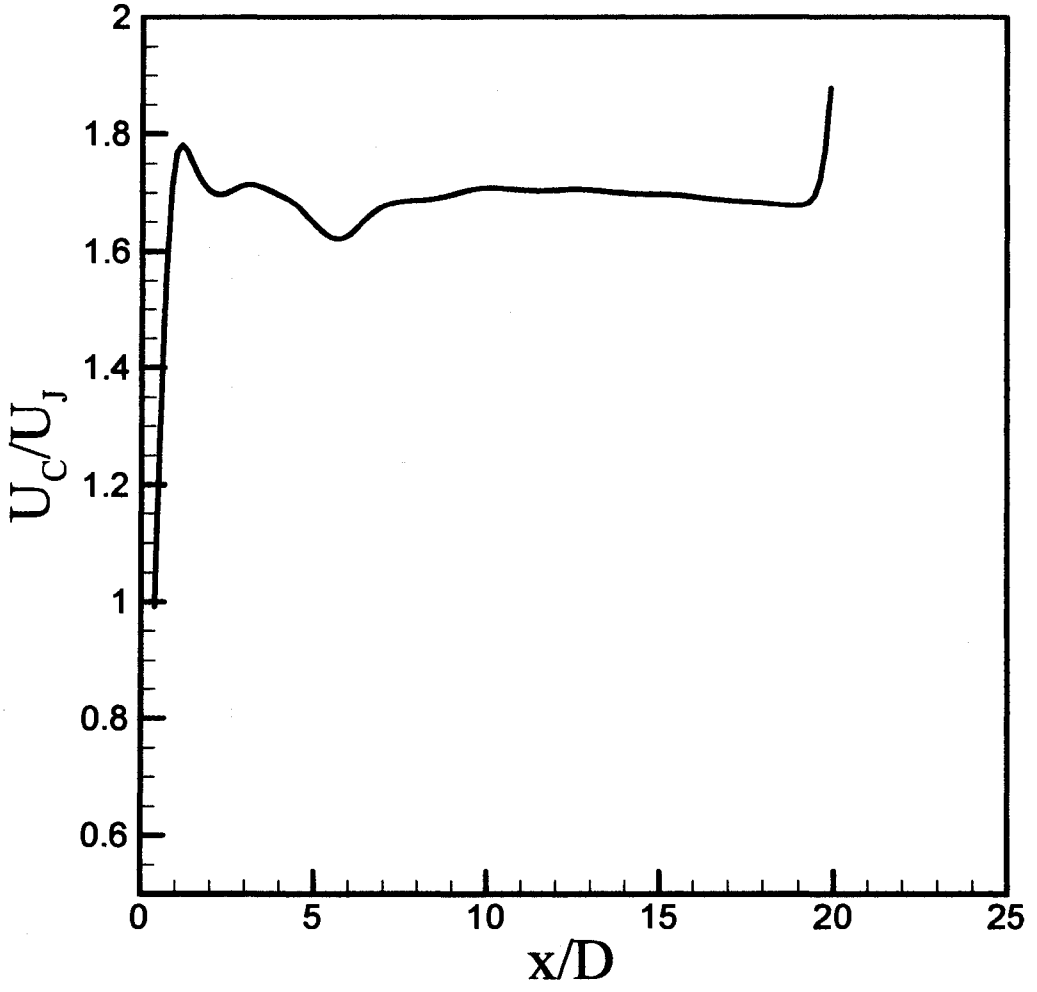

Figure 17. Streamwise mean centerline velocity using self similar inflow boundary condition

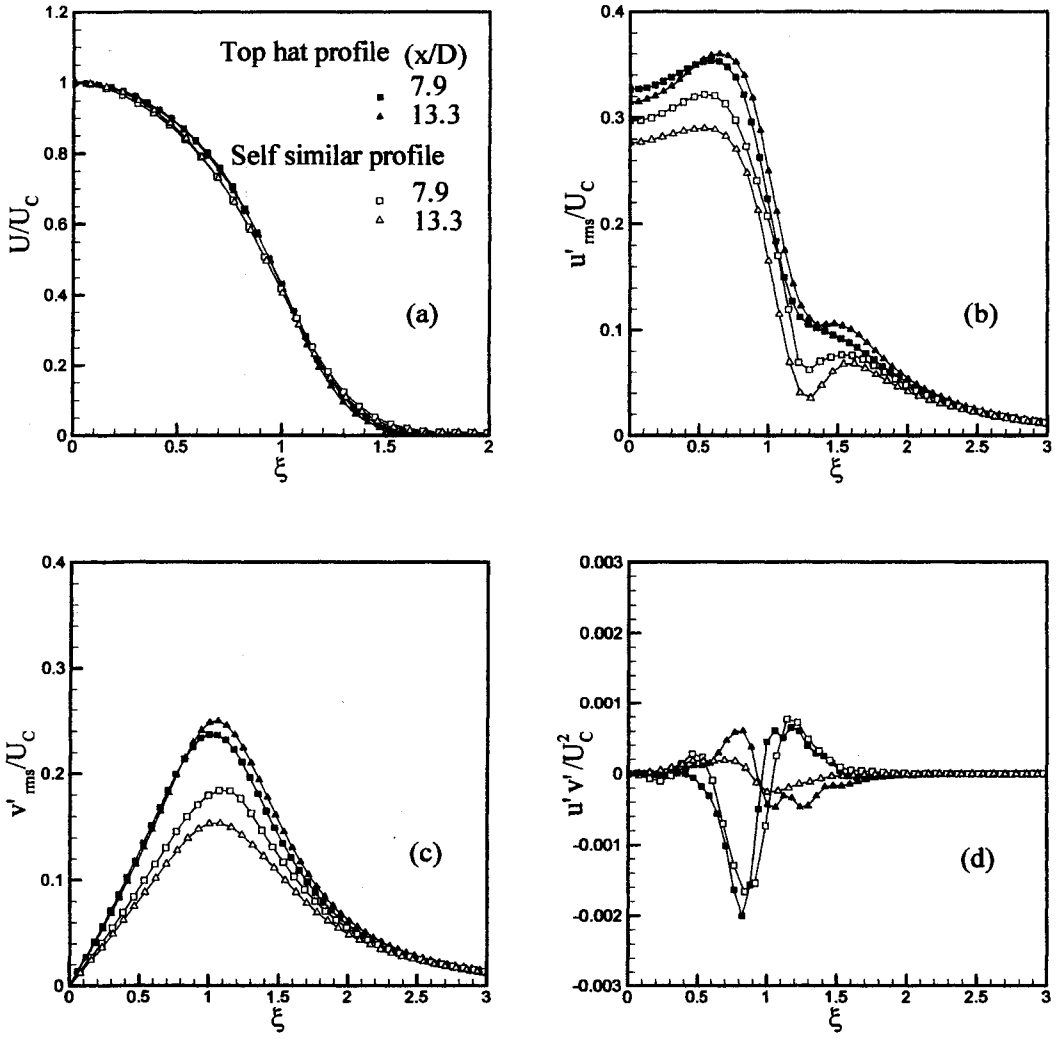

Figure 18. Effect of inflow boundary conditions on flow field, top hat inflow profile versus self similar profile at two downstream locations: (a) streamwise mean velocity, (b) rms longitudinal velocity fluctuation, (c) rms lateral velocity fluctuation, (d) cross-stream correlation. Dark symbols, top hat; Open symbols, self similar profile.

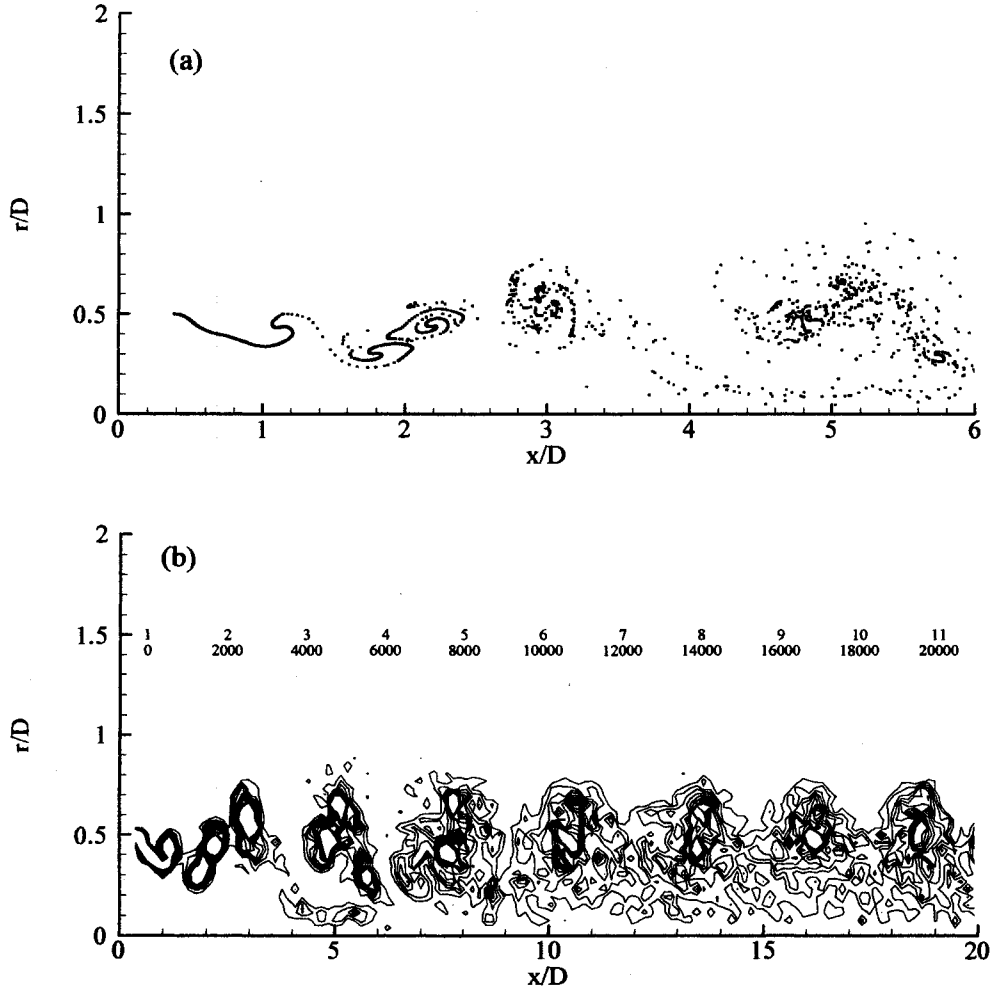

Figure 19. Effect of self similar profile inflow boundary condition on : (a) instantaneous distribution of vortex elements, (b) vorticity contour, contour level increment is 2000.

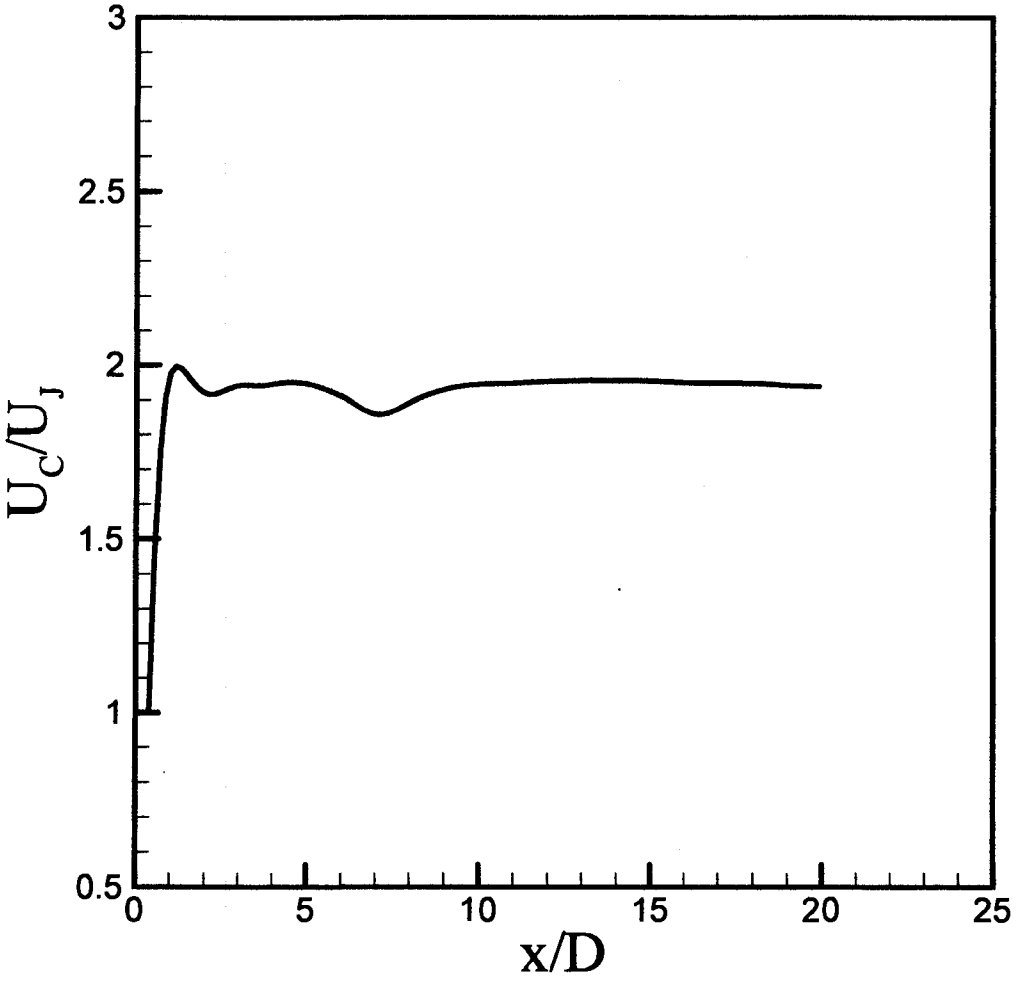

Figure 20. Streamwise mean centerline velocity using Stokes stream function with one vortex sheet.

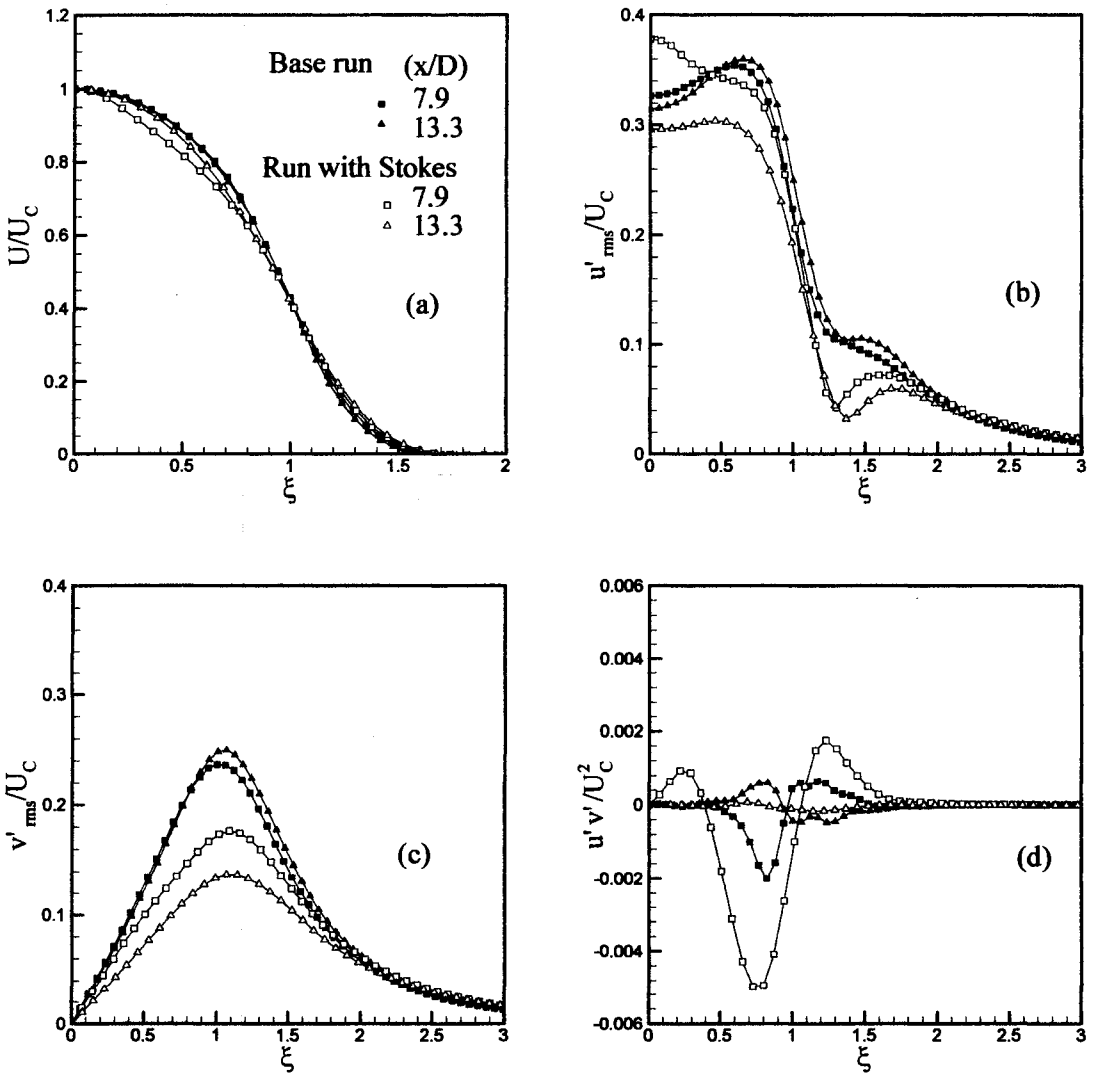

Figure 21. Comparison one sheet (base run) with one sheet using Stokes stream function at two downstream locations: (a) streamwise mean velocity, (b) rms longitudinal velocity fluctuations, (c) rms lateral velocity fluctuations, (d) cross-stream correlation.

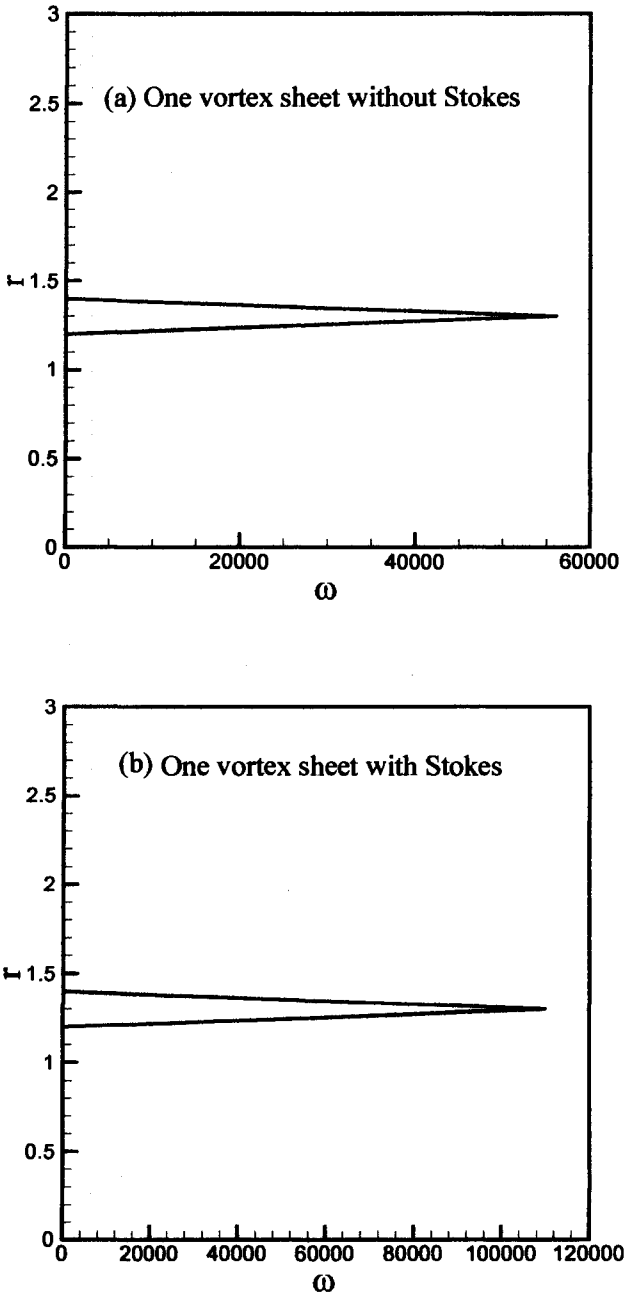

Figure 22. Vorticity field distribution in the radial direction for cases: (a) one vortex sheet without Stokes, (b) one vortex sheet with Stokes.

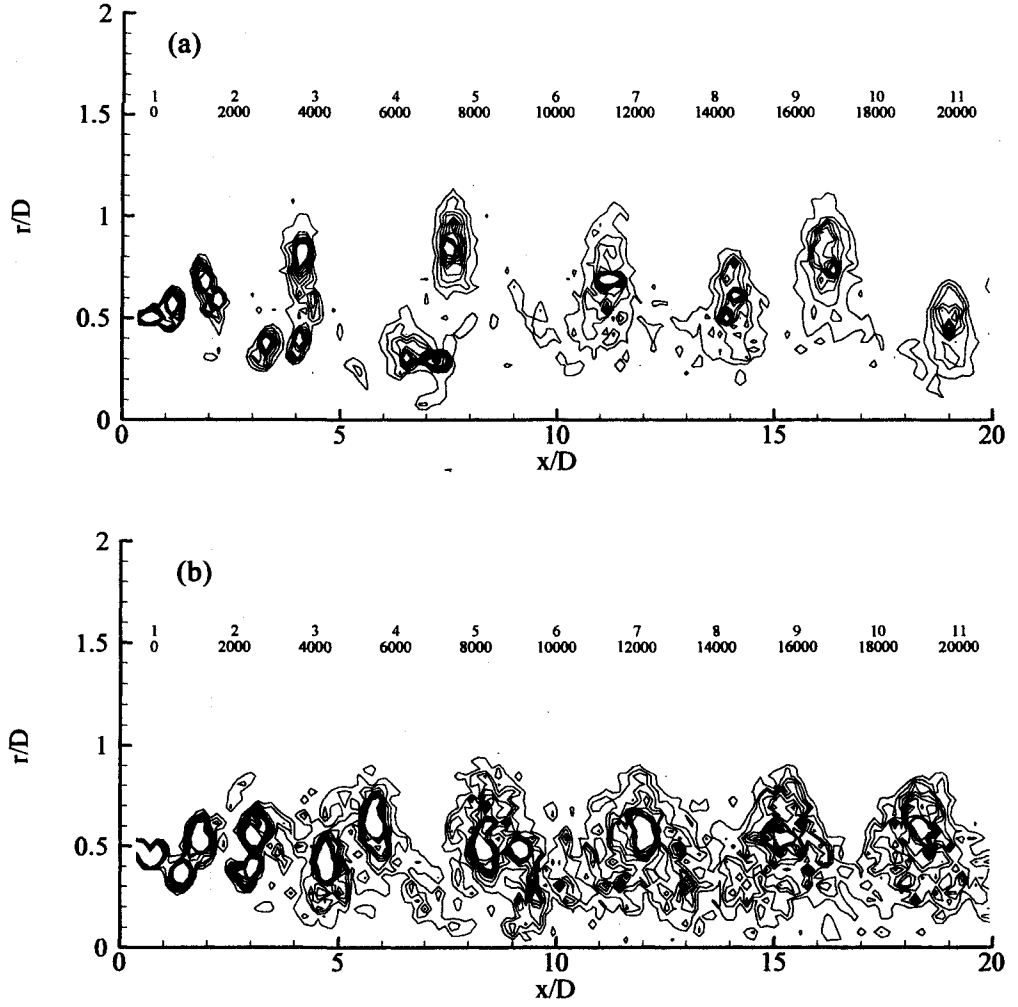

Figure 23. Comparison of vorticity contours for one sheet: (a) base run, (b) using Stokes stream function, contour level increment is 2000.

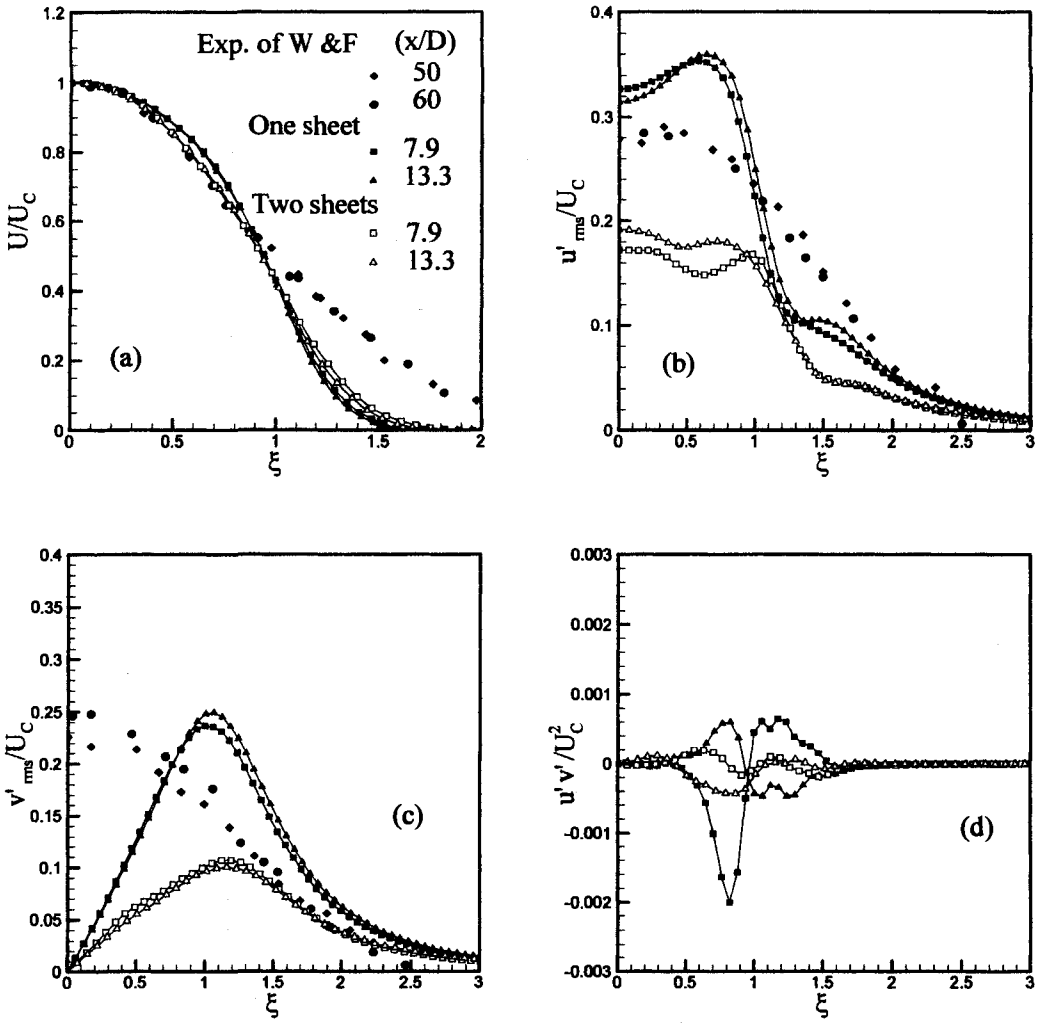

Figure 24. Comparison one sheet and two sheets with Exp. of W & F at two downstream locations: (a) streamwise mean velocity, (b) rms longitudinal velocity fluctuations, (c) rms lateral velocity fluctuations, (d) cross-stream correlation. Dark diamond and circle symbols, Exp. of Wygnanski & Fiedler (1969); mesh lines connecting dark symbols, one sheet; mesh lines connecting open symbols, two sheets.

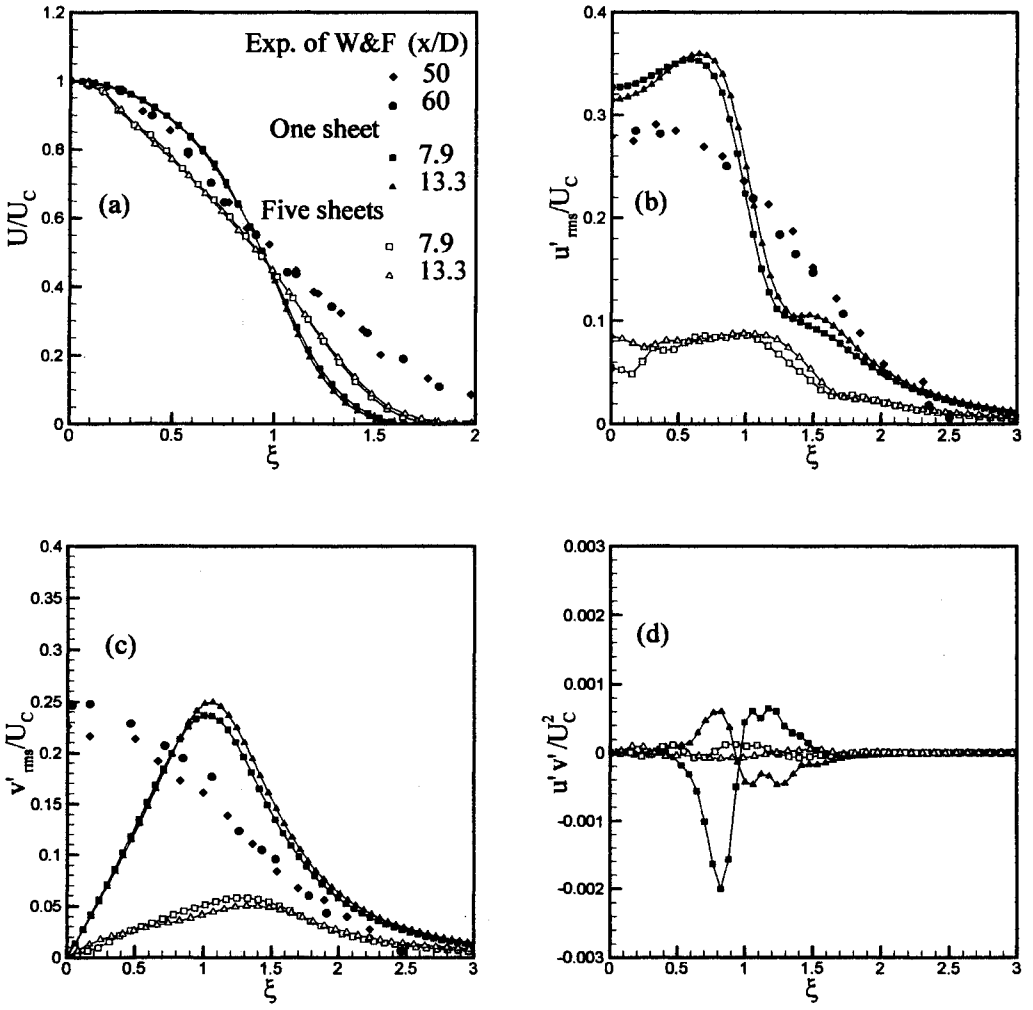

Figure 25. Comparison one sheet and five sheets with Exp. of W & F at two downstream locations: (a) streamwise mean velocity, (b) rms longitudinal velocity fluctuations, (c) rms lateral velocity fluctuations, (d) cross-stream correlation. Dark diamond and circle symbols, Exp. of Wygnanski & Fiedler (1969); mesh lines connecting dark symbols, one sheet; mesh lines connecting open symbols, five sheets.

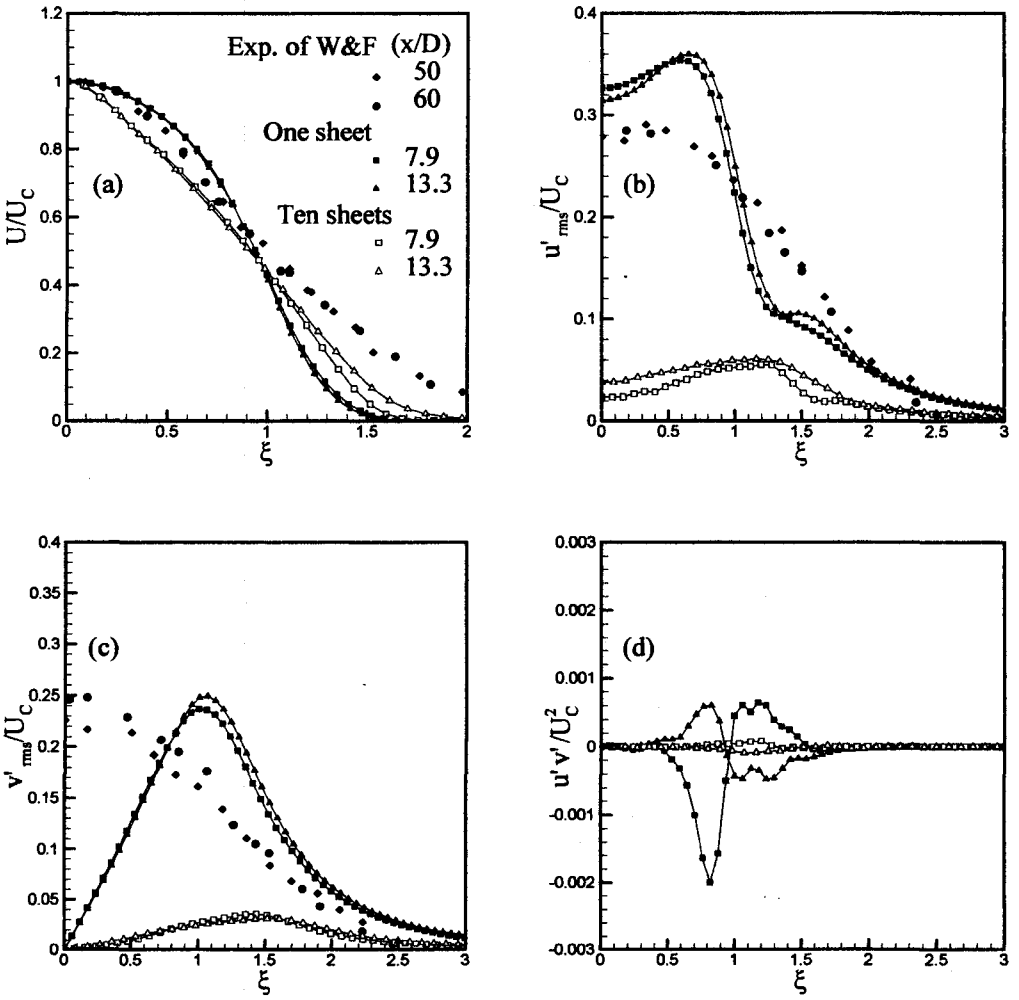

Figure 26. Comparison one sheet and ten sheets with Exp. of W & F at two downstream locations: (a) streamwise mean velocity, (b) rms longitudinal velocity fluctuations, (c) rms lateral velocity fluctuations, (d) cross-stream correlation. Dark diamond and circle symbols, Exp. of Wygnanski & Fiedler (1969); mesh lines connecting dark symbols, one sheet; mesh lines connecting open symbols, ten sheets.

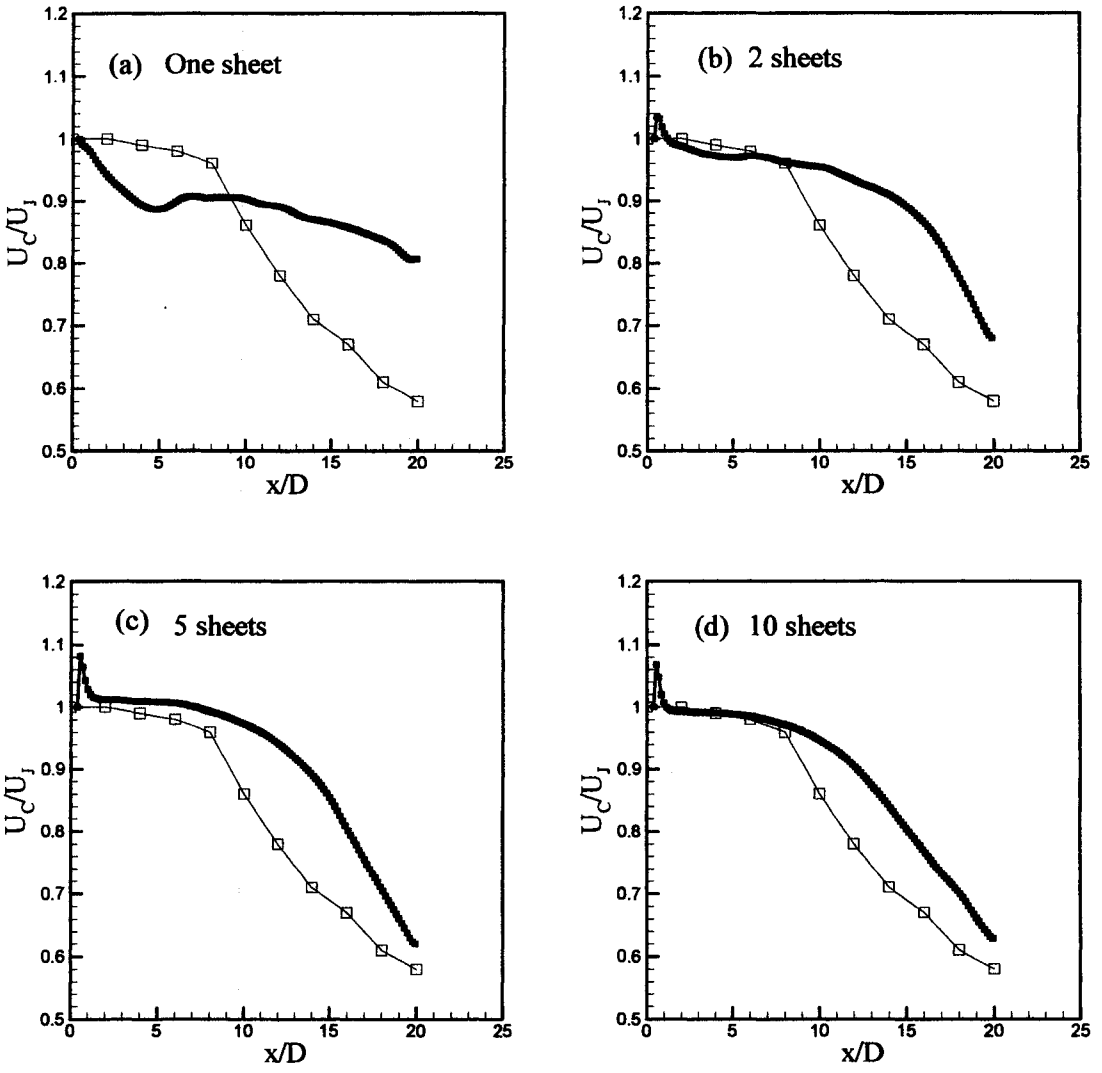

Figure 27. Effect of initializing on the streamwise mean centerline decay using: (a) one sheet, (b) two sheets, (c) five sheets, and (d) ten sheets. Dark square symbols, present simulation; open square symbols, 2D simulation of Sidahmed & Brown (2001).

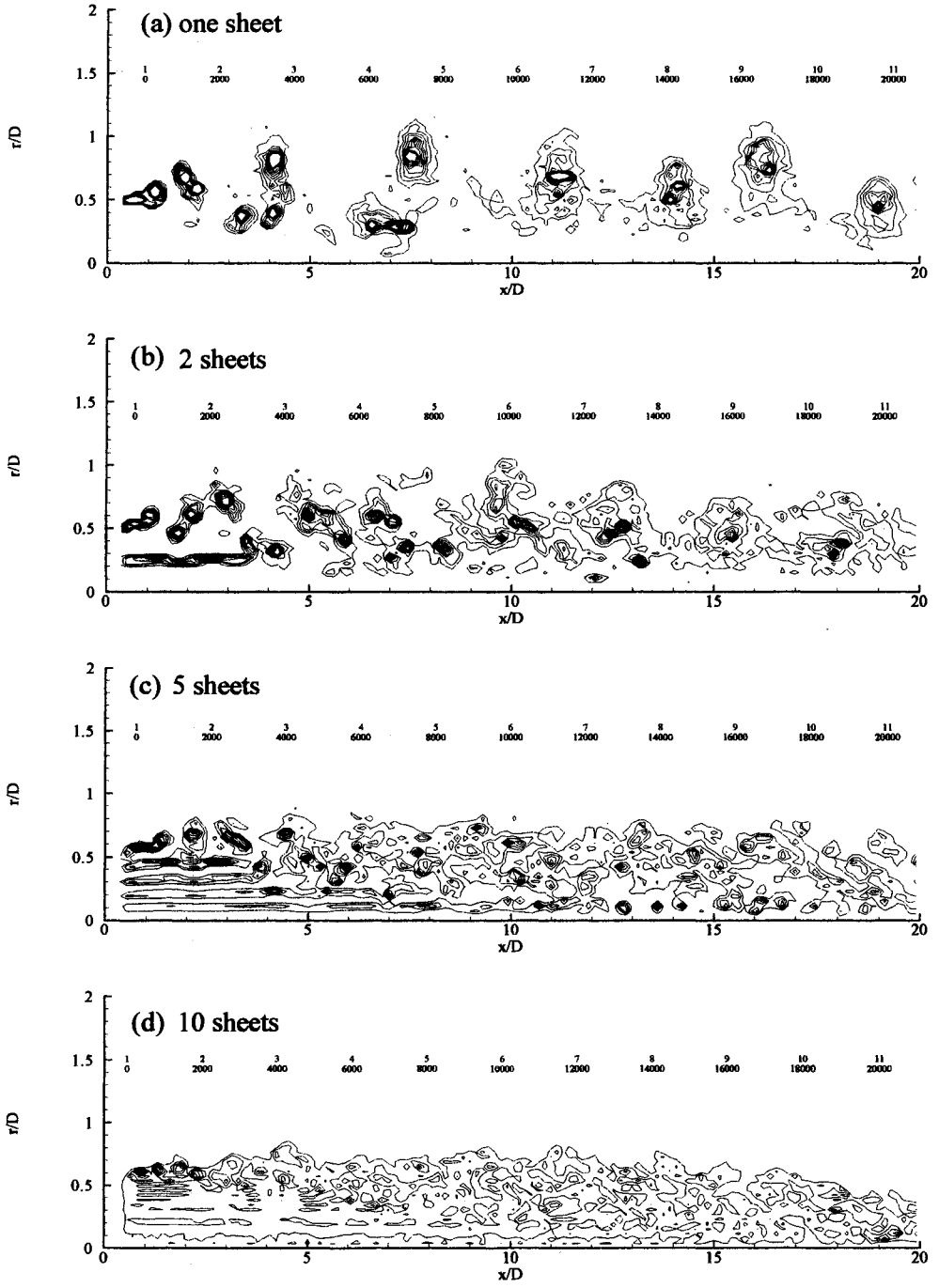

Figure 28. Comparison of vorticity contours for cases: (a) one sheet, (b) two sheets, (c) five sheets, (d) ten sheets, contour level increment is 2000.

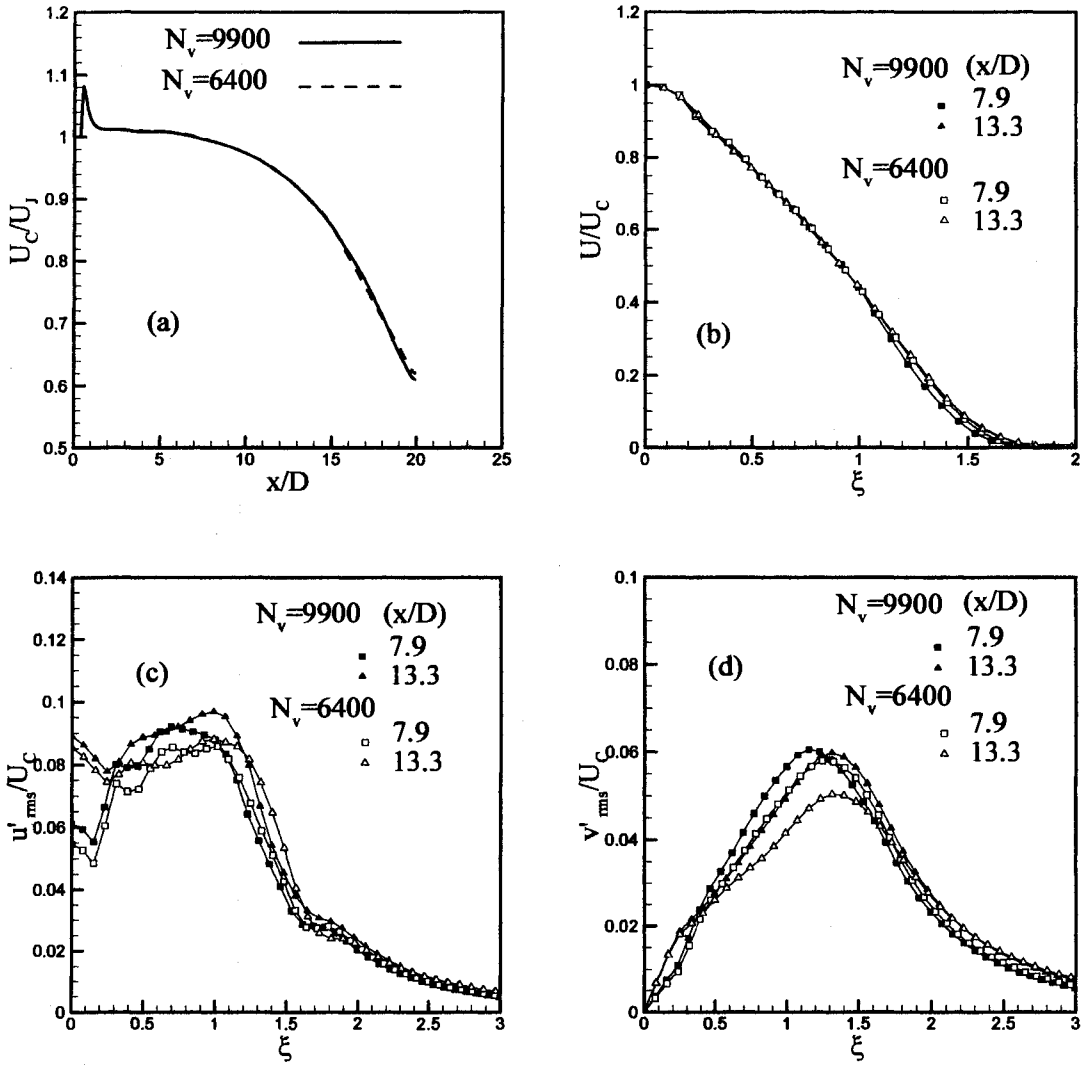

Figure 29. Sensitivity of number of vortex elements N_v=9900 and 6400 vortices using five sheets to: (a) the streamwise mean centerline velocity, (b) the streamwise mean velocity at two downstream locations, (c) rms longitudinal fluctuations at two downstream locations, and (d) rms lateral fluctuations at two downstream locations.

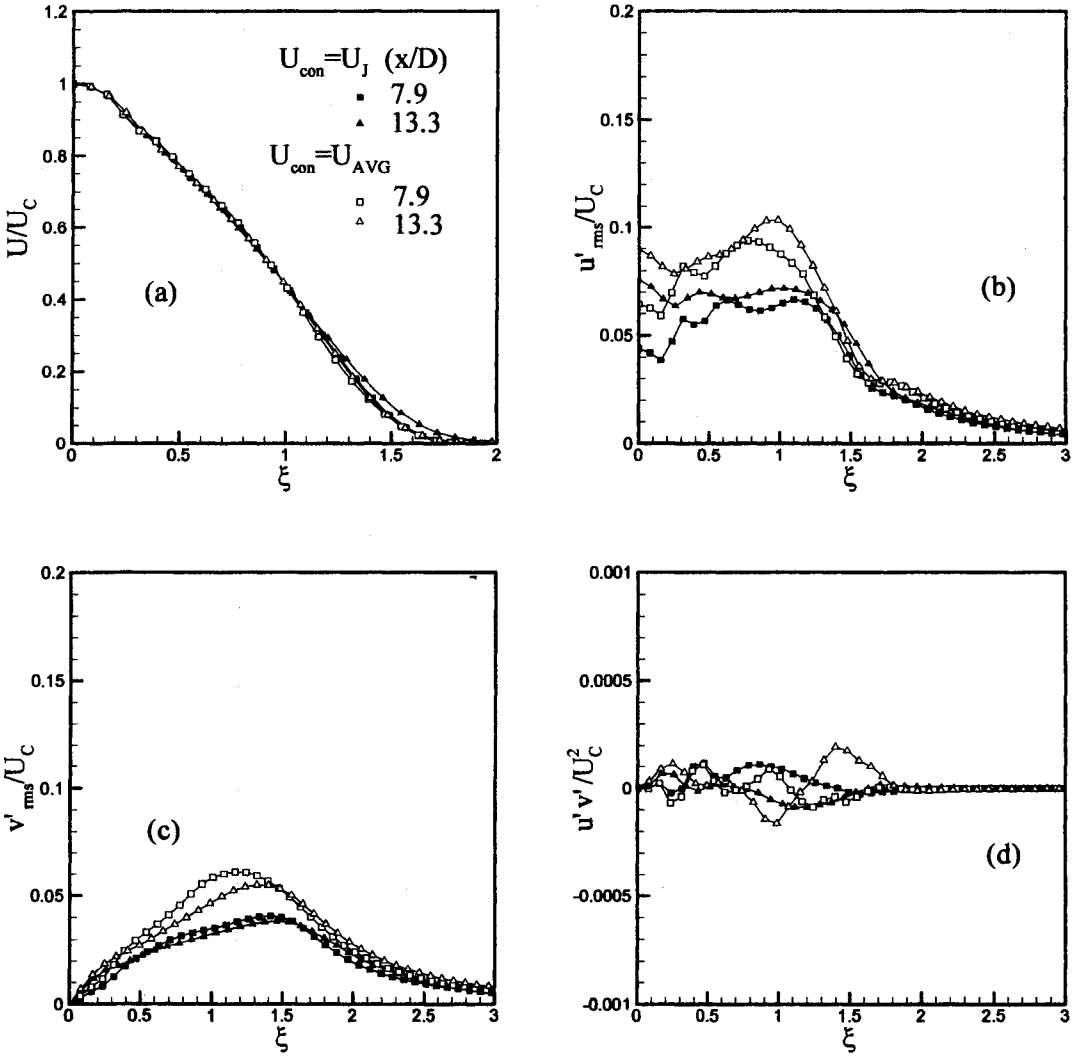

Figure 30. Comparison of $U_{con}=U_J$ with $U_{con}=U_{AVG}$ using five sheets at two downstream locations: (a) streamwise mean velocity, (b) rms longitudinal velocity fluctuations, (c) rms lateral velocity fluctuations, (d) cross-stream correlation.

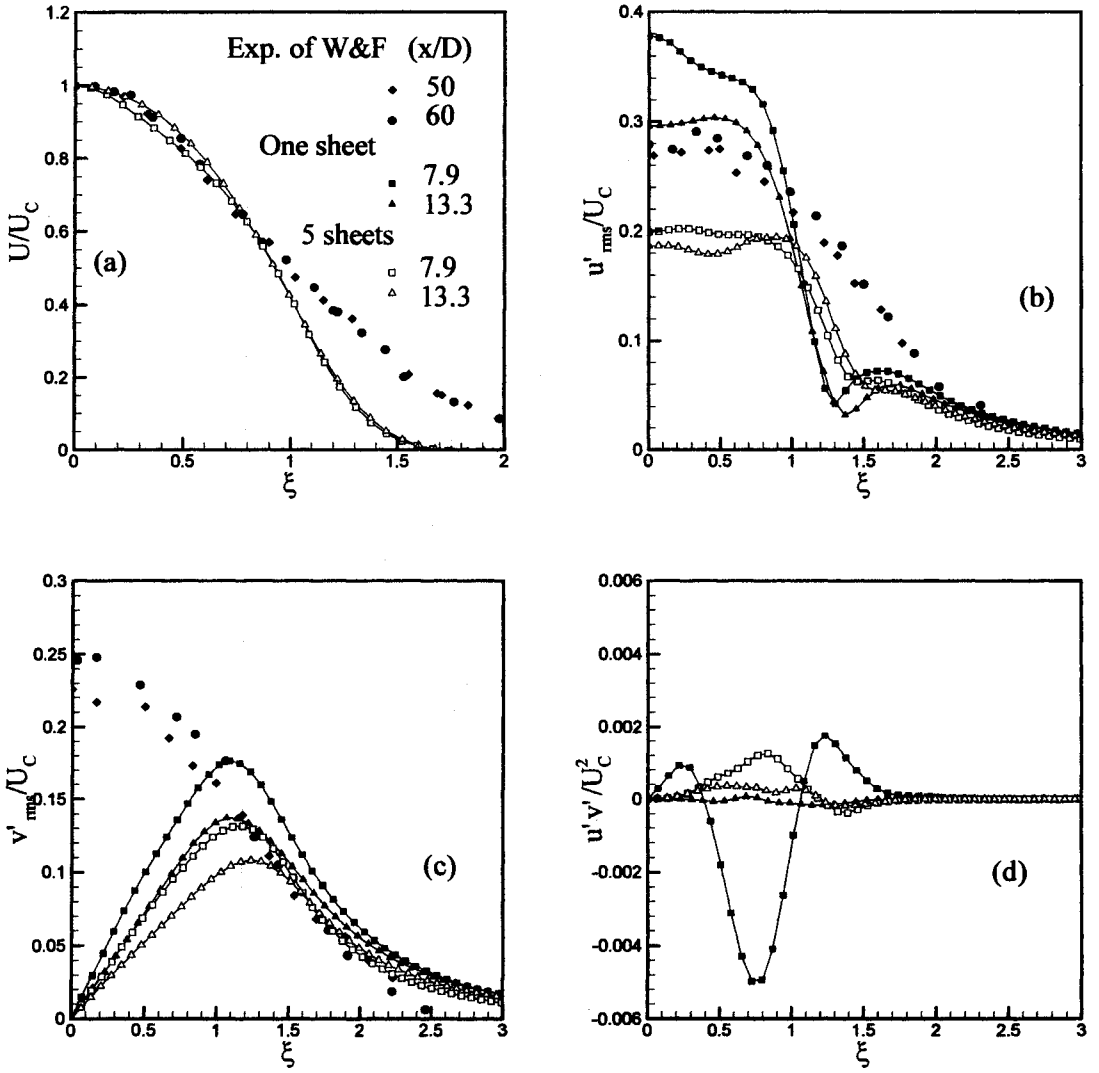

Figure 31. Comparison one sheet and five sheets using Stokes with Exp. of W&F at two downstream locations: (a) streamwise mean velocity, (b) rms longitudinal velocity fluctuations, (c) rms lateral velocity fluctuations, (d) cross-stream correlation. Dark diamond and circle symbols, Exp. of Wygnanski & Fiedler (1969); mesh lines connecting dark symbols, one sheet; mesh lines connecting open symbols, five sheets.

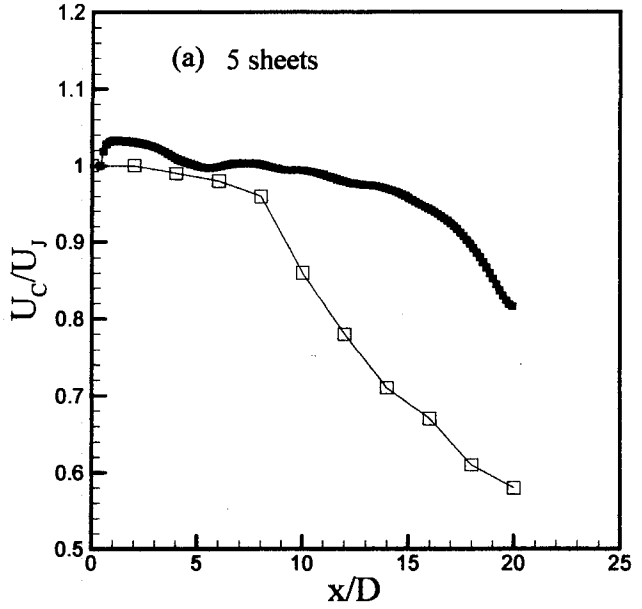

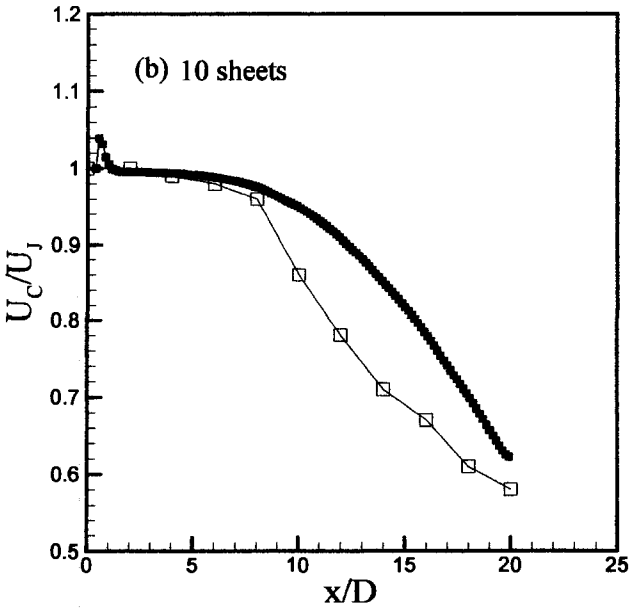

Figure 33. Effect of initializing using Stokes on the streamwise mean centerline decay using: (a) five sheets, (b) ten sheets. Dark square symbols, present simulation; open square symbols, 2D simulation of Sidahmed & Brown (2001).

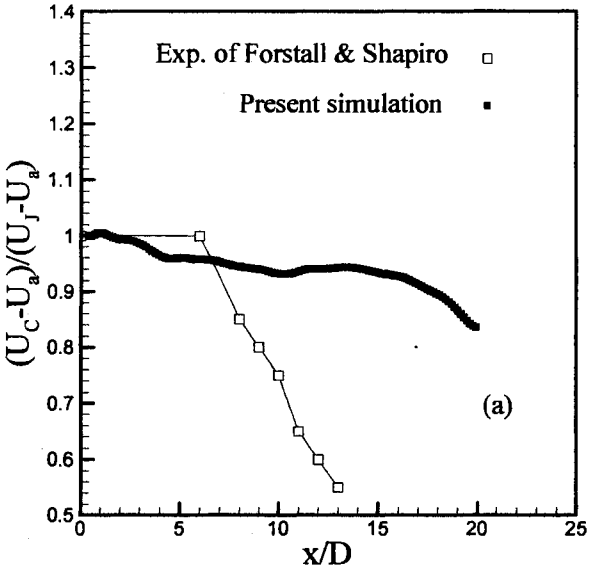

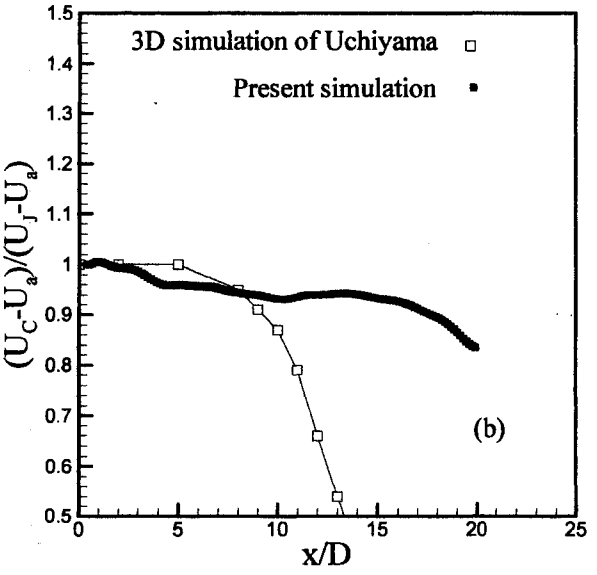

Figure 34. Streamwise mean centerline velocity: (a) comparison with experiment of Forstall & Shapiro (1950), (b) comparison with 3D simulation of Uchiyama (2003).

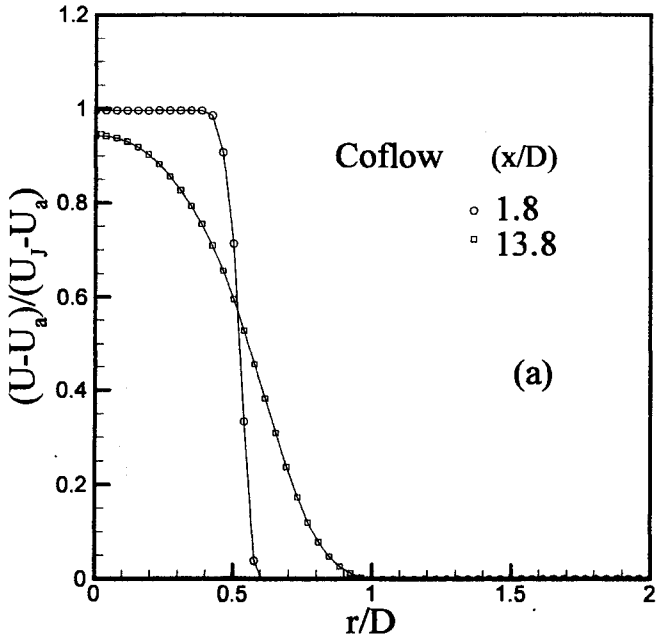

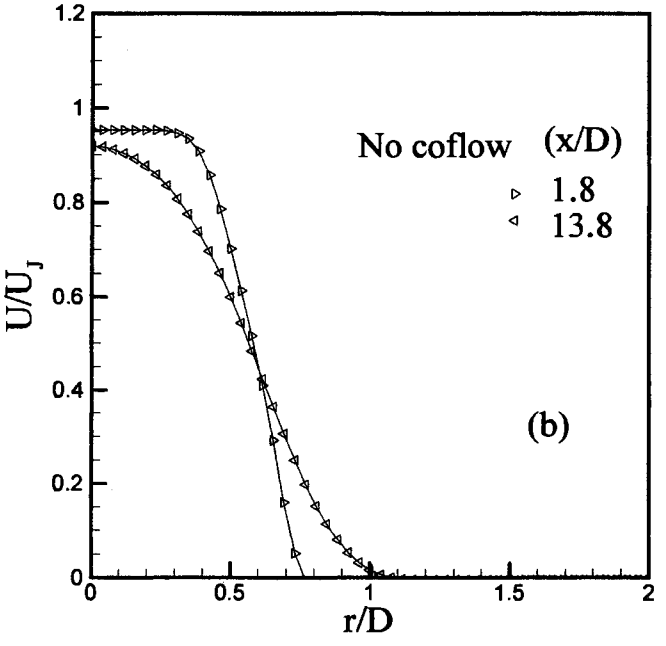

Figure 35. Radial profiles of the streamwise mean velocity at two downstream locations showing the spreading of, (a) coflow jet, and (b) no coflow jet.

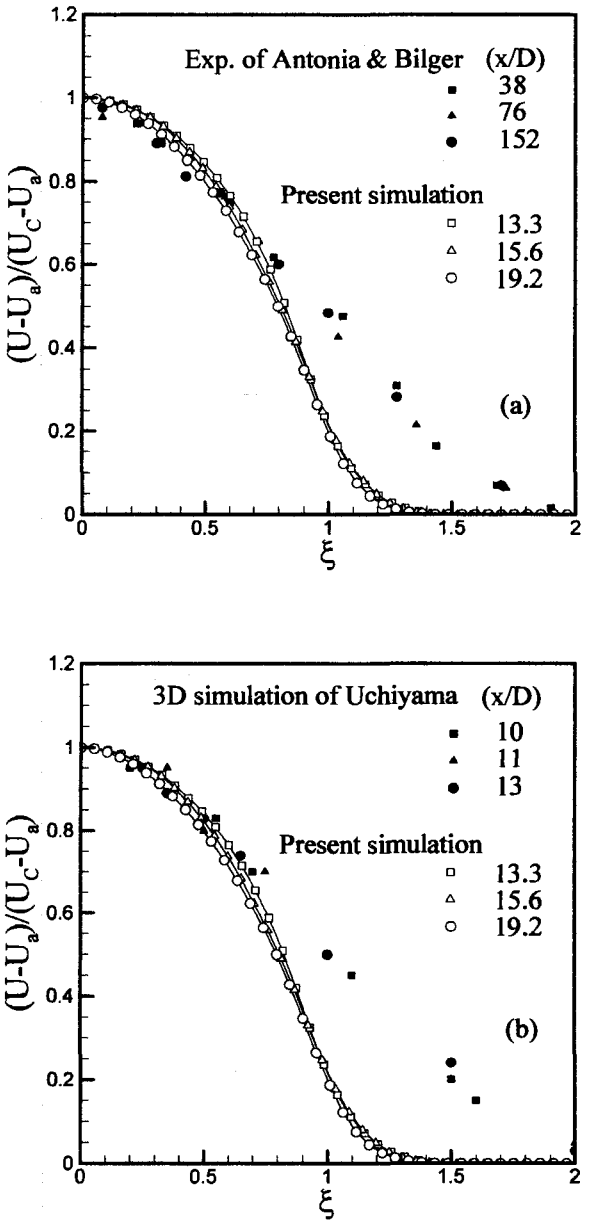

Figure 36. Streamwise mean velocity normalized with the difference of streamwise mean centerline velocity and the coflowing velocity at three downstream locations: (a) present simulation compared with the experiment of Antonia & Bilger (1973), (b) present simulation compared with the 3D simulation of Uchiyama (2003) .

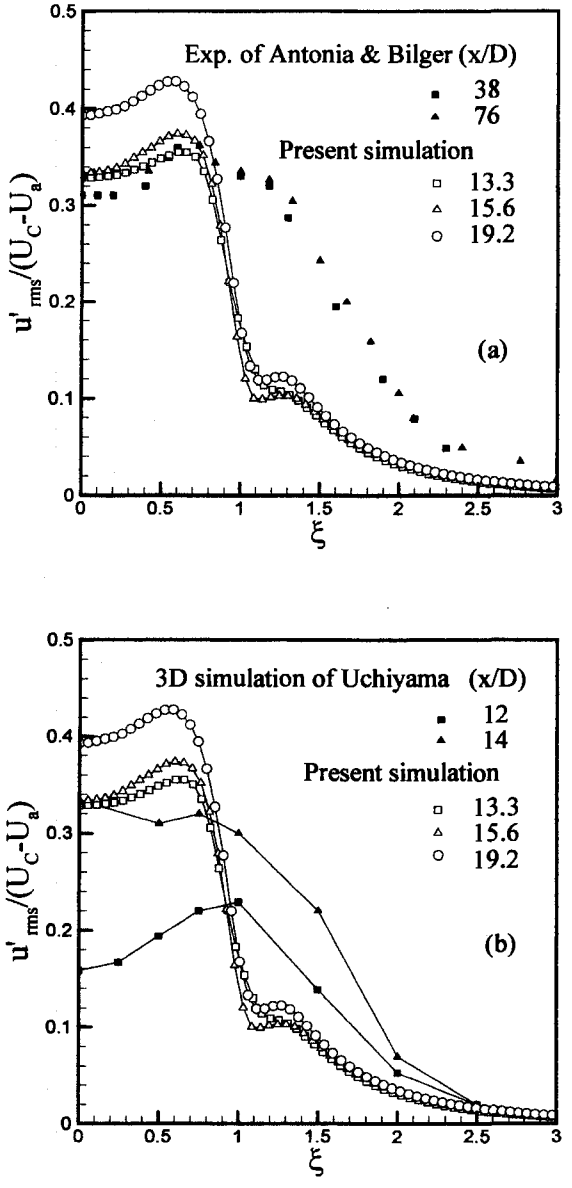

Figure 37. longitudinal root mean square fluctuations normalized with the difference of streamwise mean centerline velocity and the coflowing velocity at three downstream locations: (a) present simulation compared with the experiment of Antonia & Bilger (1973), (b) present simulation compared with the 3D simulation of Uchiyama (2003).

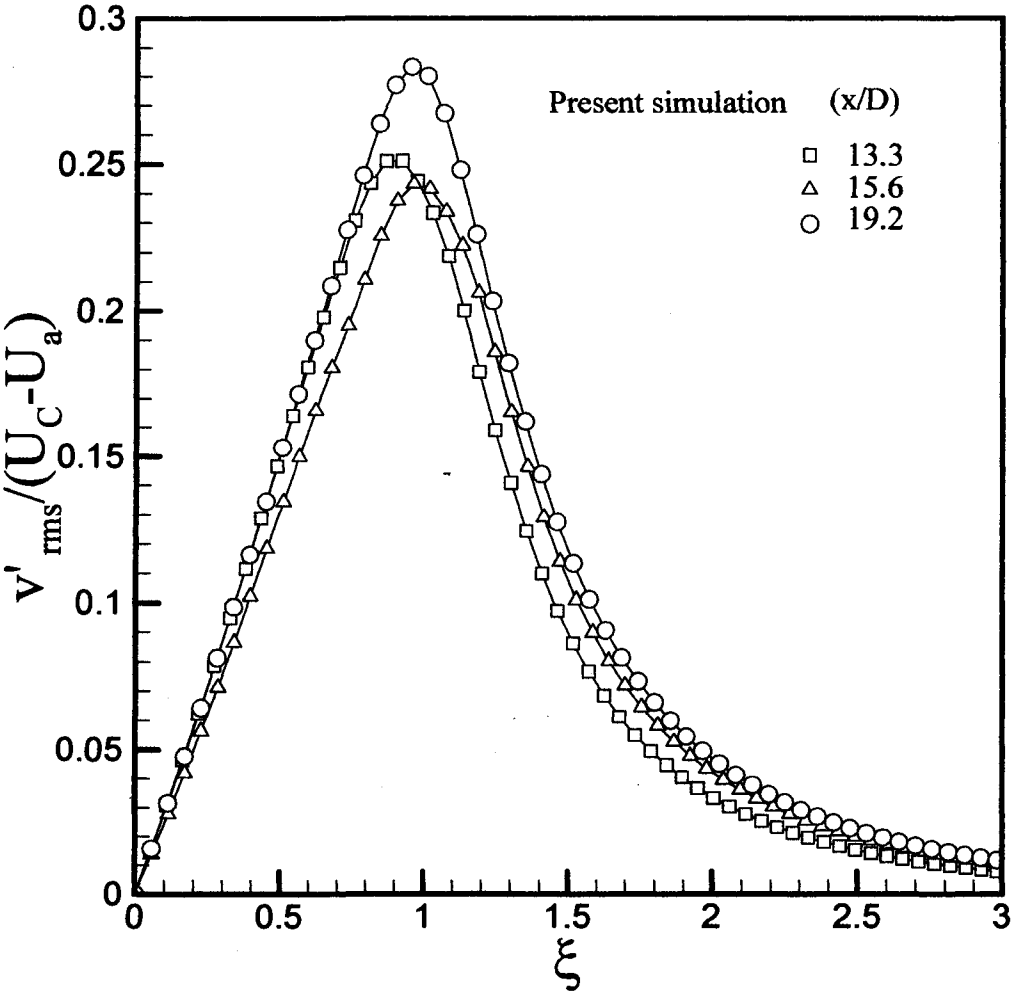

Figure 38. Lateral root mean square fluctuations normalized with the difference of streamwise mean centerline velocity and the coflowing velocity at three downstream locations.

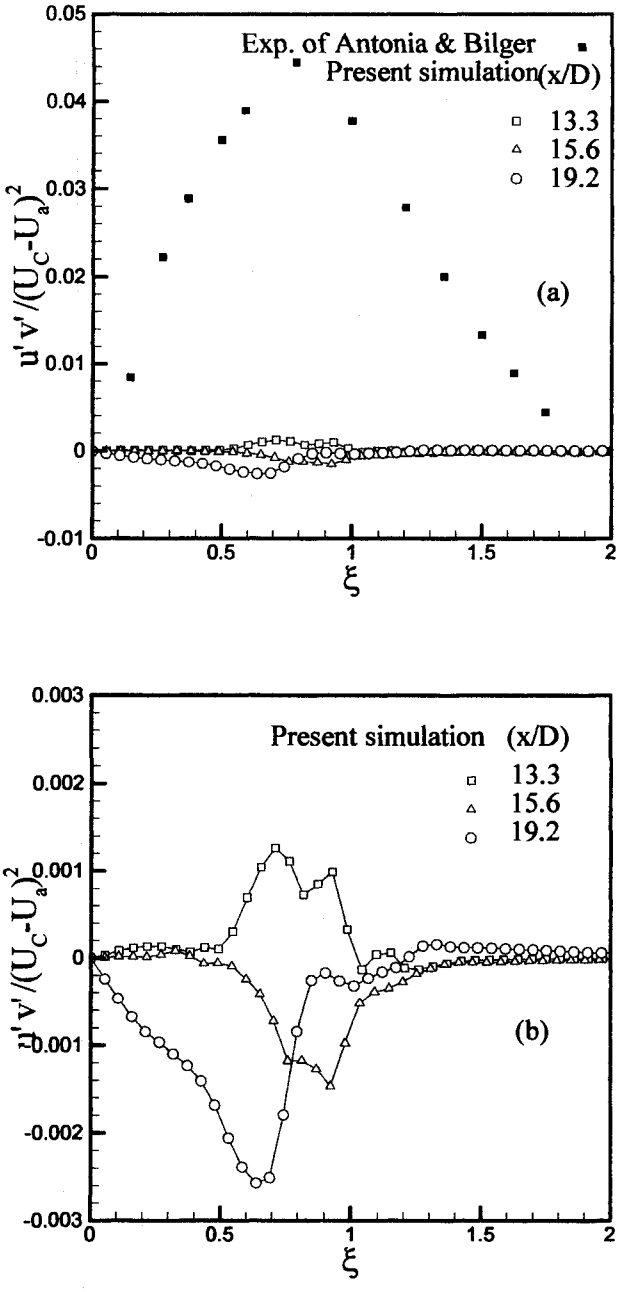

Figure 39. Cross-stream correlation normalized with the square of the difference of streamwise mean centerline velocity and the coflowing velocity at three downstream locations: (a) comparison with the experiment of Antonia & Bilger (1973), (b) magnification of the simulated cross-stream correlation. The mesh lines connecting the open symbols show the present predicted profiles; the dark symbols correspond to the data from the experiment of Antonia & Bilger (1973).

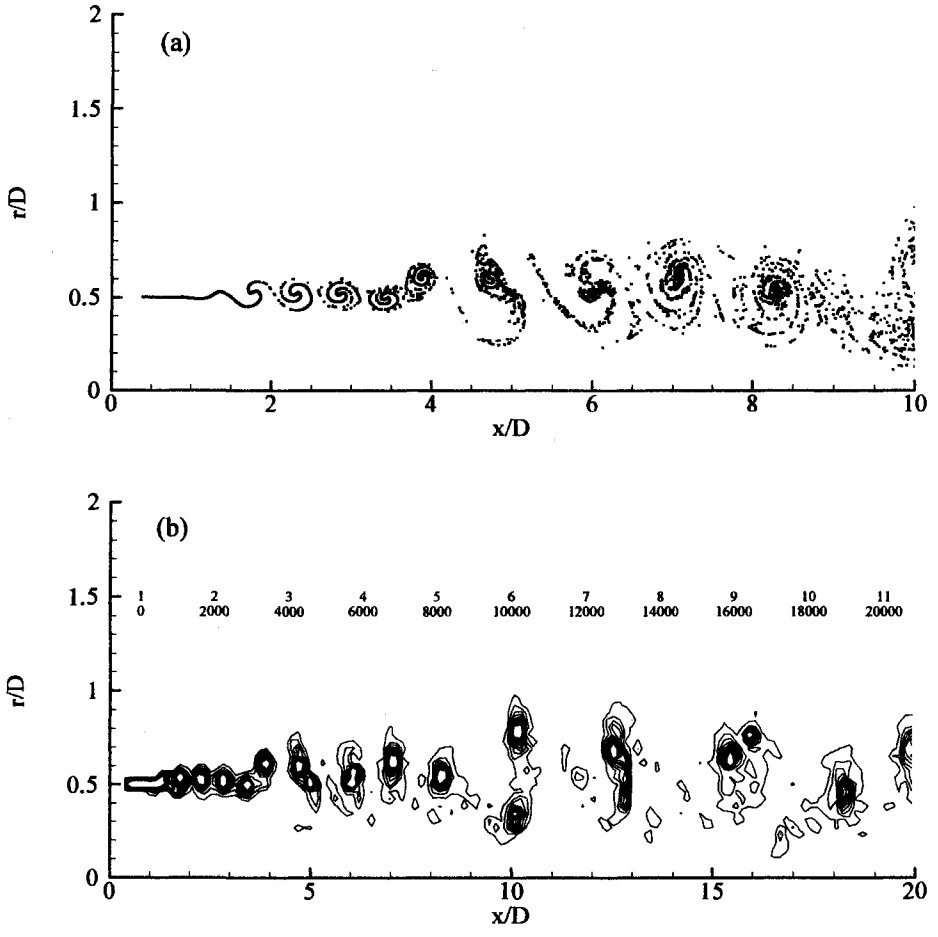

Figure 40. (a) Instantaneous distribution of vortex elements, (b) Vorticity contour for coflow jet, contour level increment is 2000.

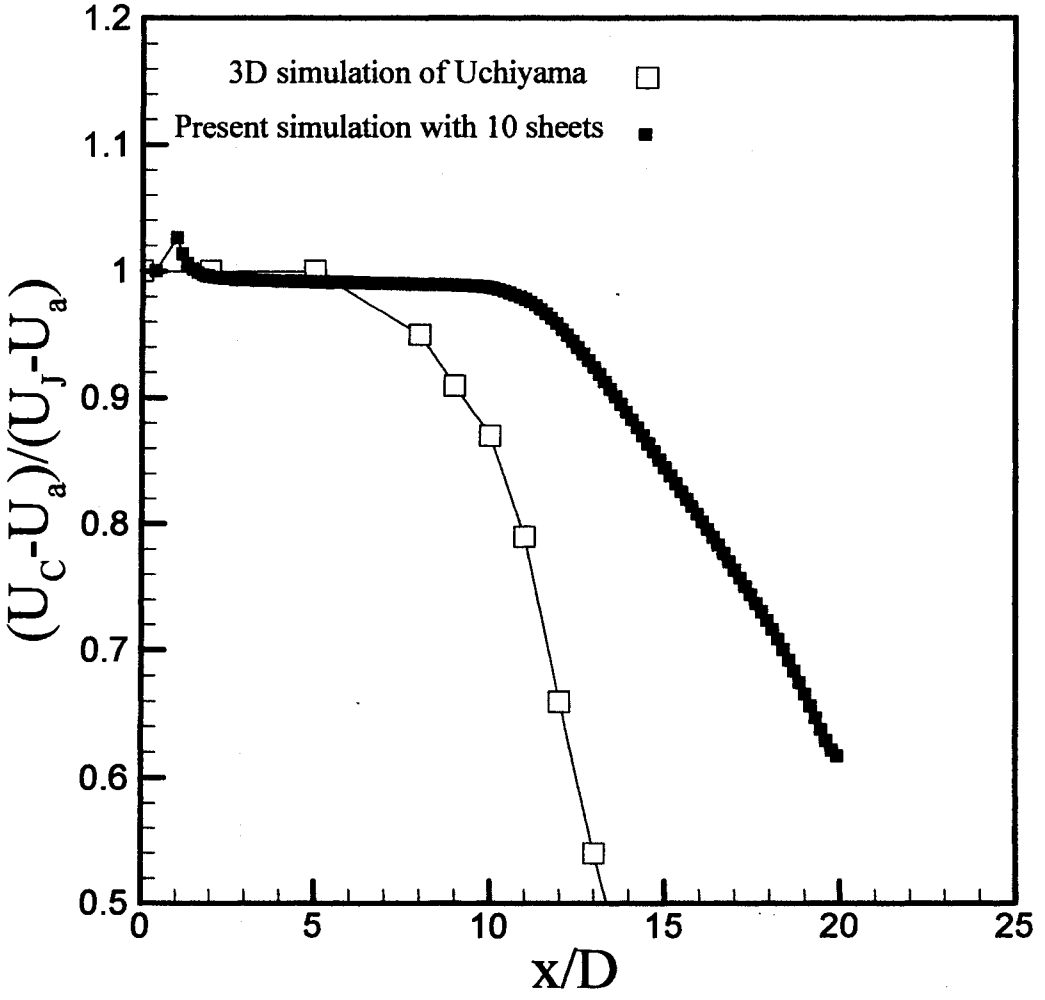

Figure 41. Streamwise mean centerline velocity decay using ten sheets of vortex elements compared with 3D simulation of Uchiyama (2003).

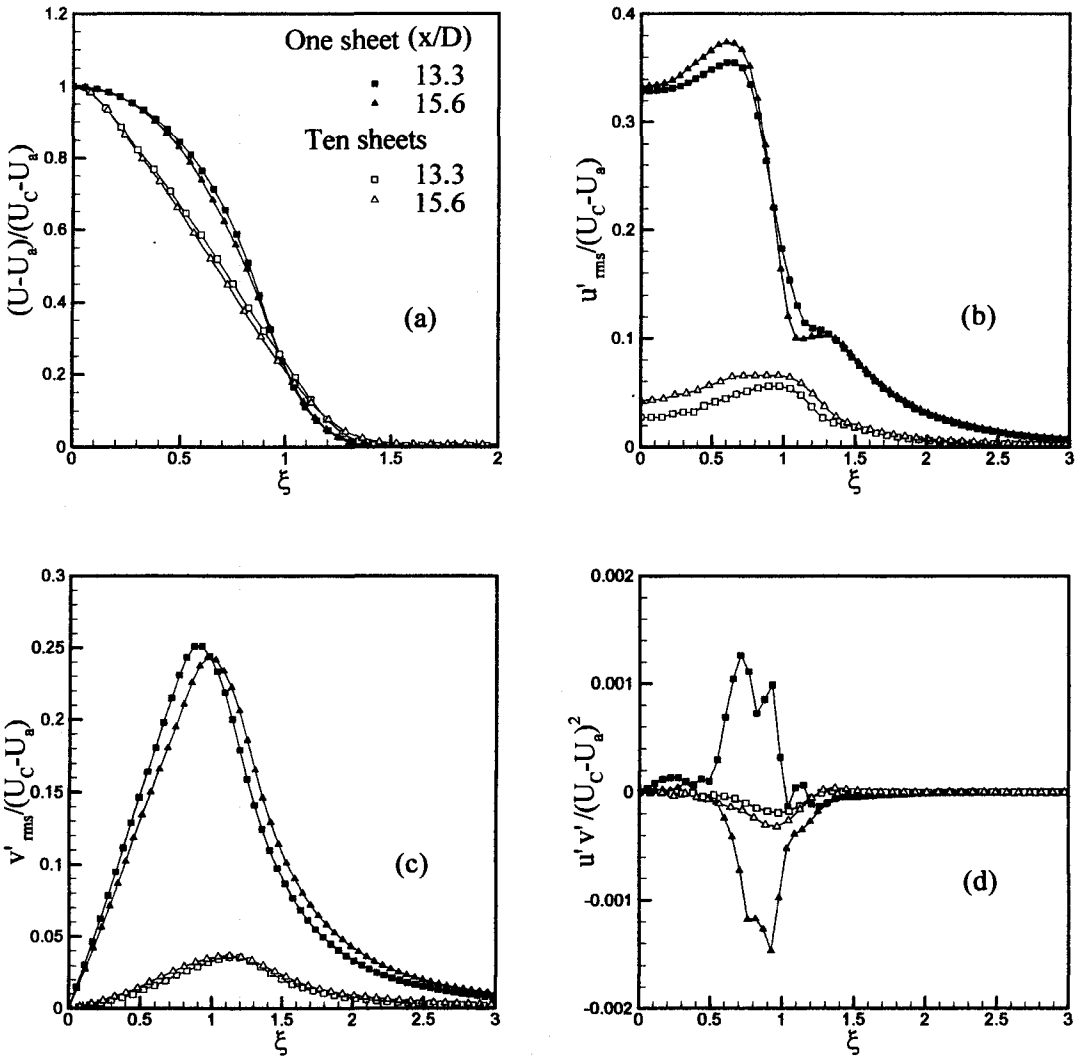

Figure 42. Comparison one sheet with ten sheets at two downstream locations: (a) streamwise mean velocity, (b) rms longitudinal velocity fluctuations, (c) rms lateral velocity fluctuations, (d) cross-stream correlation. Open symbols, ten sheets; dark symbols, one sheet.

References

Abdolhosseini R. and Milane RE. On the effect of Vortex Grid Density in the Vortex-in-Cell Simulation of Mixing Layer. International Journal of Fluid Dynamics 2000, vol. 13, pp. 161-183.

Abernathy, F. H. and Kronauer R. E. The Formation of Vortex Sheets, J. Fluid Mech. 1962, vol.13, pp. 1-20.

Abid M. and Brachet M. Numerical Characterization of The Dynamics of Vortex Filaments in Round Jets, Phys. Fluids. 1993, A5-11, 2582.

Abramowitz M. and Stegun I. A. Handbook of Mathematical Functions, Dover Publication, New York, 1972.

Acton E. The Modelling of Large Eddies in a Two Dimensional Shear Layer, J. Fluid Mech. 1976, vol. 76, pp. 561-592.

Acton E. A Modelling of Large Eddies in an Axisymmetric Jet, J. Fluid Mech. 1980, vol. 98, pp. 1-31.

Antonia R. A. and Bilger R. W. An Experimental Investigation of an Axisymmetric Jet in a Co-flowing Air stream, J. Fluid Mech. 1973, vol. 61, pp. 805-822.

Aref H. and Siggia E. D. Vortex Dynamics of the Two Dimensional Turbulent Shear Layer, J. Fluid Mech.1980, vol. 100, pp.705-737.

Ashurst W. T. Numerical simulation of Turbulent Mixing Layer Via Vortex Dynamics, Turbulent Shear Flows I, (Ed.) Durst et al., Springer-Verlag, New York 1979, 402-413.

Batchelor G. K. An Introduction to Fluid Mechanics. Cambridge University Press 1970.

Baig A. M. and Milane RE. Vortex-In-Cell and Probability Density Function Approach for a Passive Scalar Field in a Mixing Layer, J. Computational Fluid Dynamic. 2004, vol.18 (3), pp. 247-263.

Baker G. R. The Cloud-in-Cell Technique Applied to the Roll-Up of the vortex Sheets, J. Comp. Phys.1979, vol.31, pp. 76-95.

Beaudoin A, Huberson S, Rivoalen E. Simulation of anisotropic diffusion by means of a diffusion velocity method, Journal of Computational Physics 2003; 186:122-135.

Boersma B. J., Brethouwer G., Nieuwstadt F. T. M. A Numerical Investigation on The Effect of the Inflow Conditions on The Self-Similar Region of a Round Jet. Physics of Fluids 1998, vol. 10, pp. 899-909.

Brown G. L. and Roshko, A. On Density Effects and Large Structure in Turbulent Mixing Layers, J. Fluid Mech. 1974, vol 57, pp. 785-796.

Chen J. H., Lienau J. J., Kollmann W. Numerical Simulation of Low Re-Number Turbulence in Round Jet. Proc.9th Symp. Turb.Shear Flows 1993.

Chorin A. J. and Bernard P. S. Discretization of A Vortex Sheet, With An Example of Roll-up, J. Comput. Phys. 1973,13, 423.

Chorin A. J. Numerical Study of Slightly Viscous Flow, J. Fluid Mech. 1973, vol. 57, pp.785-796.

Chorin A.J. and Marsden J.E. A Mathematical Introduction to Fluid Mechanics. Springer (New York) 1979.

Chung J. N. and Troutt T. R. Simulation of Particle Dispersion in an Axisymmetric jet, J. Fluid Mech. 1988, vol. 186, pp. 199-222.

Clarke NR. and Tutty O.R. Construction and Validation of a Discrete Vortex Method for the Two-Dimensional Incompressible Navier-Stokes Equations. Computers & Fluids 1994; Vol. 23, no. 6, pp. 751-783.

Cottet G. H. and Koumoutsakos P. Vortex Methods: Theory and Practice. Cambridge University Press 2000.

Crow S. C. and Champagne F. H. Orderly Structure in Jet Turbulence, J. Fluid Mech. 1971, vol. 48, pp. 547-591.

Danaila I, Dusek J., Anselmet F. Coherent Structures in a Round Spatially Evolving, Unforced Homogeneous Jet at Low Reynolds Numbers, Phys. Fluids 1997, 9, 3323-3342.

Davies P. O. and Hardin J. C. Potential Flow Modeling of Unsteady Flow, International Conference on Numerical Methods in Fluid Dynamics 1973, pp. 42-64.

Didden N. On The Formation of Vortex Rings: Rolling-up and Production of Circulation. Math. Phys. 1979, 30, 101.

Didden N. On Vortex Formation and Interaction with Solid Boundaries. In Vortex Motion (ed. E.-A. Muller) 1982, pp. 1-17.

Forstall W. and Shapiro A. Momentum and Mass Transfer in Coaxial Gas Jets. Trans. ASME, J Applied Mech. 1950, vol. 17, pp. 399-408.

Gazzah M. H., Belmabrouk H., Sassi M., A Numerical Study of The Scalar Field in Turbulent Round Jet With Co-Flowing Stream. Computational Mechanics 2004, vol. 34, pp. 430-437.

Ghoneim AF and Givi P. Vortex-Scalar Element Calculations of a Diffusion Flame Stabilized on a Plane Mixing Layer. NASA Tech. Memo 1987. 100133 ICOMP-87-4.

Giovannini A. Vortex Simulation of Axisymmetrical Flows in Cylindrical Geometries. Part I: Numerical Algorithm. J. of Thermal Science 1995, vol. 4, no. 4.

Grinstein F.F., Gutmark E., Parr T. Near-Field Dynamics of Subsonic Free Square Jets. A Computational and Experimental Study. Phys. Fluids 1995, vol. 7, no. 6, pp. 1483-1497.

Hussein H. J., Capp S. P., George W. K. Velocity Measurements in a High Reynolds Number, Momentum-Conserving Axisymmetric Turbulent Jet. J. of Fluid Mech. 1994, vol., 258, no. 31.

Inoue O. and Leonard, A. Vortex Simulation of Forced/Unforced Mixing Layers. AIAA J 1987. vol. 26, pp.1417.

Kiya M., Nagatomi M., Mochizuki O. Simulating an Impulsively Started Round Jet by a 3D Vortex Method. Proc. Int. Conf. Fluid Eng. 1997, vol. 1, pp. 135-140.

Knani M. A., Boisson H., Giovannini A., Lili T. Study of a Plane-Free Jet Exhausting from a Channel by Vortex-In-Cell Method. International Journal for Numerical Methods in Fluids 2006, vol. 52, pp. 529-543.

Lacombe G. and Mas-Gallic S. Presentation and analysis of a Diffusion-Velocity Method. ESAIM Proceedings 1999; vol. 7, pp. 225-233.

Lamb H. Hydrodynamics. Cambridge University Press 1932.

Langthjem M. A. and Nakano M., A Numerical Simulation of The Hole-Tone Feedback Cycle Based on An Axisymmetric Discrete Vortex Method and Curle's Equation. Journal of Sound and Vibration 2005, vol. 288, pp. 133-176.

Leonard A. Vortex methods for flow simulation. J. Comp. Phys.1980, vol. 37, pp.289-335.

Leonard A. T. Computing Three-dimensional Incompressible Flows with Vortex Elements. Annual Reviews of Fluid Mechanics 1985. 17, 523-559.

Lin P. and Pratt D. T. Numerical Simulation of a Plane Turbulent Mixing Layer, with Applications to Isothermal, Rapid Reactions 1987, AIAA Pap. 87-0224.

Liu C.H. and Doorly D.J. Velocity-Vorticity formulation with vortex particle-in-cell method for incompressible viscous flow simulation, Part 1: Formulation and validation, Numerical Heat Transfer, Part B, 1999, vol. 35, pp. 251-275.

Mansfield JR, Knio OM, Meneveau C. A Dynamic LES Scheme for the Vorticity Transport Equation: Formulation and a Priori Tests. Journal of Computational Physics 1998; 145: 693-730.

Marshall J. S. Inviscid Incompressible Flow. John Wiley & Sons (New York) 2001.

Milane RE and Nourazar, S. On the Turbulent Diffusion Velocity in Mixing Layer Simulated Using the Vortex Method and the Subgrid Scale Vorticity Model. Mechanics Research Communication 1995; 224; 327-333.

Milane RE and Nourazar S. Large-Eddy Simulation of Mixing Layer using Vortex Method: Effect of Subgrid-Scale Models on early Development. Mechanics Research Communication 1997; 242; 215-221.

Nitsche M. and Krasny R. A Numerical Study of Vortex Ring Formation at The Edge of a Circular Tube. J. Fluid Mech. 1994, vol. 276, pp.139-161.

Ogami Y. and Akamatsu. Viscous Flow Simulation Using the Discrete Vortex Model-The Diffusion Velocity Method. Computers & Fluids 1991, vol. 19, no. 3/4, pp. 433-441.

Ogami Y. A vortex Method for Heat-Vortex Interaction and Fast Summation Technique. First International Conference on Vortex Methods (Kobo) World Scientific 1999: 145:152.

Olsson M. and Fuchs L. Large Eddy Simulation of the Proximal Region of a Spatially Developing Circular Jet. Physics of Fluids 1996, vol. 8, no. 8, pp. 2125-2137.

Phillips O. M. Shear Flow Turbulence. Ann. Rev. Fluid Mech. 1969, vol.1, pp. 245-264

Pope S. B. Turbulent Flows. Cambridge University Press 2000.

Pullin D. I. The Largest-Scale Structure of Unsteady Self-Similar Rolled-up Vortex Sheets. J. Fluid Mech. 1978, 104, 45.

Pullin D. I. Vortex Ring Formation at Tube and Orifice Openings. Phys. Fluids 1979, 22, 401.

Rosenhead L. The Formation of Vortices from Surface of Discontinuity. Proc. Roy. Soc. 1931, Series A, vol.134, pp. 170-192.

Saffman P. G. The Velocity of Viscous Vortex Rings. Stud. Appl. Math. 1970, 49, 371380.

Saffman P. G. The Number of Waves On Unstable Vortex Rings. J. Fluid Mech. 1978, 84, 625.

Sarpkaya E. Vortex Element Methods for Flow Simulation. Advances in Applied Mathematics 1994, vol. 31, pp. 113-247.

Sidahmed M. M. and Brown R. B. Simulation of Spray Dispersal and Deposition from a Forestry Airblast Sprayer- Part I: Air Jet Model. Transactions of the American Society of Agricultural Engineers 2001, vol. 44, no. 1, pp. 5-10.

Sod G. A. A Hybrid Random Choice Method for Application to Internal Combustion Engine. Society of Automotive Engineers 1978, paper no. 790242, pp. 1-15.

Tennekes H. and Lumley J.L. A First Course in Turbulence. MIT Press 1972.

Uchiyama T. Numerical Prediction of The Round Jet in a Co-Flowing Stream by Three-Dimensional Vortex Method. International Journal of Turbo and Jet Engines 2003, vol. 20, pp. 235-244.

Uchiyama T. and Fukase A. Vortex Simulation of Gas-Particle Two-Phase Compound Round Jet. Powder Technology 2006, 165, pp. 83-91.

Verzicco R. and Orlandi P. Direct Simulations of The Transitional Regime of a Circular Jet. Phys. Fluids 1994, vol. 6, no. 2, pp.751-759.

Winckelmans G. S. and Leonard A. Contribution to Vortex Particle Methods For The Computation of Three-Dimensional Incompressible Unsteady Flows. J. Comput. Phys. 1993, 109, pp. 247-273.

Wygnanski I. and Fiedler H. Some Measurements in the Self-Preserving Jet. J. Fluid Mech. 1969, vol. 38, no. 3, pp 577-612.

Yanenko N. N. The Methods of Fractional Steps. Springer Verlag 1971.

Appendix

Present work uses one main program (**ea128_128.f**) adopted for the free jet flow and coflow jet as described below.

ea128_128.f: This program calculates the instantaneous velocity and vorticity field using the VIC, Diffusion Velocity Method and Deterministic Diffusion. Data files for flow fields are the streamwise mean centerline decay (P483024.dat); the streamwise mean velocity (P482508.dat); rms of velocity fluctuation and shear stress (P482511.dat); vorticity contours (P483023.dat) and the vortices distribution (P482510.dat); with variables $U_C, \frac{U}{U_C}, u', v', u'u', v'v', u'v'$ and will be written at the end of the program.

ea128_128.f :
The main program is a numerical computation of flow field and vorticity field.

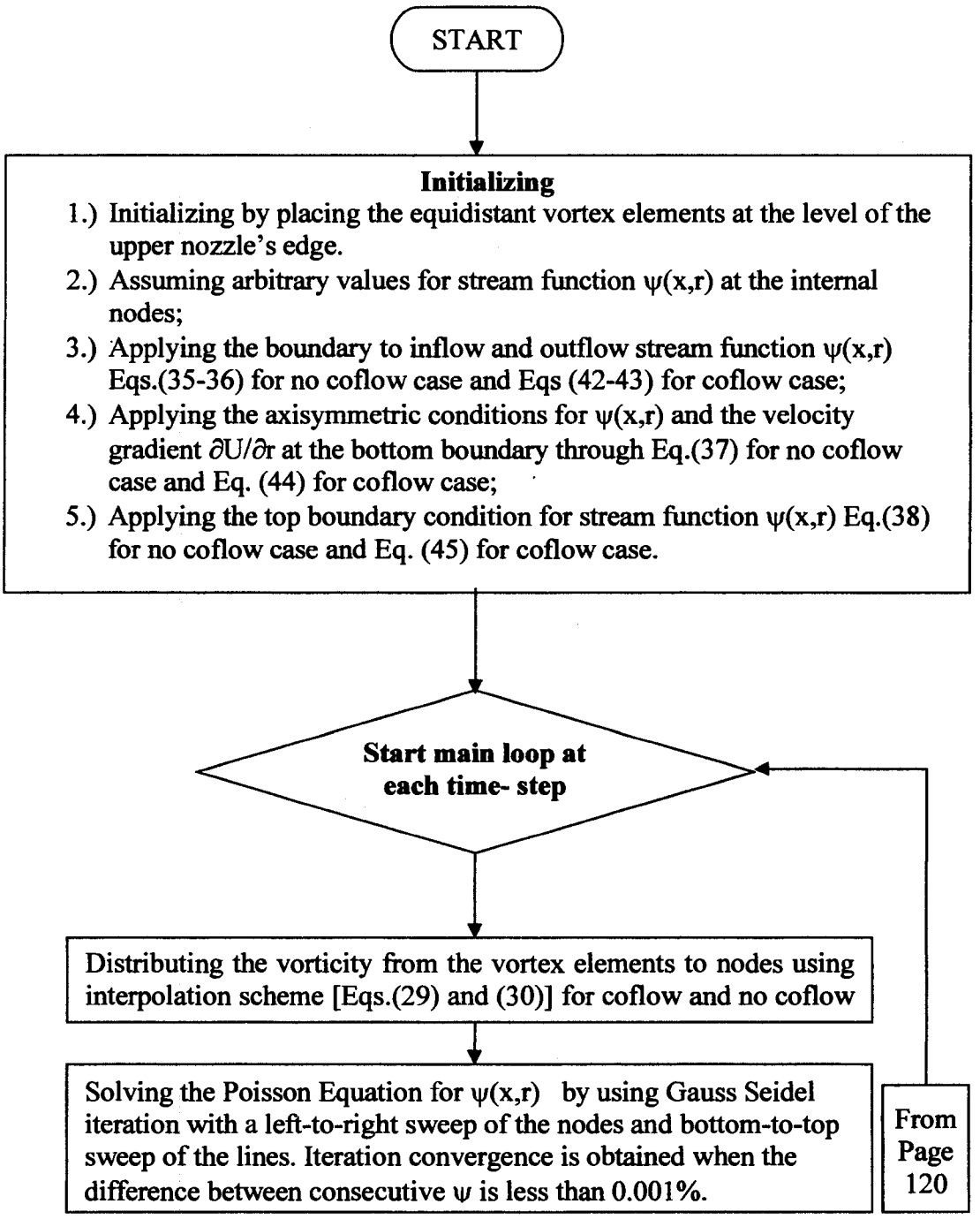

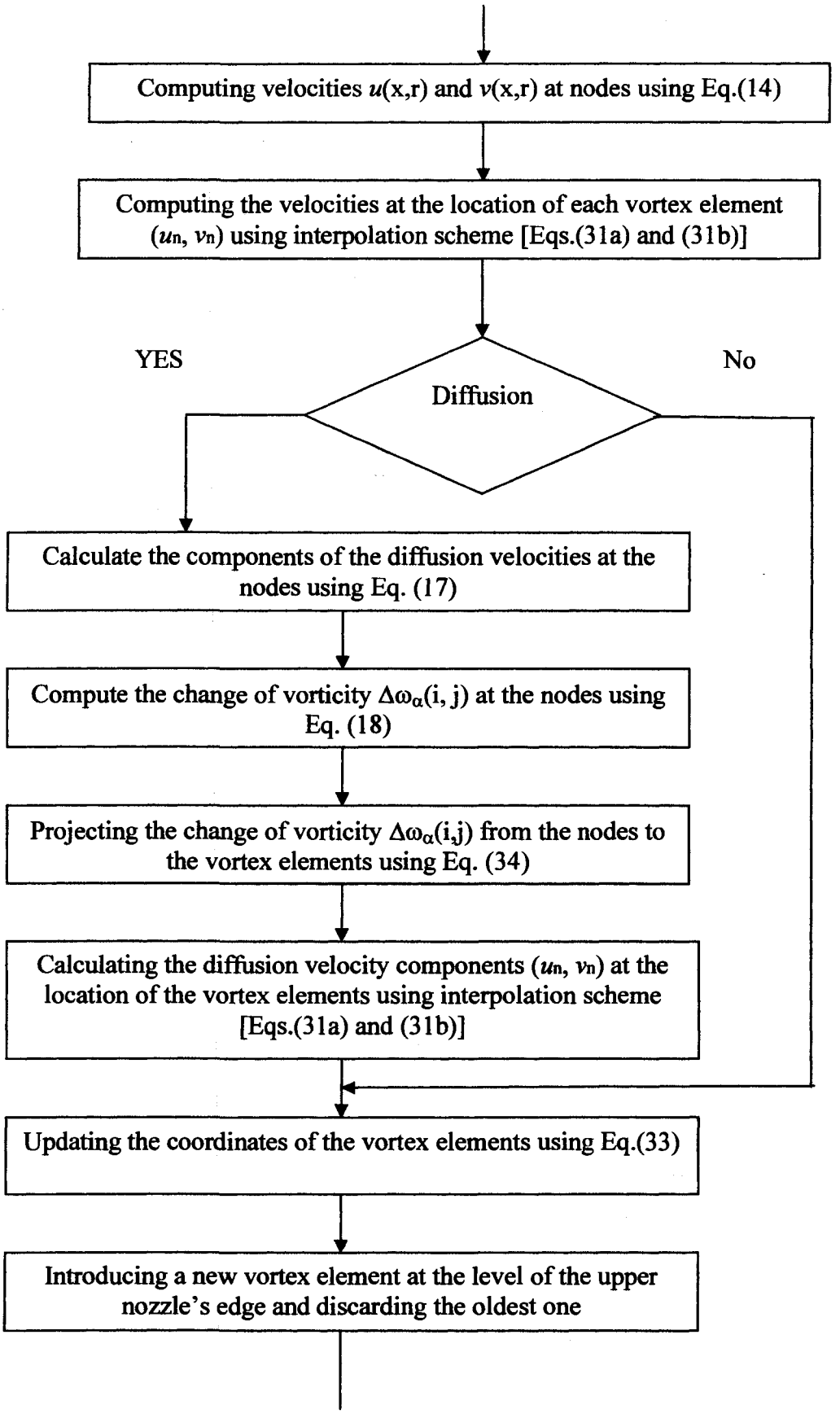
Computing velocities u(x,r) and v(x,r) at nodes using Eq.(14)
Computing the velocities at the location of each vortex element (u_n, v_n) using interpolation scheme [Eqs.(31a) and (31b)]
YES
No
Diffusion
Calculate the components of the diffusion velocities at the nodes using Eq. (17)
Compute the change of vorticity $\Delta\omega_\alpha(i, j)$ at the nodes using Eq. (18)
Projecting the change of vorticity $\Delta\omega_\alpha(i,j)$ from the nodes to the vortex elements using Eq. (34)
Calculating the diffusion velocity components (u_n, v_n) at the location of the vortex elements using interpolation scheme [Eqs.(31a) and (31b)]
Updating the coordinates of the vortex elements using Eq.(33)
Introducing a new vortex element at the level of the upper nozzle's edge and discarding the oldest one

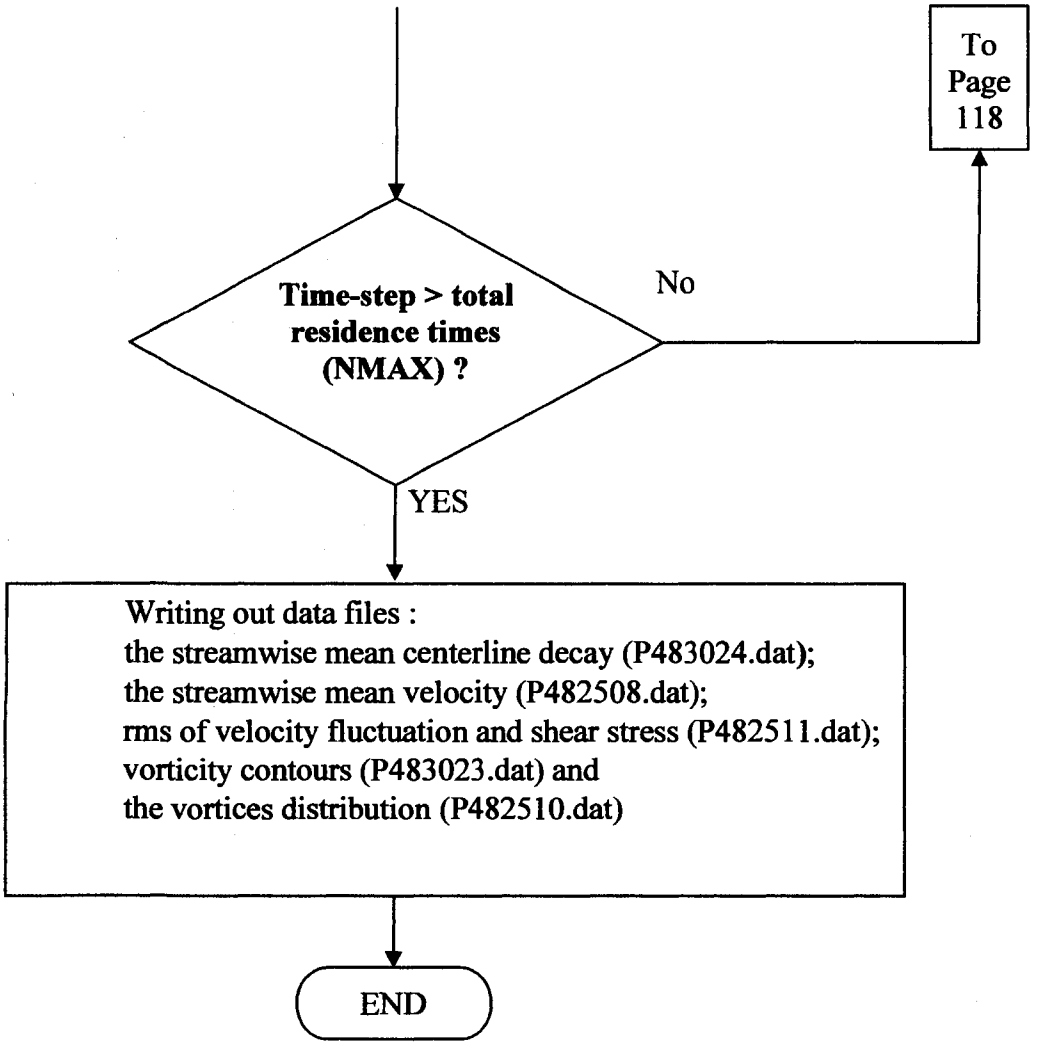
To Page 118
Time-step > total residence times (NMAX) ?
No
YES
Writing out data files :
the streamwise mean centerline decay (P483024.dat);
the streamwise mean velocity (P482508.dat);
rms of velocity fluctuation and shear stress (P482511.dat);
vorticity contours (P483023.dat) and
the vortices distribution (P482510.dat)
END